PhD project

Development of a framework to link functional activity and circuit wiring diagrams in the zebrafish larva brain

PhD Candidate: *Matteo Bruzzone*

Doctoral program in: *Neuroscience*
XXXV cycle

Padova Neuroscience Center - PNC

Coordinator: *Prof. Antonino Vallesi*

Supervisor: *Prof. Aram Megighian*

Co-Supervisor: *Prof. Marco Dal Maschio*

Ai miei genitori

Contents

List of Figures

Summary

In the last years, we have seen a significant increase in the developing of techniques to study the brain, both in terms of the functional circuit mechanisms and in the reconstruction of their anatomical organization. Whole brain dense anatomical reconstruction at synaptic resolution have provided insight into the brain architecture and how the information is transmitted. However, these datasets, even when the synaptic input/output relationship are known, are still far from revealing the general organization principles of the brain networks and how these interact one with the other. On the other side, light based techniques allow the functional characterization of the neuronal activity across the whole brain, in certain organism with cellular resolution, in association with sensory stimulation or during resting state conditions. While it is recognized that linking together these two aspects could foster a more in depth comprehension of the brain circuits, very limited are the tools and the approaches reported for this goal. With this planned aim, I focused on the circuit analysis of the zebrafish larva brain and present here the building blocks for developing an analysis framework combining these together. First, I will describe a tool for identifying functionally relevant networks based on their structural connectivity patterns which is adaptable to different anatomical datasets with or without identified synapses. Second, I will present an optical configuration for cell resolution which can be used to reconstruct the brain dynamics during sensory stimulation. Last, I will show an approach to link these two tools to functionally characterize anatomically identified neurons. The combination of these two tools can provide a deeper understanding on how the structure of the nervous system supports the flow of information and offer a more accurate basis for the formulation of models of the circuit working principles.

1 Introduction

In the late 18th century, the Italian physiologist Luigi Galvani described the functional properties of neurons when he observed that applying a small electrical current to a frog's leg caused it to contract. He proposed that this contraction was driven by an electrical current flowing through the nerves in the leg. This was the first functional description of neuronal activity. In the late 19th century, Spanish anatomist Santiago Ramón y Cajal used histological staining to examine the morphological properties of the neurons and describe their various components, including the cell body, dendrites, and axons. This work, along with that of Charles Sherrington, helped in establishing the cell theory of the nervous system, which states that the nervous system is made up of individual cells called neurons that act as the structural and functional basic elements. The connections between neurons, in the form of synapses or other type of junctions, are essential for communication within the brain and the emergence of functional roles. In the early 20th century, Lorente de Nó's work on connections in the brain laid the foundation for the understanding of how these could contribute to brain function. He highlighted "*the universality of the existence of plural parallel connections and of recurrent, reciprocal connections*" [1] which can create patterns of sustained neural activity between groups of neurons, actually representing the concept of a circuit [2]. Donald Hebb later expanded on this concept, developing the idea of "cell assemblies" postulating how recursive and reverberating patterns of neuronal activation between large populations of neurons is supported by correlated activity [3]. He defined a cell assembly as "*a diffuse structure comprising cells ... capable of acting briefly as a closed system, delivering facilitation to other systems, and usually having a specific motor facilitation*" [4].

In recent years, there has been a significant improvement of the techniques to study the brain, both in terms of its anatomical organization and function. By combining data of its function and circuit wiring with computational methods to analyze them, it is possible to gain a deeper and more comprehensive understanding

of the brain working mechanisms. In the thesis work, we aim at integrating the functional and the structural aspects of the brain in a common reference space where to analyze the functioning mechanisms of the circuits based on the wiring properties and the activity patterns. We will start with an introduction about the current state-of-the-art for both structural and functional analyses in model organisms and the rationale that prompted us to embark on this work (Chapter 1). In the next session, we will describe the methods developed and applied as the building blocks of a comprehensive analysis framework (Chapter 2). Following the methodological part, we will present the outcome and the results obtained (Chapter 3, Chapter 4 and Chapter 5). In the last section, we will present the basis for the strategy and the mathematical approach to integrate together these circuit analysis approaches under the same framework (Chapter 6).

1.1 Inferring the circuit connectivity in the brain

In general, brain connectivity in the brain refers to the patterns of connections between different brain regions or individual neurons that allow information to be transmitted, enabling the processing of sensory inputs and the selection of the proper motor program. Connections can be studied by identifying the input and output points either by directly reconstructing the synaptic information, or by inferring these based on proximity (Structural connectivity). In alternative, connectivity can be estimated based on the temporal correlation that characterize the activity profiles of the different regions or neurons (Functional connectivity).

1.1.1 Structural connectivity

Neuronal morphologies and connections have been described with neural tracing performed either with neurotropic viruses, such as herpes and rabies virus, encoding a fluorescent reporter [5–11] or with fluorescent dyes [12–17].
Neural tracing can be performed by injecting the tracers in the population of interest. A tracer can be injected in the soma of neurons and transported to the axon to investigate where a neuron

project; in this case, it is defined anterograde. A tracer can be injected in the axon and transported to the soma to investigate where a projecting neuron is located; in this case, it is defined retrograde [18]. Moreover, trans-synaptic tracers or GFP-fragment split between pre- and post-synaptic neurons can be used to identify post-synaptic partners of specific neurons [19, 20]. The injection of distinct viruses targeted to a specific population of input and output neurons can inform on the neuronal synapses [21] and the combination with optogenetics can further characterize the connections [22]. A brain-wide, cellular-level, mesoscopic[1] connectome for the mouse has been published [23] and recently, a virus-based approach has been developed to label, at a whole-brain level, presynaptic neurons of a target neuronal class [24].
Along with virus-mediated approaches, one can take advantage of transgenic methods for sparse labelling of individual neurons or markers in neurons that are sub-sequentially acquired [25–27]. However, these methods are difficult to integrate on a whole-brain scale and their level of detail results in the loss of conceptually important information on the collateral branching patterns of neurons [28].

1: The mesoscale connectome represents connections between neuronal types across different brain regions, lacking finer detail of neurons morphology and synapses [6]

SBEM, serial block-face scanning electron microscopy is an imaging technique performed on thin sheets of biological samples acquired sequentially and merged afterward to reconstruct the 3D volume that provides superior dense anatomical reconstruction (Figure 1.1A) [29]. EM-based imaging was used to create the first synapse-level neural map of the nematode *Caenorhabditis elegans*, a small, transparent roundworm that has a simple but well-defined and stereotyped nervous system composed by 302 neurons. Initially, the pharyngeal nervous system was reconstructed [30] and later the whole organism [31].
With its continuous development and refinement [32–36], EM-based imaging has been applied to reconstruct the volume of the central nervous system of the larval form of the *Ciona intestinalis* [37], eyes in a larva of the marine annelid *Platynereis dumerilii* [38], visual system, mushroom body and other neural circuits in adult and larval *Drosophila melanogaster* [39–44], olfactory bulb of zebrafish larvae [45], basal ganglia of the songbird [46] and several portions of the mouse cortex and visual system [47–50]. At the whole brain level, in addition to *C. elegans* [31], the volume of the nervous system of the predatory nematode *Pristionchus*

pacificus [51], the brain of the larval [39, 42] and adult *Drosophila melanogaster* [52] and the brain of the zebrafish larvae [29] have been reconstructed (Figure 1.1C).
Dense anatomical reconstruction provides a 3D representation of the imaged volume at typical resolution of few nanometers (Figure 1.1A). Typically, extracting the information from this dataset requires: the identification of a series of seed points from which starting the reconstruction of the cellular skeletons; from the skeletons, either with manual or automated pipelines, the cells must be segmented; and ultimately, annotated to identify the pre- and post-synaptic partner (Figure 1.1B). Subsequently, the results must undergo human proofreading. These steps are resource-demanding and result in several years of work (up to 100 human-years for the fly hemibrain connectome [53]); the continuous development of high-performance machine learning tools to reliably segment neurons hold promise for more accessible annotated EM-connectomes [46, 54–56]. Currently, the complete dataset of annotated neurons and synapses has been produced for the 302 cells of the *C. elegans* [57], for 3013 neurons from the brain of the larval Drosophila [58] and for the 25 thousands of the adult Drosophila hemibrain [53] (Figure 1.1C). From the annotation of the synaptic partners, it is possible to extract the adjacency matrix that is the mathematical representation of the input-output relationships established between all the cells in the reconstructed volumes.

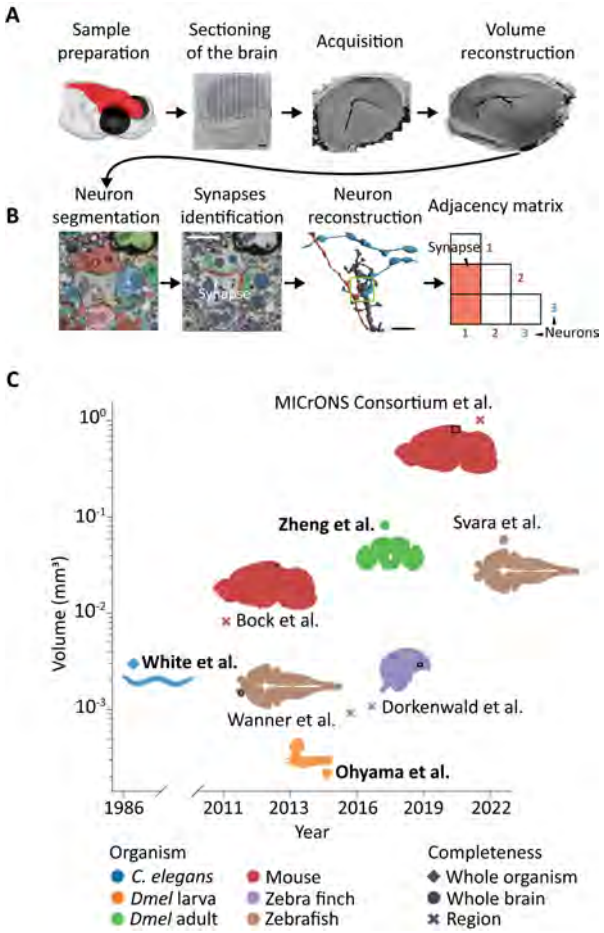

Figure 1.1: EM-reconstruction pipeline and main EM-reconstructed volumes.
A) Workflow to generate a EM-reconstructed volume and **B)** the related connectome. Scale bars: 50 μm (Sectioning of the brain), 1 μm (Synapses identification, Neuron reconstruction). **C)** Selected datasets by year of publication. In **bold** are reported datasets on which a connectome has been mapped.
Refs: **White et al.** [31, 57], Bock et al. [47], **Ohyama et al.** [39, 58], Wanner et al. [45], Dorkenwald et al. [46], **Zheng et al.** [52, 53], MICrONS Consortium et al. [50], Svara et al. [29].
(A - B) Adapted from [29, 56].
(C) Adapted from [59].

1.1.2 Functional connectivity

Temporal correlation is a common measure to assess functional connectivity between neurons [60]. It is based on the assumption that non-independent neurons should carry non-independent signals, thus sharing some level of common variability [61]. Although functional connectivity is widely used [62–66], it hardly reflects effective connectivity. This is due to the presence of indirect connections between correlated neurons, typical scenarios with multiple neurotransmitters involved, redundant population encoding by independent neurons, and articulated scheme of convergence involving independent inputs [62, 67–69]. Furthermore, correlation alone, except in some particular circumstances, does not provide causal relation between the neuronal component involved in the observed activity.

To infer causality between the activity of distinct neurons, one would like to record the changes in the system activity when boundary conditions or network properties are known or artifi-

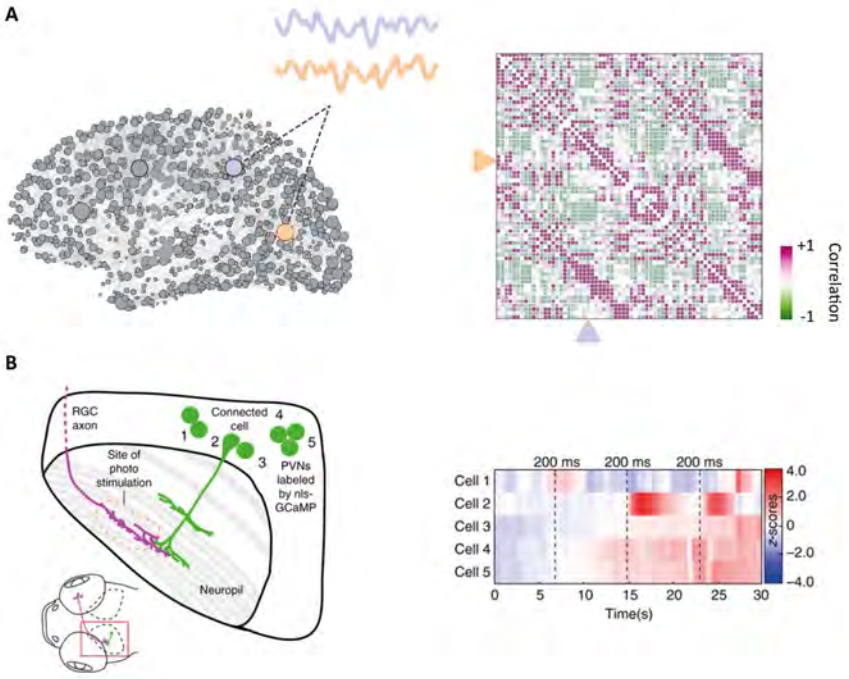

Figure 1.2: Functional connectivity. **(A)** Functional connectivity between nodes in the human brain. Connection is estimated based on correlation between node time courses. (B) Optogenetic stimulation to identify connectivity in the zebrafish larva. Connection is estimated based on post-synaptic partner activity after photo-stimulation (dashed line on right image) of the pre-synaptic one. The periventricular neuron (PVN) connected to the retinal ganglion cell (RGC) axon is Cell 2.
Adapted from [84, 85].

cially controlled. Recent development and constant improvement of light-activated modulators of membrane potential offer in this sense a tool to probe circuit mechanisms, i.e., to measure the output of the circuit while controlling the status of genetically or spatially identified subpopulations [70–72]. This functional interrogation has allowed the characterization of circuit wiring in a non-invasively and non-destructively fashion [73, 74]. For example, it has been used to investigate connectivity in the genetically defined neuron population [75], cortical microcircuit [76], long distance pathways [77], synaptic communication [78, 79] and has been combined with other techniques such as fMRI and optical intrinsic signal imaging [80, 81].

Both structural and functional connectivity are important for understanding how the brain works [66, 82, 83]. Structural connectivity provides insight into the brain's architecture and how information is transmitted. Functional connectivity, on the other hand, can reveal how patterns of neuronal activity support brain functions. Together, structural and functional connectivity can provide a comprehensive view of the brain.

1.2 Functional recordings of the brain activity

Investigating how patterns of neuronal activity support the processing of sensory information and the selection of an appropriate motor program is a fundamental task. In this sense, appropriate model organisms showing a panel of sensory driven behaviours in combination with powerful methods for recording the neuronal activity with cellular resolution across the complete brain do offer an unique opportunity.

1.2.1 Model organisms

Currently, only few model organisms allow the study of the brain dynamics at the whole brain scale with cellular resolution during a sensorimotor integration task [86–88].

Among the vertebrates, larval zebrafish is one of the few and results the most commonly used. This is due to its optical transparency in the first few weeks of life, as well as its brain's suitable dimensions in terms of accessible volume (about $400 \times 800 \times 250$ μm^3 (W × L × H)) and number of neuronal units (estimated to be between 80,000 and 120,000). Additionally, at early developmental stages, zebrafish larvae are already able to perform a wide range of spontaneous and sensory-evoked behavioral maneuvers, making them an ideal model system for studying brain circuit mechanisms. The observation of neuronal activity in large populations across the zebrafish brain has been made possible through the use of engineered proteins for measuring physiological activity and novel optical technologies and imaging methods to record it.

1.2.2 Molecular tools to record neuronal activity

Intracellular calcium (Ca^{2+}) is a key second messenger in cells. In neurons, action potentials trigger rapid increases in intracellular free Ca^{2+} levels through the activation of voltage-gated ion channels and NMDA receptors [89–91]. Genetically encoded fluorescent calcium indicators (GECIs) are tools that allow for the optical detection of changes in Ca^{2+} levels in cells. These indicators

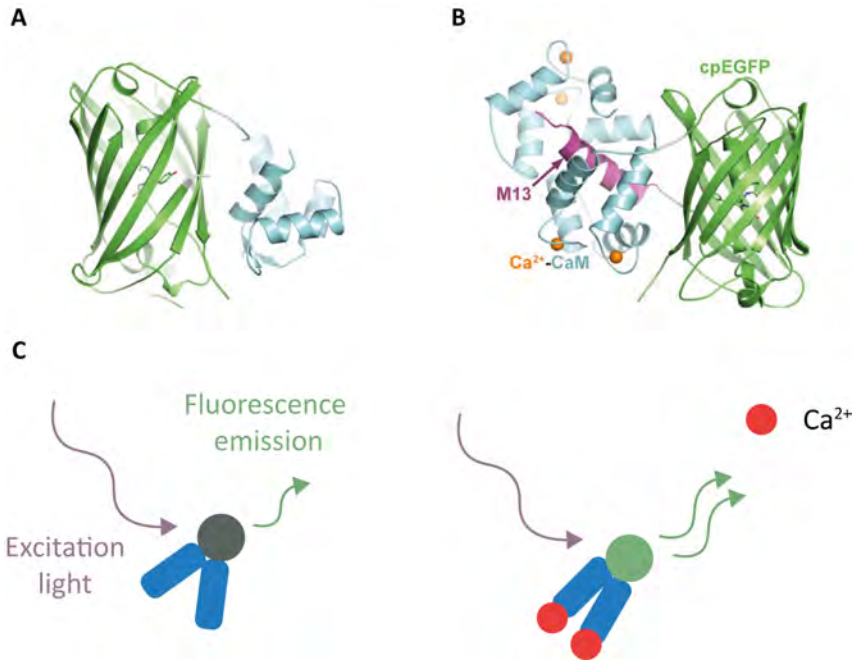

Figure 1.3: GCaMP.
A) Model structure of Ca^{2+}-free GCaMP. Adapted from [101]. **B)** Model structure of Ca^{2+}-saturated GCaMP. Adapted from [101]. **C)** Genetically encoded fluorescent reporters of calcium are designed to display variations in the fluorescence yield (green) as a consequence of the binding of calcium (red). Adapted from [97].

are genetically engineered to change the fluorescence emission in response to Ca^{2+} concentrations, enabling optical recording of large groups of cells. GECIs can be targeted to specific cell types or subcellular compartments, allowing for calcium imaging in specific areas or subcellular domains [92, 93]. For example, cytosolic GECI can be used to measure calcium fluctuations in small neuronal structures, such as dendrites and spines, when labelling is sparse. However, in conditions of dense labelling, it can be difficult to accurately measure calcium activity in individual neurons due to the presence of neuropil and the surrounding neuronal processes. To overcome these limitations, GECIs have been effectively targeted to the cell body or nucleus in zebrafish and fly [94–97]. GCaMP is currently the most widely used GECI in neuroscience. The molecular structure comprises a green fluorescent protein (EGFP) bound, through a M13 fragment of a Myosin Light Chain, to Calmodulin (CaM) [98] (Figure 1.3A,B). CaM is a calcium binding protein which, with the increase in intracellular calcium concentration following the firing of an action potential, induces a conformational change to the overall configuration resulting in an increase in the detected fluorescence intensity (Figure 1.3C). In 2013, a family of ultrasensitive calcium reporters, GCaMP6, was introduced [99] and later improved with the GCamp7 family [100].

1.2.3 Microscopy methods to record neuronal activity on the whole brain

Light-based techniques have been successfully applied in investigating information processing in an intact brain circuit [102]. With respect to electrophysiological measures, these methods allow recording from a large number of cells comprising the volume of the brain. Currently, there are limited options available for volumetric imaging. An approach to recording brain activity throughout a 3D volume involves the use of optical elements to scan the imaging beam in the longitudinal direction (Z) of the sample. This is typically achieved by moving the imaging objective with a piezoelectric actuator [103]. However, this design generates vibrations, thus perturbing the system. Recently, alternative methods have been developed. These involve manipulation of the light wavefront curvature at the back focal plane (BFP) of the objective, allowing remote control of the effective focal position without moving the objective [104].

Generally, when scanning a beam within a sample volume, the modulation of the light wavefront at the BFP of a lens or objective is crucial. By superimposing a spatial gradient or a curvature on the phase of the electric field of a flat light wavefront, the focus of the beam can be laterally or longitudinally shifted at the Frontal Focal Plane (FFP) as the wavefront propagates (Figure 1.4 A -B). To facilitate this wavefront modulation, the BFP of the objective is optically conjugated to a remote plane using relay optics, where a modulating element can be conveniently placed (Figure 1.4 B). When multiple modulations are needed, for example for introducing both vertical and horizontal tilts and curvatures, they can be placed closely together near the focal plane of the scan lens or distributed in multiple locations and conjugated to the BFP of the objective.

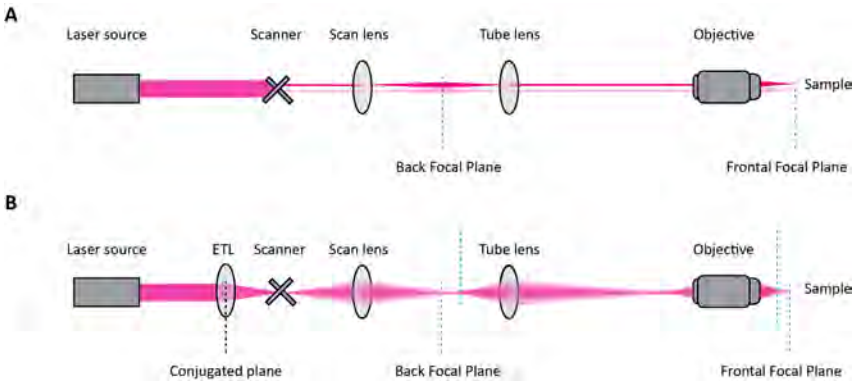

Figure 1.4: Lateral and longitudinal focus shift.
A) Laterally shifted focus of the beam by means of galvanometric mirrors. **B)** Longitudinally shifted focus of the beam by means of an Electrically Tunable Lens (ETL) placed in a plane optically conjugated with the Back Focal Plane.

Scanning the sample along the lateral dimension The most common method to scan a sample along the lateral dimension involves using a pair of galvanometric mirrors that are conjugated to the back focal plane (BFP) of the objective. These mirrors are two movable plates with orthogonal optical axes, each measuring between 3-6 mm wide, and their orientations can be adjusted by appropriate control signals. By changing the angle of the mirrors relative to the direction of propagation of the incoming beam, a linear phase gradient is introduced into the wavefront, resulting in a lateral shift of the beam relative to the field of view (FOV).

In a raster scanning scheme, one mirror sweeps over a line while the other jumps to the next line. With a typical pixel dwell time of approximately 4 µs, this design allows for frame acquisition times of less than a second for a pixel matrix of 512 x 512 pixels. An 8 or 12 kHz resonant galvanometric mirror can replace the line scanning galvo, reducing the line acquisition time to 62 or 41 µs, respectively, and increasing the acquisition rates to up to 30-45 frames per second for a pixel matrix of 512 x 512 elements. However, in this second scenario, there is no direct control over the pixel dwell time, and its short duration, typically 120-80 ns, significantly affects the number of collected photons per pixel and ultimately impacts the image signal-to-noise ratio (SNR).

Scanning the sample along the longitudinal dimension Remote adjustment of the longitudinal position of an excitation spot generally relies on the possibility of imposing a curvature on the wavefront profile in an upstream plane optically conjugated to the BFP of the objective. An approach is to use a spatial light modulator (SLM), a matrix of liquid crystal molecules that uses a control voltage to modulate the phase delay of different spatial

components of a wavefront [105–109]. Another method for faster longitudinal scanning is to use an acousto-optic lens, which adds a variable curvature to the wavefront using a combination of acousto-optic deflectors (AODs) that produce a gradient of spatial frequency to locally deflect the wavefront [110, 111]. A lens with a controllable focal length can also be used, either downstream of the XY scanner and the scan lens-tube lens pair or in an upstream plane optically conjugated to the BFP. An example of such a device is an electrically tunable lens (ETL) which consists of a liquid volume enclosed between a glass and an elastic polymer membrane [112]. By using an electromagnetic coil powered by an electric current, pressure is applied to the liquid, causing the membrane to curve and increasing the lens's focal power. ETL can achieve a focal range of a few hundred micrometers with minimal distortion of the point spread function (PSF) in response to a step-like control signal (5-7 ms settling time). To acquire a volume image, the ETL can be synchronized with frame acquisition also by using a sawtooth control signals, enabling plane-by-plane acquisition. In this case, the axial scanning continuous with a submillisecond refresh rate. As a result, volume information is gathered section by section along the longitudinal axis, rather than moving plane-by-plane.

1.3 Principles of network organization

So far, the recording of functional activity has been interpreted most frequently with rate models [113] which generally assume a certain connectivity scheme and specific neuronal properties or neurotrasmitter specificity [114, 115]. In parallel, researchers have considered applying graph theory analysis on connectome dataset to characterize the general architectural elements of the networks and extract a number of parameters that describe the organization of the brain network.

1.3.1 Graph theory analysis of the circuit connectomes

Graph and network analysis provide a convenient abstraction to investigate the organization of the network. In this framework, connectomes are composed of nodes (the unit, a functional or

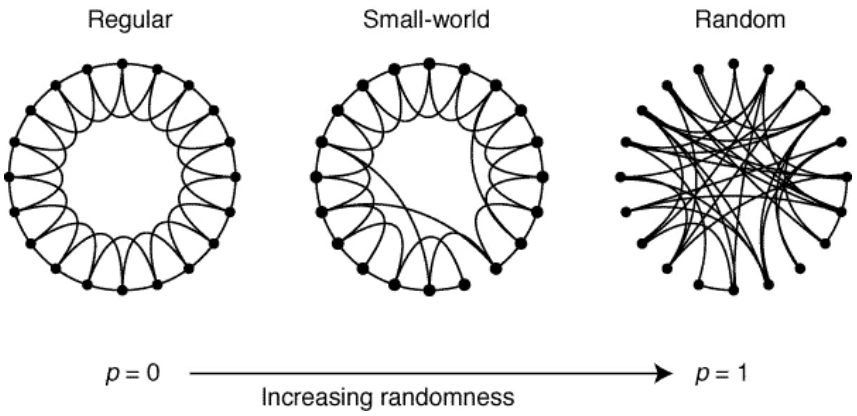

Figure 1.5: Small-world network. Wiring patterns in function of randomness. Adapted from [119].

anatomical neuron) and edges (connections between nodes, correlation or synapses) [82, 116]. In addition, each node displays a degree indicating the number of edges, and each edge displays a weight indicating the strength of the connection. The generated graph or network can be defined as directed or undirected on the basis of the nature of its edges, whether a precise directionality can be assigned to the information flow.

It is postulated that an optimal network configuration for cost-effective information transfer should depend on a calibrated balance between local and global features that maximize information processing and integration while minimizing wiring cost [117]. This configuration lies between a totally regular connection pattern and a completely random one, and it is called a "small world" (Figure 1.5) [118, 119]. In a small world network, nodes are usually organized in clusters, and although most of them are not neighbors, the number of edges dividing them is generally small. Several small-world properties have been found to correlate to some extent with the *C. elengas* EM-connectome [119, 120], fly EM-connectome [121], zebrafish larvae posterior later line GFP-connectome [122], zebrafish larvae whole brain spontaneous activity correlation-connectome [123], zebrafish larvae brain region GFP-connectome [27], pigeon forebrain marker-connectome [124], mouse neural tracing-connectome [23], human structural MRI- and functional fMRI-connectome [125, 126].

1.3.2 Biological value of network organization

The application of graph analysis provides a powerful abstraction to which to apply computational methods to discover system-level patterns. However, the extracted network properties are not sufficient to characterize circuit function because they do not provide a biological insight, and, usually, they describe global features lacking temporal features of functional connectivity or local properties in anatomical connectivity. A more comprehensive view will come with the integration of these properties with multimodal datasets combining anatomical reconstruction and functional recording [127]. The structural network of the Drosophila hemibrain has a high clustering coefficient that is consistent with whole-brain recording of spontaneous activity [121]. However, there are also some differences between the two types of connectivities. For example, the anterior ventrolateral protocerebrum has a relatively high clustering coefficient in the functional graph compared to its structural one, while the mushroom body (MB), the lateral horn (LH), and the antennal lobe (AL) have relatively high degrees and clustering coefficients compared to their respective structural graphs. The higher clustering coefficient in the functional graph of the MB can be understood in the light of the functional value of this region. MB is a high-order associative center involved in odor processing that can be subdivided into 15 compartments with segregated output neurons and different types of dopaminergic (Figure 1.6A-C) neurons [128, 129]. Neurons within each compartment receive inhibitory input from neurons located in their own compartment and disinhibitory feedback from a compartment of opposite valence, suggesting that the MB acts as an interconnected ensemble during learning (Figure 1.6D) [130].

The strength of regional structural connections in the zebrafish brain exhibit a log-normal distribution and decay with distance [27], this is in line with whole-brain spontaneous activity of neurons aggregates [123]. Log-normal distribution of connection strengths is a property of small-world network and it is found in many biological networks [131, 132]. Moreover, regional structural connectivity correlates with functional connectivity of neurons aggregates (Figure 1.7) [133]. Additionally, certain clusters of neurons in the hindbrain that are strongly connected have been found to be specialized for specific behavioral functions [134].

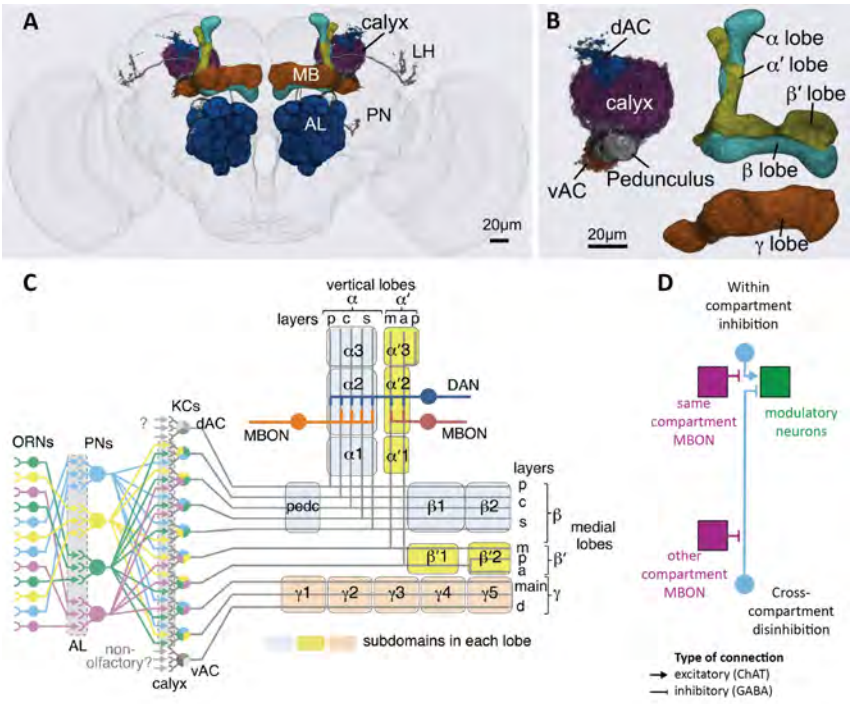

Figure 1.6: Mushroom body connectivity.
A) Adult female brain showing the antennal lobes (AL) and subregions of the mushroom bodies (MB). LH: lateral horn. Adapted from [128]. **B)** Subregions within the MB. The γ lobe, calyx, and pedunculus (pedc) are displayed separately from other lobes. vAC: ventral accessory calix, dAc: dorsal accessory calix. Adapted from [128]. **C)** Information flow to the MB during processing of olfactory inputs. ORN: olfactory receptor neuron, PN: antennal lobe projection neurons, KC: kenyon cell, MBON: mushroom body output neuron, DAN: dopaminergic neuron. Adapted from [128]. **D)** Schematic wiring diagram showing indirect inhibitory within-compartment feedback and disinhibitory feedback from a compartment of opposite valence converging onto the same DAN. Adapted from [130]

Another example comes from the integration of structural connectivity and graph analysis with ecological observation. In *P. pacificus*, the flow of information is higher in the front part of the pharynx compared to the same region in *C. elegans*. In *C. elegans*, the flow of information is higher in the isthmus compared to *P. pacificus*. This suggests that the different complexities of the information flow in the two species may be related to differences in the complexity of the connections due to distinct foraging behaviours [51].

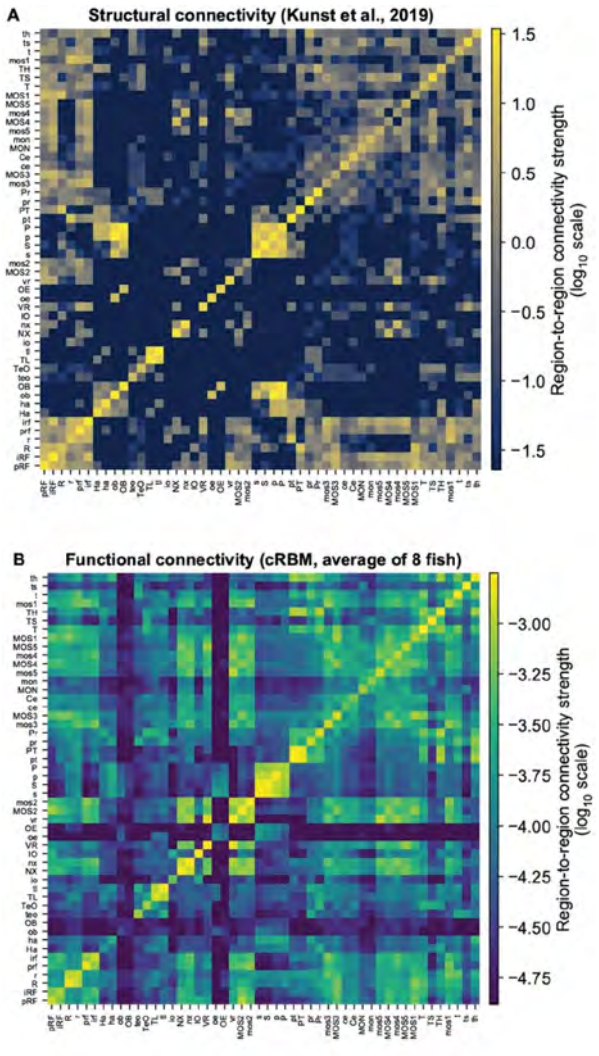

Figure 1.7: Comparison structural and functional connectivity in zebrafish larva. A) Regional structural connectivity matrix adapted from [27]. (B) Inferred average regional functional connectivity matrix. Regions are labeled according to [27]. Adapted from [133].

1.4 Aim of the thesis

To gain a more comprehensive understanding of the brain, it is important to examine both its activity and wiring structure. While advances in technology have made it possible to reconstruct the synapses of almost all neurons, the relationship between structural connectivity and function is not yet fully understood. Additionally, techniques for recording activity from the entire brain are limited and challenging to implement. This PhD thesis aims to address these issues by developing a framework for studying neuronal mechanisms in zebrafish larvae that includes a tool for identifying brain networks based on their structural connectivity patterns and a method for reconstructing neuronal activity from the entire brain at a cellular level using a multi-photon microscope and link this to the anatomical information.

Methods 2

The first section deals with the graph theory methods used for the analysis of the brain connectome. These include the evaluation of basic topological parameters of the graph and the description of the algorithm used to discover the communities, the Leiden algorithm. I describe then the application of the Leiden algorithm on a fully annotated dataset obtained from EM reconstruction of the Drosophila adult brain, where the information about the input-output relationship of the synapses is available. Following this proof of principle validation, I introduce the strategy devised to generate a proxy of the zebrafish larva brain connectome starting from an available dataset of single cell neuronal reconstructions, where the synaptic information is not available, and extend the community detection algorithm to this type of dataset.
The second section describes the methods for integrating an electrical tunable lens on a multi-photon microscope and performing volumetric imaging on a zebrafish larvae. The section is adapted from candidate first-author research paper [135].
The third section covers the methods for extracting activity from recorded neurons and identifying stimulus-responsive cells.
Finally, the fourth section outlines the methods for mapping the functionally recorded neurons onto the zebrafish brain atlas.

2.1 Reconstructing the connectome and the circuit wiring diagram

2.1.1 Basic concepts of graph analysis

A graph can be conveniently summarized mathematically in a corresponding adjacency matrix, where each entry along the line i and the column j represents the number of connections between an output node i and an input node j. The adjacency matrix naturally support the representation of a network structure, like a neuronal

circuit where neurons are represented as nodes and the synaptic connections between them are represented as edges.

In analyzing a network, there are two fundamental properties that represent the organization, the node degree and the weight of the edges. The degree of a node, which is the number of edges associated with the same node. The weight of an edge, in turn represents the strength of the connection between two nodes and is defined as the number of mutual connections between the two nodes (Figure 2.1). Additionally, the degree of a node can be weighted, taking into account the weight of its edges. A network can be defined as undirected in which each edge does not displays a direction (Figure 2.1A) or directed in which each edge display a direction (Figure 2.1B); the corresponding adjacency matrix is asymmetric or symmetric, respectively.

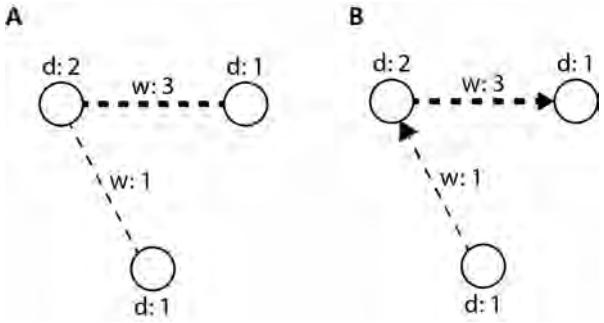

Figure 2.1: Key properties of the network.
A) Example of three nodes (circle) connected by edges (dashed lines) in an undirected way. d refers to the degree of the node (i.e. the number of edges) and w refers to the weight of the edge. For example purpose, weights are represented as thickness. **B)** Example of three nodes (circle) connected by edges (dashed lines) in a directed way.

In the first analysis of the connectome, we adopted a series of parameters to characterize the topological features:

- The number of **connected components** refers to the number of isolated sub-network of connected nodes. If there is a large group comprising most of the nodes, it is defined as giant component.

- The **average shortest path length** is defined as the average number of steps between nodes and it is a measure of efficient information transmission. It is described as:

$$a = \sum_{s \neq t} \frac{d(s,t)}{n(n-1)} \tag{2.1}$$

where $d(s,t)$ is the distance between node s and node t and n is the number of nodes in the graph.

- The **density** of a network is the ratio of actual edges to potential edges. It is described as:

$$d = \frac{2m}{n(n-1)} \tag{2.2}$$

where m and n represent, respectively, number of edges and nodes of the graph.

- The **weighted clustering coefficient** measures how connected a node's neighbors are to one another. It is described as:

$$c_i = \frac{1}{k_i(k_i-1)} \sum_{jk} \left(\tilde{w}_{ij}\tilde{w}_{jk}\tilde{w}_{ki}\right)^{\frac{1}{3}}$$

where k_i is the degree of node i and the weights of the neighbours are scaled by the largest weight of the network, $\tilde{w}_{ij} = w_{ij}/max(w_{ij})$ [136]. The average of the clustering coefficients is described as:

$$C = \frac{1}{n} \sum_{i \in G} c_i \tag{2.3}$$

where G is the graph.

- The **assortativity** describes the preference of the nodes to connect with other nodes with similar number of degrees. It is described by the correlation coefficient:

$$\beta = \frac{\sum_{xy} xy(m_{xy} - a_x b_y)}{\sigma_a \sigma_b} \tag{2.4}$$

where m is the fraction of all edges in the network, x and y are the degrees of two nodes, a_x and b_y are the fraction of edges at nodes with degree x and y and σ_a and σ_b are the standard deviation of the distribution a_x and b_y [137].

The analysis of these parameters was performed using dedicated Python libraries.

https://networkx.org/

The following functions from the '**networkx**' library have been used: *'connected_components'* to identify the network connected components, *'average_shortest_path_length'* to compute the average shortest path length as described in Equation 2.1, *'density'* to compute the density of the network as described in Equation 2.2, *'average_clustering'* to compute the average clustering coefficient of

the network as described in Equation 2.3, *'degree_assortativity_coefficient'* to compute assortativity correlation coefficient as described in Equation 2.4.

2.1.2 Community detection

Understanding the network structure in terms of its organization in sub-components or sub-networks offers the possibility to grab aspects of the network information processing that are not evident directly from the topological parameters described above. To extend the analysis in this sense it is possible to apply algorithms to highlight the presence of communities leveraging the connectivity properties of the nodes. In this class are comprised a number of approaches, mostly dealing with the optimization of a functional called modularity. This is defined as:

$$Q = \frac{1}{2m} \sum_c \left[m_c - \left(\frac{K_c}{2m} \right)^2 \right] \tag{2.5}$$

where m is the total number of edges, m_c is the total edges weight in community c, K_c is the total weighted degree of nodes in community c and $\left(\frac{K_c}{2m}\right)^2$ represents the expected number of edges in the community obtained the configuration model. The configuration model is a method used to generate a random network given a pre-defined degree sequence, serving as reference network model [138]. Maximizing the difference between actual and expected edges leads to the identification of groups of densely connected nodes, i.e. communities.

To identify communities based on modularity optimization, we applied the Leiden algorithm, a community-detection algorithm that ensure the identification of well-connected communities [139]. The method proceeds through three main phases:

1. A *fast local moving phase* in which individual nodes, initially assigned to their own community (Figure 2.2A), are relocated to the community c_i that results in the largest improvement of Q (Figure 2.2B).
2. A *refinement phase* in which increase of Q is performed intra-communities and typically leads to the identification of communities (c_j) within the communities identified in the

fast local moving phase (c_i). The network is initially set to a partition in which each node is assigned to its community c_n; then, the nodes are locally merged in the same community c_j only if they belong to the same community c_i (Figure 2.2C). This results in c_j being contained in c_i. The community c_j is chosen randomly, but with a higher probability of selection if it leads to a greater increase in the quality function. Usually this phase yields to the identification of more communities c_j than communities c_i.
An example of this can be seen in Figure 2.2C, where the red shaded region represents the red community identified in Figure 2.2B. Within this area, the red and green communities become distinct after the refinement stage. A similar pattern is observed in the green shaded region.

3. An *aggregation phase* in which nodes are aggregated based on the belonging c_j and labelled accordingly to the belonging c_i (Figure 2.2D). The aggregates nodes undergo the *fast local moving phase* (Figure 2.2E) and *refinement phase* (Figure 2.2F).

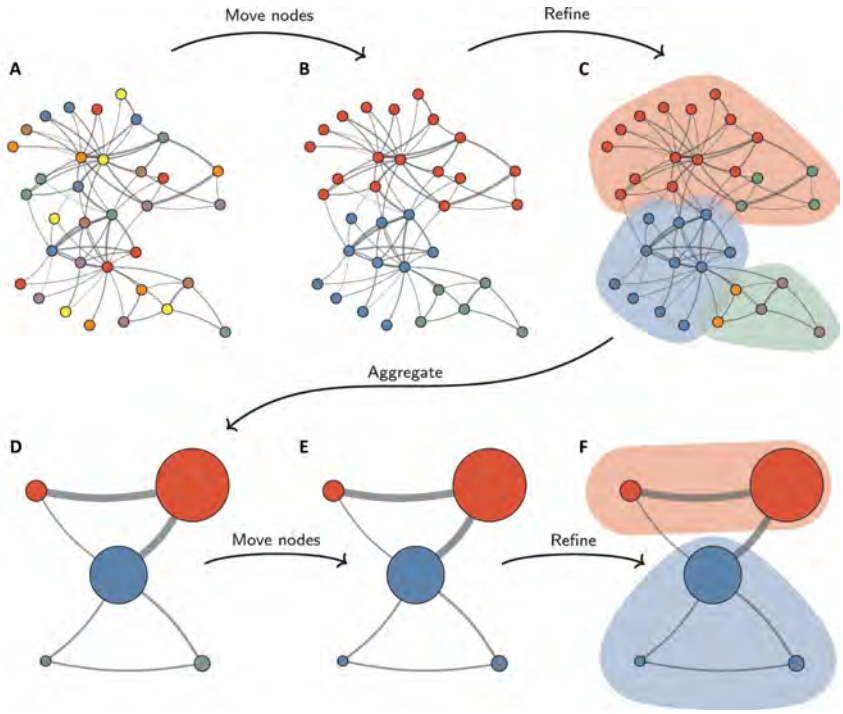

Figure 2.2: Workflow of the Leiden algorithm.
A) Initially, each node is assigned to its own community, **B)** nodes are then locally merged to form a partition **C)** that is successively refined. **D)** The aggregate network is constructed using the refined partition, taking the non-refined partition as the starting point to form an initial partition for the aggregate network. **E)** The aggregate network undergo nodes merging and **F)** refinement until no further improvement is achieved.
Adapted from [139].

The analysis was performed using dedicated Python libraries. The following function from the **'leidenalg'** library [139] has been used: *'find_partition'* to apply the Leiden algorithm on the weighted graph obtained from the giant component of the adjacency matrix. The partition type was *'ModularityVertexPartition'*, based on Equation 2.5. The intercommunities communication has been quantified

`https://leidenalg.readthedocs.io/en/stable/index.html`

by counting the number of edges between communities identified with the function *'has_edges'* of the **'networkx'** library.

2.1.3 Drosophila atlas

To validate the community detection algorithm on an annotated SBEM dataset, we used a recently published *Drosophila melanogaster* adult hemibrain connectome [53]. The achieved isotropic resolution was 8x8x8 nm and by automated segmentation algorithms more than 25000 neurons (approximately 25% of the total neurons in the Drosophila brain) have been reconstructed and their synapses (10^6) annotated.

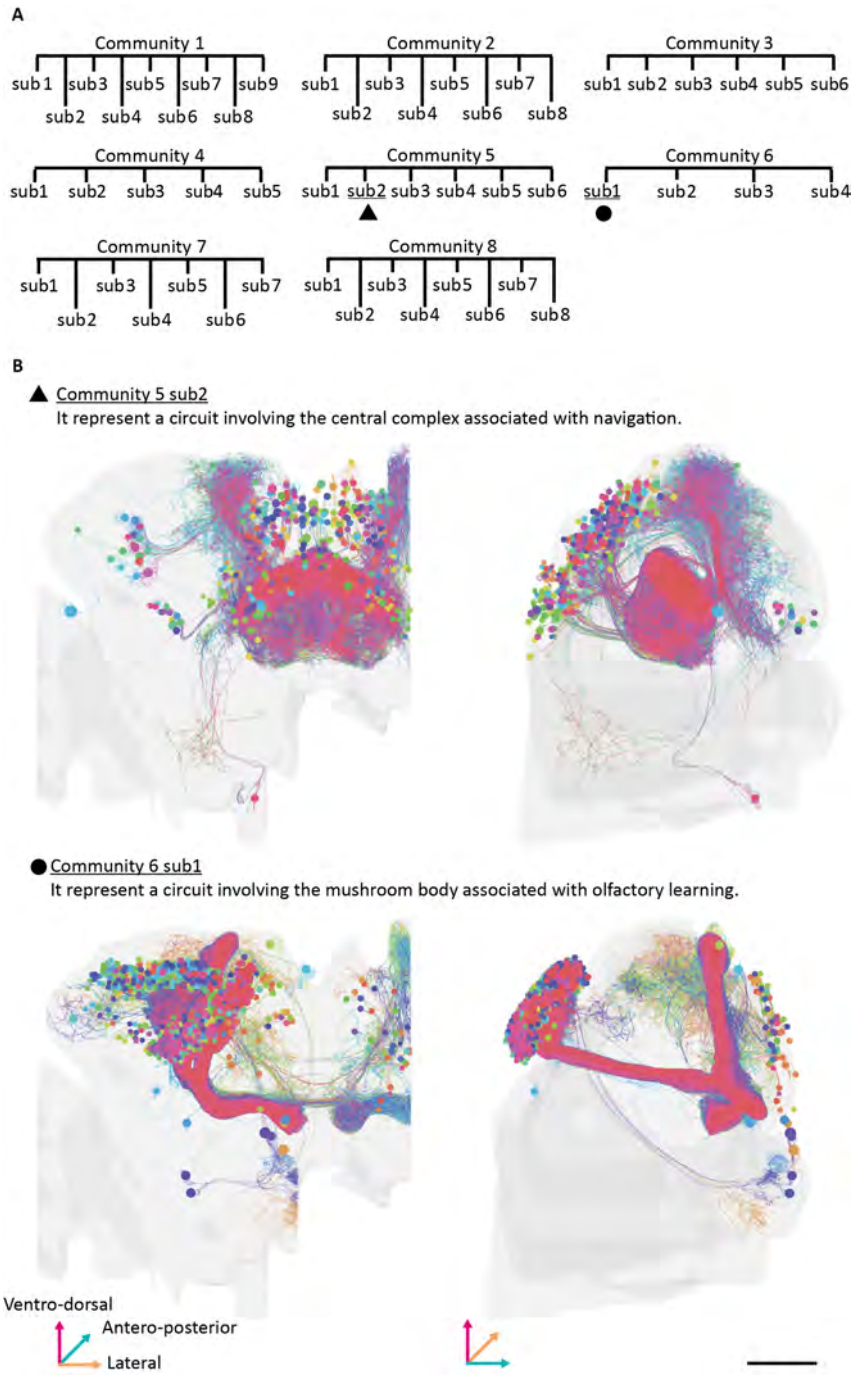

Figure 2.3: Network structure.
A) Tree diagram reporting the structure of the Drosophila connectome. **B)** Projections of the neurons found in two example subcommunities overlaid to the reconstructed hemibrain of the fly (template JRC-FIB2018F). Colors are assigned randomly.
Scale bar= 50 μm.

The size of the skeletonized dataset was approximately 5.2 GB. From the point of view of topological organization, the brain connectome has an average short path length of ~1.39, a weighted clustering coefficient of ~0.8 and the distribution of edge weights follows a power law distribution for intermediate-strength edge weights [121]. The application of the Leiden algorithm revealed the existence of eight main communities, each composed of a few thousands of cells (Figure 2.3). At this link (https://mt-bruzz.github.io/Drosophila_subcommunities/) you can navigate a couple of examples related to different subcommunities, work is currently in progress to share the complete analysis with the scientific community.

2.1.4 Zebrafish larval brain atlas

1: https://mapzebrain.org/home

A recently published zebrafish larva whole-brain atlas[1] has been used [27]. Currently, the constantly updating atlas comprises more than 3000 neurons, approximately 3% of the total neurons in the zebrafish larvae brain, but covering almost the complete brain, reconstructed anatomically (Figure 2.4A) by random and sparse GFP labelling under the control of BGUG (Figure 2.4B) or with other labelling techniques. With a typical resolution of 300x300x1000 nm (X,Y,Z), the size of the skeletonized dataset was approximately 60 MB. The reference brain was generated by co-registering the z-stacks of 12 brains from 6 days post-fertilisation (dpf) zebrafish stained for an antibody to Synapsin (SYP) using the advanced normalization tool (ANT) toolkit [140]. The reported median accuracy for the registration was 4.38 μm across the whole brain. The current reference brain contains two different channels, a 'live template' that contains a reference atlas for the calcium reporter *Elav3:H2B-GCaMP6s*, and a 'fixed template' with SYP. The anatomically reconstructed neurons and the designed anatomical regions are registered into the 'fixed template'. The functional template can be mapped in the fixed one by applying a set of anatomical transformations [141].

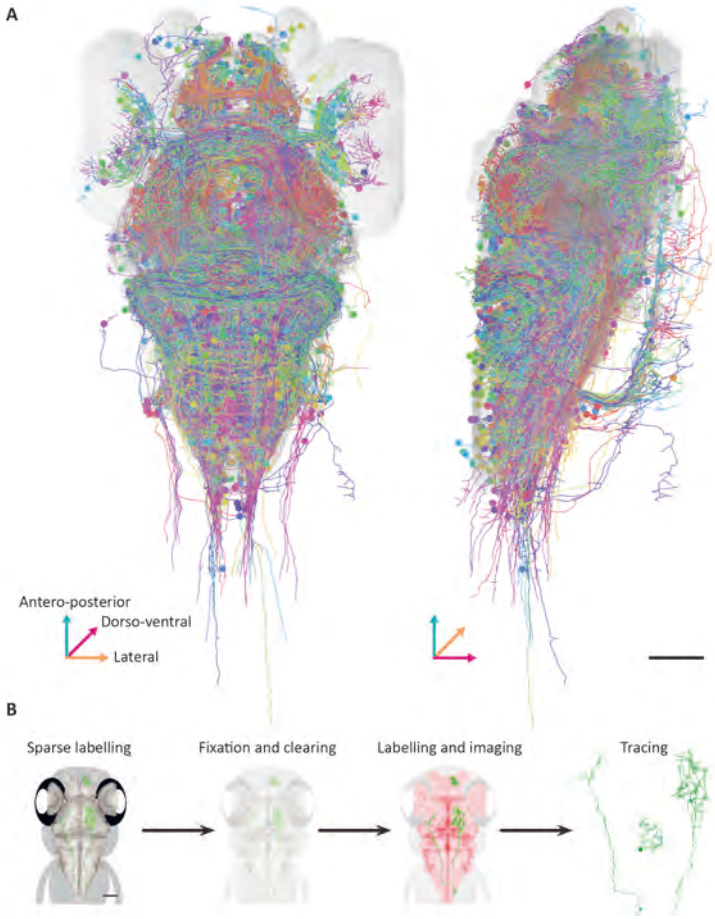

Figure 2.4: Zebrafish atlas.
A) More than three thousand anatomically reconstructed neurons overlaid to the zebrafish atlas (fixed template). Colors are assigned randomly. **B)** Workflow for generating single-neurons tracings. Adapted from [27].
Scale bar= 100 μm.

2.1.5 Generation of the zebrafish brain connectome

The mesoscale larval zebrafish brain atlas provides the reconstructions of more than 3000 neurons aligned on the same reference brain. However, it lacks information about the synapses between them, thus preventing the direct generation of a connectome. To overcome this limitations, we use as a proxy of potential connection between two neurons the proximity of their endpoints with a defined proximity range [142–144]. Connections are defined in the following way:

1. The neuron skeleton nodes were numbered using Strahler's numbering. The Strahler's numbering was originally developed to number the branches of streams. Basically, endpoints have Strahler's number (SN) = 1 and the nodes upstream of the ramification have $SN = i + 1$, where i is the highest SN of the branches downstream of the ramification.
2. Endpoints ($SN = 1$) of two different neurons that are within a proximity range of 5 μm are defined as connected. The 5 μm

proximity range was chosen to address inaccuracies in the anatomical reconstruction as outlined in the Subsection 2.1.4, to retain most of the network nodes in the giant component (Figure 2.5) and in accordance with a previous study that used a similar value [134].

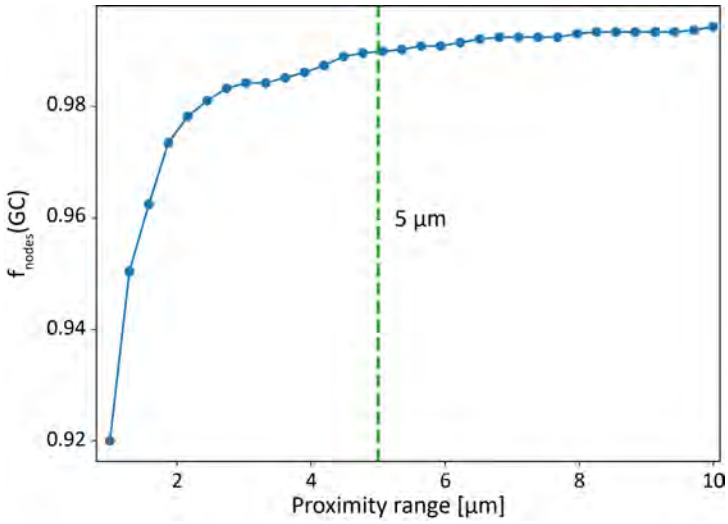

Figure 2.5: Relationship between the proximity range and the nodes in the GC.
A fraction of 0.99 of the total nodes of the network can be contained in the giant component (f_{nodes}(GC)) with a proximity range (green dashed line) of 5 μm.

To create a directed network, we classified the endpoints as either dendrites or axons. To accomplish this, we determined the Euclidean distance of each endpoint from the soma for each neuron. The resulting probability distribution is mostly bimodal, indicating that many of the endpoints are either close to or far from the soma. The probability distribution can be grouped into two main modal classes [145] (Figure 2.6A). We introduced a threshold, which corresponds to the local minimum between the two modes; endpoints that fall above the threshold were labeled as axons, while those below were labeled as dendrites (Figure 2.6B-C). In our analysis, if not otherwise stated, we use the undirected network and all kinds of connection are considered equal (i.e., axon↔dendrite, axon↔axon, dendrite↔dendrite) [58].

The analysis was performed using dedicated Python libraries.
The Strahler's numbering has been implemented with a custom-build function relying on the '**networkx**' [146] and '**numpy**' [147] librarys. The following function from the '**scipy**' [148] library has been used: *'spatial.distance.euclidean'* to calculate the euclidean distance between the endpoints of two distinct neurons.
Bimodal distributions have been classified according to the Galtung's classification method base on the endpoint spatial distribution and implemented with the R package *'agmrt'* [149].

https://numpy.org/
https://scipy.org/

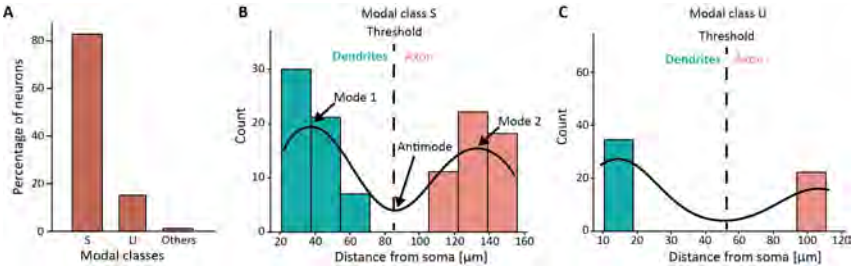

Figure 2.6: Distribution of endpoints of a neuron.
A) Typically the distance between the endpoints of a neuron and the soma is distributed accordingly to two main distribution classes. **B)** Bimodal class S. The antimode of the distribution is used to set a threshold (dashed line) to distinguish between dendrites and axon. **C)** Bimodal class U. The antimode of the distribution is used to set a threshold (dashed line) to distinguish between dendrites and axon.

2.2 Whole-brain recording of neuronal activity by multiphoton imaging

2.2.1 Light-based activity reporters and transgenic lines

Experiments were carried out according to the current legislation of our country (Decreto Legislativo 4 Marzo 2014, n.26) and were approved by the Ethical Committee of the University of Padua (61/2020_dalMaschio) and adhere to the ARRIVE (Animal Research: Reporting of In Vivo Experiments) guidelines. Larvae were raised at 28°C on a 12h light/12h dark cycle using standard procedures. *Elavl3:H2B-GCaMP6s* larvae were used for whole brain imaging, *galn:Gal4; UAS:NTR-mCherry; elavl3:H2B-GCaMP6s* larvae were used for both calcium recording in Galn^{+} neurons and whole brain imaging. Transgenic lines were kept in Tupfel long fin nacre (TLN) background, carrying a mutation suppressing the melanophore pigmentation. Five days post-fertilization (dpf) larvae were embedded in 2% low melting point agarose gel and used for experiments (Figure 2.7).

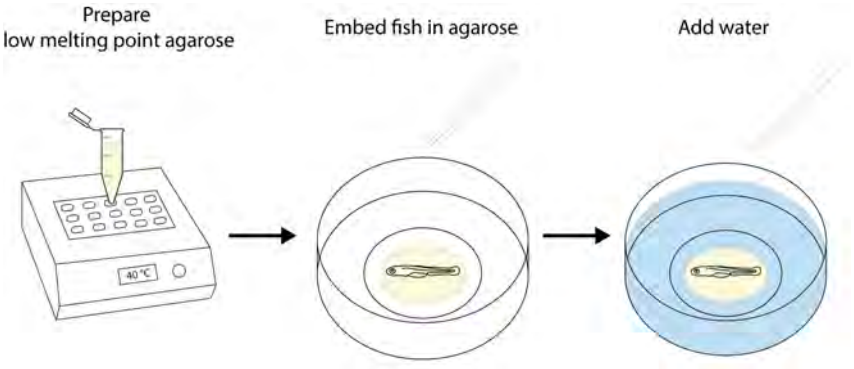

Figure 2.7: Fish preparation.
Workflow for embedding zebrafish larvae in 2% low melting point agarose gel.
Adapted from [150].

2.2.2 Hardware for two photons calcium imaging

The imaging process employs an 8 kHz galvo-resonant commercial two photon design (Bergamo I Series, Thorlabs, Newton, NJ, United States). The system uses a Ti:Sapphire source (Chameleon Ultra II, Coherent) tuned at 920 nm for GCaMP6 imaging. Imaging is performed using a water-dipping Nikon CFI75 LWD 16X W objective. The fluorescence collection path includes a 705 nm long-pass main dichroic, an IR blocking filter, and a 495 nm long-pass dichroic that directs the fluorescence light to a highly sensitive GaAsP photomultiplier (PMT) detector (H7422PA-40 from Hamamatsu) with a EM525/50 emission filter. The PMT signal is sampled at 400 MHz by a fast digitizer board (Alazar Tech Board) and the images, with a resolution of 1024 x 512, are acquired at 30 frames per second and stored on a PC in a *.raw* file format. The microscope control unit (MCU) provides the analog waveforms for driving the galvo-resonant scanner and other Transistor-Transistor Logic (TTL) signals, including a 30 Hz Frame Sync TTL signal that marks the start of the image acquisition along the slow axis (Y) and is used to synchronize the ETL scanning. Moreover, the acquisition can be controlled and triggered by an external TTL signal.

2.2.3 Electrically tunable lens implementation

To perform volumetric imaging, an electrically tunable lens (ETL)[2] was implemented upstream of the x/y scanner, in a plane optically conjugated with the back focal plane (BFP) of the objective. The ETL was powered by the Optotune Lens Driver 4i and could be controlled in two ways - through a PC using proprietary software via a USB connection or by external analog and serial signals. The latter was achieved by integrating a commercially available microcontroller, an Arduino Mega 2560 [3], that sent serial commands to the ETL driver through the universal asynchronous receiver-transmitter (UART) interface.

The wiring is performed as follows. Pin 47 of the microcontroller corresponds to the counter input and is connected to the "Frame Sync" TTL (0-5 V) output of the MCU via a coaxial cable (Figure 2.8 - lime line). Pins 18 and 19 are, respectively, TX and RX of the UART serial port 1; they are connected to the corresponding

2: Optotune EL-10-30-C-IR
https://www.optotune.com/el-10-30-c-lens

3: Arduino Mega 2560
https://store.arduino.cc/products/arduino-mega-2560-rev3

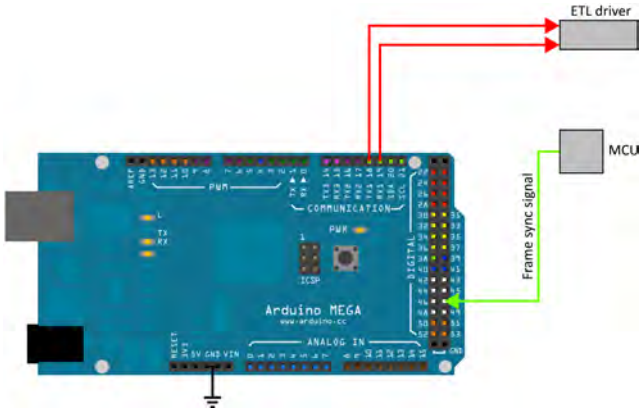

Figure 2.8: Microcontroller wiring. The microcontroller receives "Frame Sync" TTL (0-5 V) inputs from the MCU (lime line) and sends outputs to the ETL driver (red lines). Arrows indicate the direction of the signals.

RX/TX pins of the UART serial port of the ETL driver (Figure 2.8 - red lines). The ground (GND) is connected to the GND of the microscope.

The microcontroller accepts as input the frame clock signal from the MCU. This signal, Frame Sync, marks the beginning of the scanning along the slow axis (Y) and is used to increment a digital counter implemented in the microcontroller. The microcontroller repeatedly sends to the ETL driver, at the maximum possible rate (every 3 ms in our case), the commands to update the value of the current *I(t)* which in turn controls the focal power of the lens. This is computed from a 5^{th} order polynomial that interpolates the points of a LUT obtained during a calibration phase. The calibration procedure envisages the acquisition of a series of images of the same field of view, every time with different currents driving the ETL. The corresponding *z*-shift of the objective arm to bring the FOV back into focus represents a measurement of the focal shift introduced by the ETL. This set of *z(I)* points is used to generate the LUT (Figure 2.9).

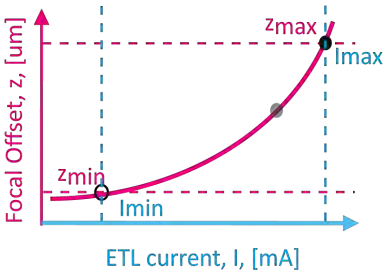

Figure 2.9: ETL Look-Up-Table (LUT). Relationship between the input current to the ETL (blue axis) and the change in the focus resulting at the level of the sample (magenta axis). Adapted from [135].

First, the z values are remapped to z^* in the range 0–1. Then, the corresponding values of current $I(z^*)$, where $I(z^* = 0) = I_{\min}$ and $I(z^* = 1) = I_{\max}$, are fitted with a 5^{th} order polynomial, whose coefficients $p0, \ldots, p5$ are then loaded into the microcontroller. This

is programmed to continuously generate a sawtooth waveform, $z^*(t)$ (where t is an internal high-resolution timer), spanning the range 0 to 1 in the desired number of counted frames, 30 in our case. The corresponding currents $I(z^*(t))$ are calculated from the coefficients $p0, \ldots, p5$ and commands are sent to the ETL driver to update the output current. Furthermore, the microcontroller periodically sends the total number of frames counted to the PC, which is used to synchronise the stimulation protocol.

2.2.4 Optical performance measurement

The PSF was determined by acquiring z-stacks of 0.2 μm diameter fluorescent polystyrene beads at eight different positions, with a z-range between 0 and 233 μm, by mechanically move the objective. The z-stacks were analyzed using the Fiji distribution of ImageJ software [4]. The first step involved reslicing the images along the x/y or z axis (Image → Stacks → Reslice), followed by a z-projection (Image → Stacks → Z Project) to produce an average intensity slice. The fluorescence of the beads was determined by using the "plot profile" function in the software (Image → Stacks → Plot Z-axis Profile). The FWHM was calculated as:

4: https://imagej.net/software/fiji/

$$FWHM = 2\sqrt{2\ln 2} * \sigma$$

where σ is the standard deviation of the fluorescent profile of the beads. The FOV dimensions were measured by annotating the μm travel of the piezo actuator to shift a fluorescent bead from one side of the FOV to the other along the given axis.

2.2.5 Visual stimulation

The stimuli were displayed at 60 Hz using a Texas Instrument DPL4500 projector[5] with a magenta Wratter filter to eliminate light interference with fluorescence detection. The projector was placed 20 cm from a 50 × 50 mm screen positioned 3 cm from the subjects. The stimulation sequence was initiated based on the frame count of the microscope, which allowed for precise alignment between the visual stimuli and the imaging acquisition. A single dot, which expanded from 0 mm to 50 mm in 17 seconds, was presented in

5: https://www.ti.com/tool/DLPLCR4500EVM

the center of the fish's field of vision. The time taken for the dot to expand to half its final size was 8.3 seconds, the final angle size was 79.4° and the rate of angular expansion was 9.5°/s. The stimulus was repeated 10 times with an interval of 150 seconds between each presentation.

Visual stimulation was performed in Python.
The following function from the '**stytra**' library [151] has been used: *'LoomingProtocol'* to generate the looming stimulus. The following functions from the '**serial**' library has been used: *'Serial'* to initialize communication between the visual stimulation script and the microcontroller and *'read'* to read incoming data from the microcontroller (i.e. frame number).

https://www.portugueslab.com/stytra/
https://pythonhosted.org/pyserial/index.html

2.3 Identification of stimulus responsive cells

2.3.1 Data analysis

The time series were acquired at an acquisition rate of 1 volume per second and with a spatial resolution of 1024 × 512 pixel. To prevent focus shifting from the lens's thermal drift, the first few minutes of the acquisition were discarded. The raw data with interleaved planes underwent plane-by-plane motion correction to minimize lateral motion and was smoothed using a short window running average filter (3 frames). The filtered data were processed using suite2p[6], an automatic cell segmentation tool, which used a cell classifier trained on similar datasets [152]. The process generated various output files, with the most important being the 'stat.npy' file that contained information about each segmented cell and the 'F.npy' file with the respective fluorescence levels over time. After the automatic segmentation process was completed, the datasets were manually reviewed to assess the quality and accuracy of the ROI classification. Typically, between 5% and 10% of cells were not accurately segmented during the acquisition process; on the other side, less than 5% of identified ROIs did not correspond to a recognizable cell. These errors were manually corrected to produce a clean dataset, which typically consisted of 30,000 to 50,000 correctly identified neurons.

6: https://github.com/MouseLand/suite2p

2.3.2 Regressor analysis

The neurons active during visual stimulation were identified through a regression-based analysis [153]. Binary waveforms were created to represent the different presentations of the visual stimulation. These temporal waveforms present most of the time a zero level baseline and transitions to one at the onset of the stimulus presentation. The level remain at 1 during the stimulus presentation, to return at the baseline level at the end of the specific stimulus presentation (Figure 2.10A). The typical stimulation protocols envisages the presentation of different visual stimuli interleaved with a sufficient time interval so to have the activity returning close to the baseline level. This implies that for each acquisition, one can fit the neuronal activity profile with a linear combination of opportune regression functions, each corresponding to a different phase of the stimulation. We adopted a kernel function that approximate the decay kinetic of the fluorescence signal of the reporter over time. The kernel is usually described by a normalized exponential decay function:

$$K_c = e^{\frac{-t}{\tau_{off}}} \frac{1 + sign(t)}{2} \tag{2.6}$$

where τ_{off} is the decay kinetic of the reporter, in our case 5 seconds, and t is the time interval to construct the window function, in our case 30 seconds, and $\frac{1+sign(t)}{2}$ is a correction factor for the rise phase of the fluorescence signal. Each binary waveform corresponding to a different regression function was then convolved with the kernel to produce a regressor that resembles as much as possible the expected temporal dynamic of the fluorescence signal [153] (Figure 2.10B). The activity of each neuron was normalized, via z-score, over its duration. The z-scored activity y was fit to the regressors with a linear model described by:

$$y \simeq \hat{y} = cx \tag{2.7}$$

where $\hat{y}$ is the resulting approximation for the activity y, c is a vector of coefficients and x is the panel of the regressors (Figure 2.10C).

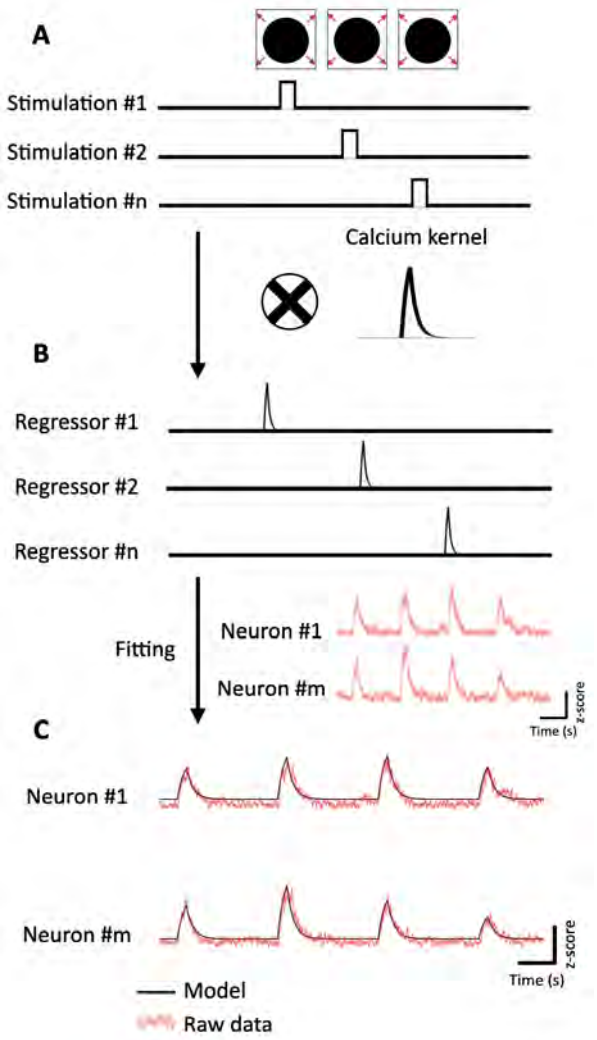

Figure 2.10: Regression-based analysis.
A) The binary waveforms are created to represent the presentation of the stimuli. These temporal waveforms present most of the time a zero level baseline and transitions to one at the onset of the stimulus presentation. **B)** Each binary waveform corresponding to a different regression function was then convolved with the kernel to produce a regressor. **C)** The z-scored activity was fit to the regressor with a linear model

Then it is computed the mean squared error, a metrics that corresponds to the average quadratic differences between the linear model and the real data. It is described by:

$$MSE(y, \hat{y}) = \frac{1}{n_{samples}} \sum_{i=0}^{n_{samples}-1} (y_i - \hat{y}_i)^2 \tag{2.8}$$

where y is the real data, the cell activity, and $\hat{y}$ is the corresponding regressor-based reconstruction of the cell activity. The samples, in this case, are the frames. For each neuron, the coefficient c obtained from Equation 2.7 is divided by the MSE obtained from Equation 2.8 to obtain a score describing the fidelity of description of the neuron activity by the regressor. Given that the MSE is taken in consideration, the score is susceptible to non-stimulus related activation of the cell. Neurons whose score were within the top 5% of the scores distribution were considered as stimuli-responsive and

isolated for further analysis. To identify populations of functionally distinct neurons, they were grouped with the agglomerative clustering algorithm using as a linkage criterion the Ward method. The algorithm starts by considering each neuron as an isolated cluster and sequentially merge neurons in the same cluster whether the merging leads to the minimum increase of variance in the cluster. The variance computation is based on the Lebesgue 2-norm (L_2-norm, i.e. the squared euclidean distance) between two cluster center:

$$d_{ij} = \| X_i - X_j \|^2 \tag{2.9}$$

The analysis was performed using dedicated Python libraries. The **'numpy'** library has been used to design the kernel described in Equation 2.6. The following function from the **'scikit-learn'** library [154] have been used: *'linear_model.LinearRegression'* to compute the coefficients of the regression as Equation 2.7, *'metrics.mean_squared_error'* to compute the MSE as Equation 2.8 and *'cluster.AgglomerativeClustering'* to identify population of functionally distinct neurons as Equation 2.9.

https://scikit-learn.org

2.4 Bringing functional information on the anatomical space

Following the acquisition of the time series, a reference z-stack was recorded as reference for the anatomical registration (from now on referred to as the z-stack). The resolution was 1024 x 512 pixels with a spacing between the planes of 1 μm and the sampling rate was 0.03 Hz per plane. The acquired z-stack is saved with pixel measurement unit and prior the registration it must be converted to μm. The conversion value between pixels and μm is provided in the 'Experiment.xml' file produced by the microscope software at the end of the acquisition.

2.4.1 Registration of recorded fish on the anatomical reference brain

Registration is the process of converting an image to match the space coordinates of a reference one. The *'antsRegistration'* command in ANTs was used to register the z-stack to the reference

live channel of the atlas. To achieve optimal registration, a set of algorithms are used [7]:

1. a 'rigid' transformation, in which the image to register is moved and rotated to align it with the template
2. an 'affine' registration that allows also non-rigid transformations as shearing and scaling
3. a symmetric normalisation (SyN) that account for non-linear transformations

Steps are iterated with increasing resolution for better performance. To measure the accuracy of the registration, the registered stacks have to be manually inspected for successful alignment, this is typically done by evaluating the matching in the superimposition of the registered stacks with the atlas template (Figure 2.11). Next, we identified various neurons in the reference channel of the standard brain that were also present in the registered stacks and saved their x, y, z coordinates in Fiji/ImageJ. The calculated distances had a median of 5.84 μm, comparable to the cell diameter.

7: For an exhaustive explanation of the individual parameters please refer to https://github.com/ANTsX/ANTs/wiki/Anatomy-of-an-antsRegistration-call

Figure 2.11: Anatomical registration.
Example of the anatomically registration between the z-stack of a *Elav3:H2B-GCaMP6s*-expressing fish and the 'live template' of the atlas.

2.4.2 Registration of functionally-identified neurons on the anatomical reference brain

The 'stat.npy' obtained from suite2p (Subsection 2.3.1) contains information about each segmented cell. The coordinates of center of mass are contained in the entry 'med' in the y,x format. A custom Python script based on the function *'feature.match_template'* of the **scikit-image** library matches, for each t-series plane, the most similar z-stack plane to extract the z coordinate. Furthermore, the results are manually checked to correct the eventual errors that can occur when two t-planes are similar. At the end of the process, a list containing anatomical information (x,y,z) of each cell is obtained.

https://scikit-image.org/

Prior to the registration of the cells into the atlas, cell coordinates are transformed by using the conversion value between pixel and μm provided in the 'Experiment.xml' file (Subsection 2.4.1). Moreover, moving from suite2p to the z-stack generates a flip of the coordinates along the short axis that must be corrected. To be sure that the cell coordinates align well with the z-stack, we found effective to plot some of them superimposed on their respective plane of the z-stack. At this point, cells can be registered in the live template using the command 'antsApplyTransformToPoints'. The *'antsRegistration'* command (Subsection 2.4.1) generates a '0GenericAffine.mat' file and a '1InverseWarp.nii.gz' file necessary to the command *'antsApplyTransformToPoints'* to convert the cell coordinates to the anatomical space of the live template. Subsequently, the coordinates aligned with the live template were mapped onto the fixed template containing the anatomically reconstructed cells.

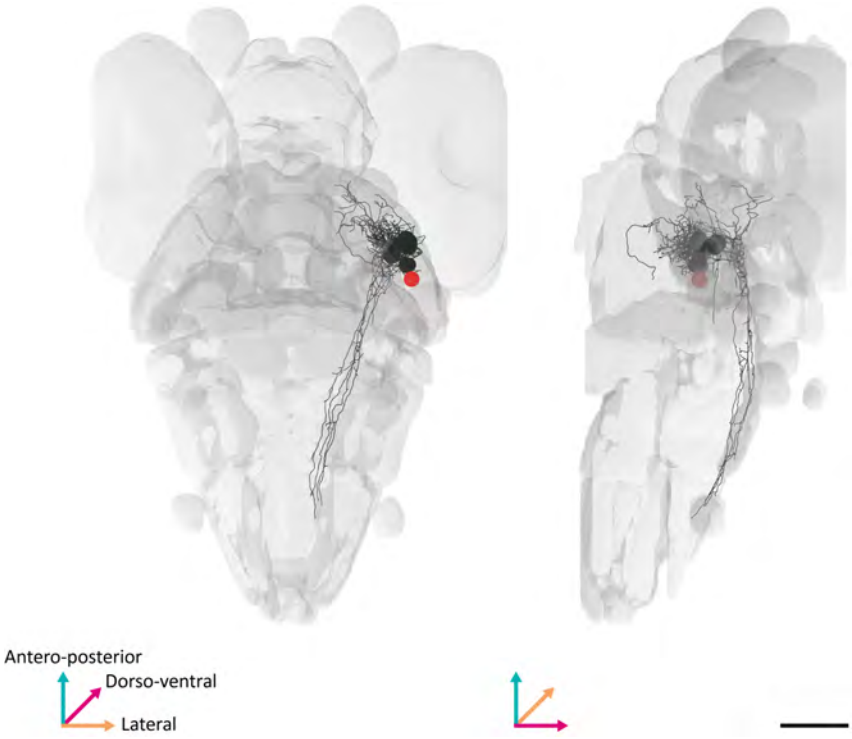

Figure 2.12: Registration of functionally-identified neurons on the anatomical reference brain.
Example of a functionally recorded neuron (red) mapped onto the fixed template of the brain atlas. In black are reporter the anatomically reconstructed that are spatially located within a range of 50 μm from the functionally recorded neuron.
Scale bar= 100 μm.

2.4.3 Segmentation of Chr$^+$-neurons

For the work in collaboration with the lab of Alessandro Filosa [155], we took advantage from the combination of volumetric imaging and anatomical registration of functionally characterized neurons. In particular, the goal in this work was to identify a possible relation in the activity between a subpopulation of hypothalamic neurons

releasing Galanin (*galn*) and a population of pretectal neurons expressing corticotropin releasing hormone b (*crhb*$^+$). While it was possible to identify Galn$^+$-neurons during the functional imaging sessions in the *galn:Gal4; UAS:NTR-mCherry; elavl3:H2B-GCaMP6s* line, for identifying the Crhb$^+$-neurons the only method available is currently the in situ mRNA hybridization. So, to link these two pieces of information, we registered using the GCaMP channels on the same reference brain the z-stacks acquired at the the end of the functional imaging session and the z-stack acquired post fixation with the in situ reporter. To segment Chr$^+$-neurons, a sub-stack containing the preoptic area and the *chr*$^+$ signal was obtained from the whole brain z-stack of the fixed fish (Figure 2.13A). Neurons identification was performed on the sub-stack using a custom Python script based on the *'feature.peak_local_max'* function of the **'skimage'** library. These peaks typically corresponded to identified cells, as indicated by the arrowheads in Figure 2.13A. The coordinates of the identified peaks were then aligned, using the *'feature.match_template'* function, with the system coordinates of the whole brain fixed z-stack used for the anatomical registration (Figure 2.13B).

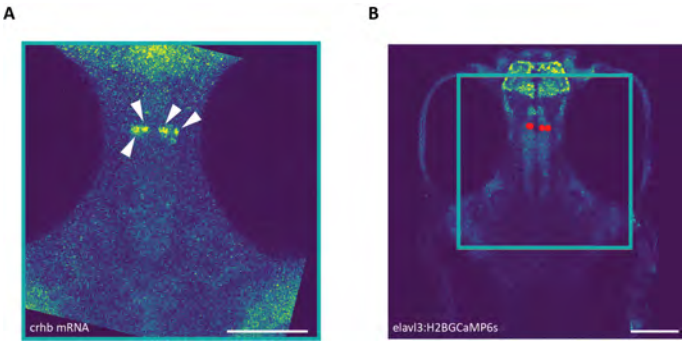

Figure 2.13: Segmentation of Chr$^+$-neurons
Example of a functionally recorded neuron (red) mapped onto the fixed template of the brain atlas with anatomically reconstructed neurons (black) within a range of 50 μm. Scale bar= 100 μm.

2.4.4 Analysis of Chr$^+$- and Galn$^+$-neurons responses

The classification of neurons was based on the changes in the number of Ca^{2+} events after exposure to NaCl compared to before. Neurons were categorized as having "increased activity" if there was a 5% or more increase in the number of events, as "decreased activity" if there was a reduction of at least 5%, or as "non responsive" if the frequency of Ca^{2+} events changed by less than 5%.

Results: Analysis of the zebrafish larva brain wiring diagram

3

Understanding how the structure of the nervous system supports information flow is a challenging problem, and the anatomical reconstruction of neurons provides a valid support to design hypothesis on circuit wiring diagram.

In the following subsections, a modularity-based network analysis algorithm is applied to detect neuronal communities in the structural connectome dataset of the zebrafish larvae. Prior to this, we validated it on the annotated EM-dataset of the Drosophila hemibrain (Methods 2.1.3). The Leiden algorithm has been shown to provide superior guarantees on the density of discovered communities and effective connectivity [139]. Although this approach has been widely used, it has not previously been applied to the study of whole brain organization from a structural perspective.

3.1 Building the zebrafish larva brain connectome

Recently, the SBEM reconstruction of the zebrafish larvae brain has been published [29]. This represents the first EM-dataset for the whole brain of a vertebrate. However, no brain-wide connectome is available, yet. To overcome this limitation, we generated a cell resolution connectome for the zebrafish larve using a dataset of single cell anatomical reconstructions [27] and a rule based on a proximity range to define putative connections between cells. As discussed in Methods 2.1.5, the Strahler number, a measure of the position of a point in the cell branching hierarchy, was calculated for each point on the cell skeleton (Figure 3.1A). Terminal points, which have a unitary value of the Strahler number, were considered to be potential points of connection between different cells if they fell within a proximity range of 5 μm (Figure 3.1B). The 5 μm proximity range was chosen based on 1) reports dealing with connectome reconstructions [134] and 2) to account for eventual error due to the accuracy of the anatomical reconstruction (Methods 2.1.4). The connectome was then constructed by calculating the adjacency

matrix, which was assumed to be undirected (Methods 2.1.2). The obtained adjacency matrix was re-arranged in order to group together neurons with the soma belonging to the same anatomical regions (Figure 3.1C).

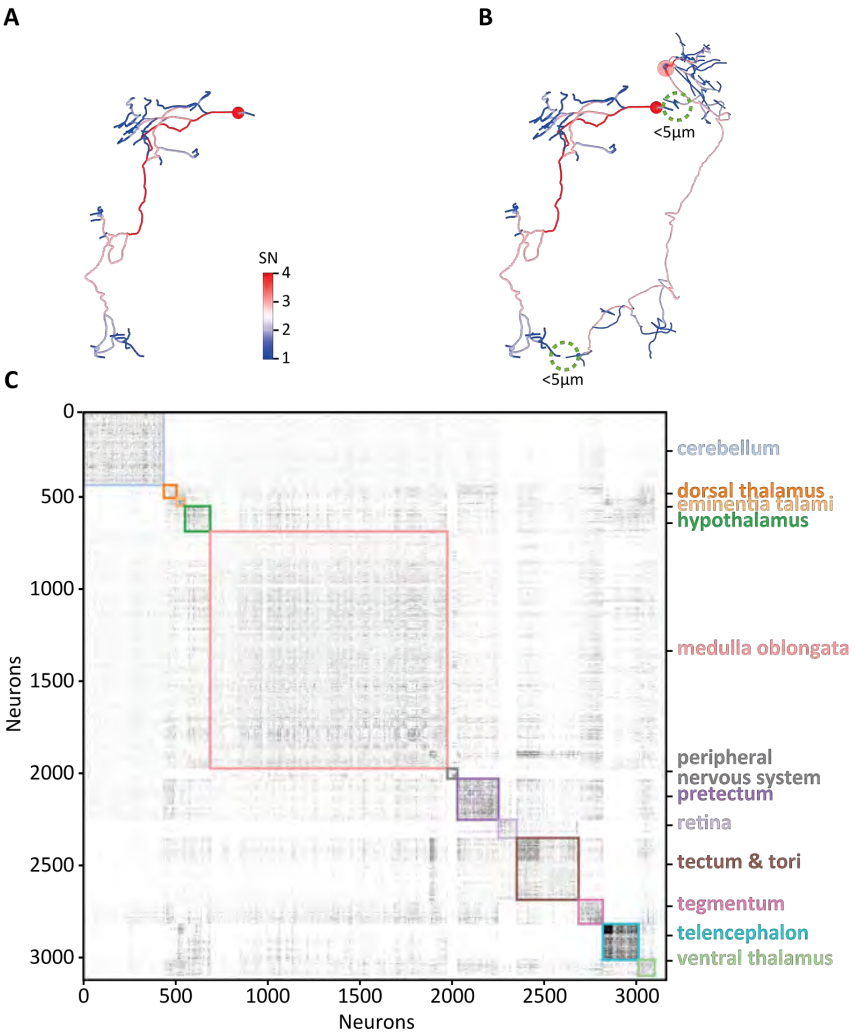

Figure 3.1: From neuronal reconstructions to a connectome.
A) Anatomically reconstructed neuron color-coded with the Strahler number. The soma is represented as a circle and it display the highest SN possible. **B)** Example of connections between two neurons whose endpoints (SN=1) are closer than 5 μm. **C)** Binarized adjacency matrix showing connections between neurons sorted by brain regions in which the soma of the neurons are located. The matrix is binarized (i.e. 1: connection/s, 0: no connection) for visualization purpose.

3.2 Topological properties of the zebrafish connectome

The analysis of the adjacency matrix revealed the existence of 23 subgraphs, with a giant component (GC) accounting for 99% of the edges of the original graph and a set of small poorly populated disconnected subgraphs (accounting for 32 out of total 3163 nodes), that have been neglected from further analyses. The GC presents a network density of 0.0397, pointing to a rather limited connectivity, a small weighted clustering coefficient of 0.00203 and an average

shortest path length of 3.792. The graph has an heterogeneous degree distribution, with most of the nodes characterized by a relative small number of degree (<10^3) and a fewer ones with a high number of degrees (>10^4) defined hubs (Figure 3.2A). Interestingly, in the small degree region the distribution shows a flat trend, suggesting that this graph deviates from the power-law behavior (Figure 3.2A). An assortativity analysis returned a correlation coefficient β of 0.345, meaning that the graph is assortative (i.e. the nodes tend to connect with other nodes with similar number of degrees). As for the hubs, when we mapped them to the corresponding anatomical regions normalizing for the relative number of cells, it appeared that the majority belongs to medulla oblungata, followed by the telencephalon and the optic tectum (Figure 3.2B).

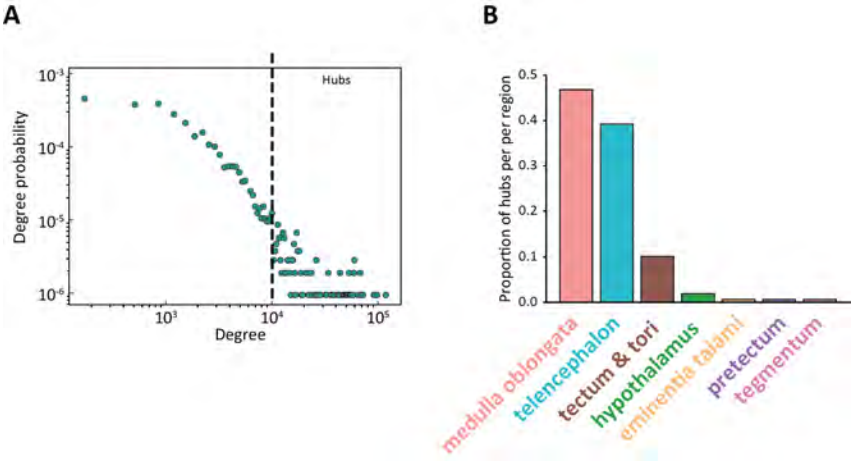

Figure 3.2: Topological properties of the connectome.
A) Weighted degree distribution. Each green dot represent a bin in the binned probability distribution. **B)** Histogram representing the distribution of hubs (number of connections >10^4) in the brain regions.

3.3 Identify the communities and the associated properties

Modules or communities are a common feature of brain networks, and modularity is often used as a measure of their presence [156]. Here, the Leiden algorithm is applied to detect communities by maximizing modularity in the zebrafish connectome. Running the algorithm 10,000 times in the undirected adjacency matrix generally resulted in a stable and robust identification of 12 neuronal communities, with little deviation in the assignment of several nodes from one trial to another (<0.5 %) (Figure 3.4). Among the neuronal communities, five contained an extremely limited number of neurons and were discarded (Figure 3.4A). The remaining

seven communities were assigned to the brain regions containing their soma to investigate the topology (Figure 3.4B). As a control, we applied the community detection algorithm at the directed adjacency matrix, we obtain communities that are in line with the ones from the undirected adjacency matrix (Figure 3.3). The only major difference was that two undirected communities were merged in one directed community.

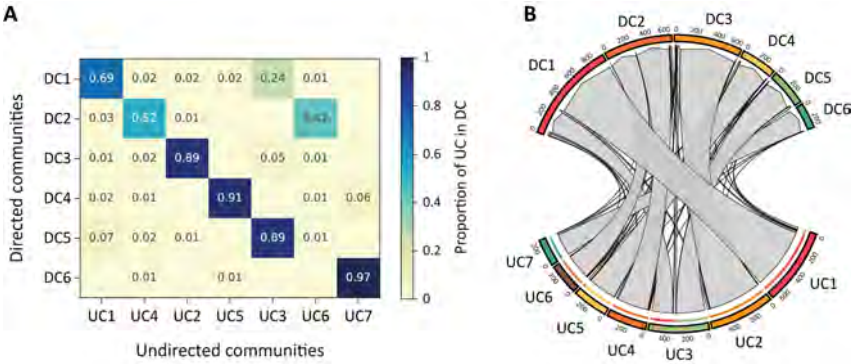

Figure 3.3: Organization of the community structure for the directed and the undirected connectome. **A)** Proportion of node of the undirected communities present in the directed communities. **B)** Number of node of the undirected communities present in the directed communities.

The neuronal communities identified exhibit distributed spatial patterns that cover multiple brain regions in a nonexclusive manner. Most brain regions are associated with more than one community (Figure 3.4C). To better understand the organization of these communities, we applied the community identification algorithm to each identified community to reveal finer network patterns, leading to the discovery of subcommunity patterns (Figure 3.4D) that capture additional levels of circuit organization involving spatial segregation of neuronal populations within brain regions and anatomical connections between different functionally characterized brain areas.

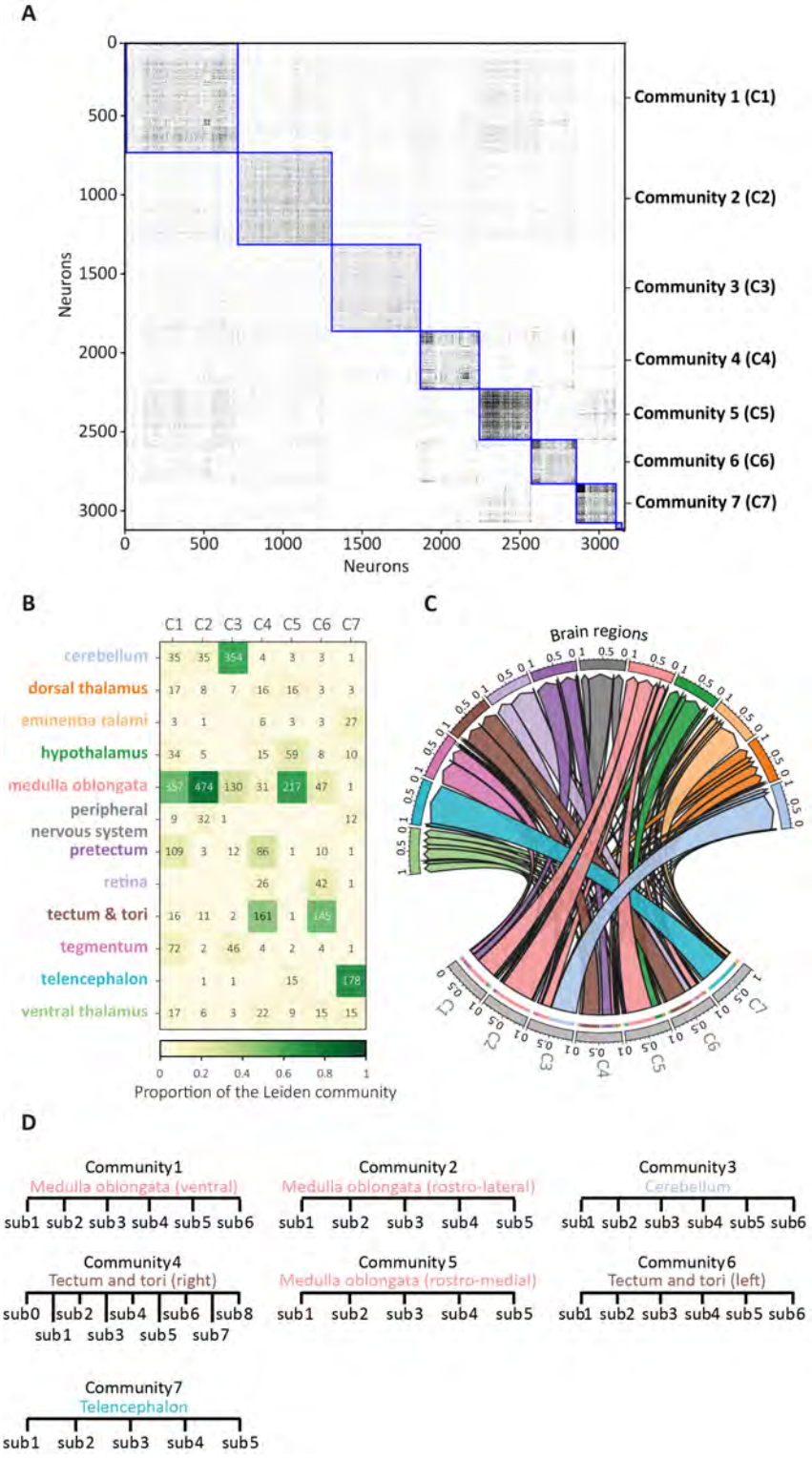

Figure 3.4: Distribution of the communities in the brain and network structure.
A) Binarized adjacency matrix showing connections between neurons sorted by identified communities. The matrix is binarized for visualization purpose. **B)** Distribution of the communities across the brain regions. Numbers refers to the neurons belonging to a certain community and with the cell body in corresponding regions. Matrix cells are color-coded based on their proportion within the community. **C)** Proportion of the distribution of the communities across the brain regions. **D)** Tree diagram reporting the structure of the zebrafish connectome. For each community, the most represented brain region is reported.

3.3.1 Community 1

It is mainly represented by neurons in the medulla oblungata, pretectum, tegmentum, cerebellum and hypothalamus (Figure 3.5A).

Neurons located in the vagal motor nucleus (VMN) convey motor information to peripheral nuclei (Figure 3.5B, Supplementary Figure 7.1). These connections are involved in branchiomeric muscles innervation [157]. Neurons located near the arborization field 7 (AF7) in the pretectum form connections with the gabaergic part of the nuclei isthmi (NI) (Figure 3.5B, Figure 7.4, Supplementary Figure 7.5). These connections are involved in the tracking of prey during hunting behavior [158]. Pretectum neurons that project to the cerebellum are part of direction-selective neurons, located near AF4, associated with motion-opponent responses (Figure 3.5B, Supplementary Figure 7.6) [141].

In summary, neurons in community 1 are involved in innervation of branchiomeric muscles, motion-opponent responses and prey-tracking.

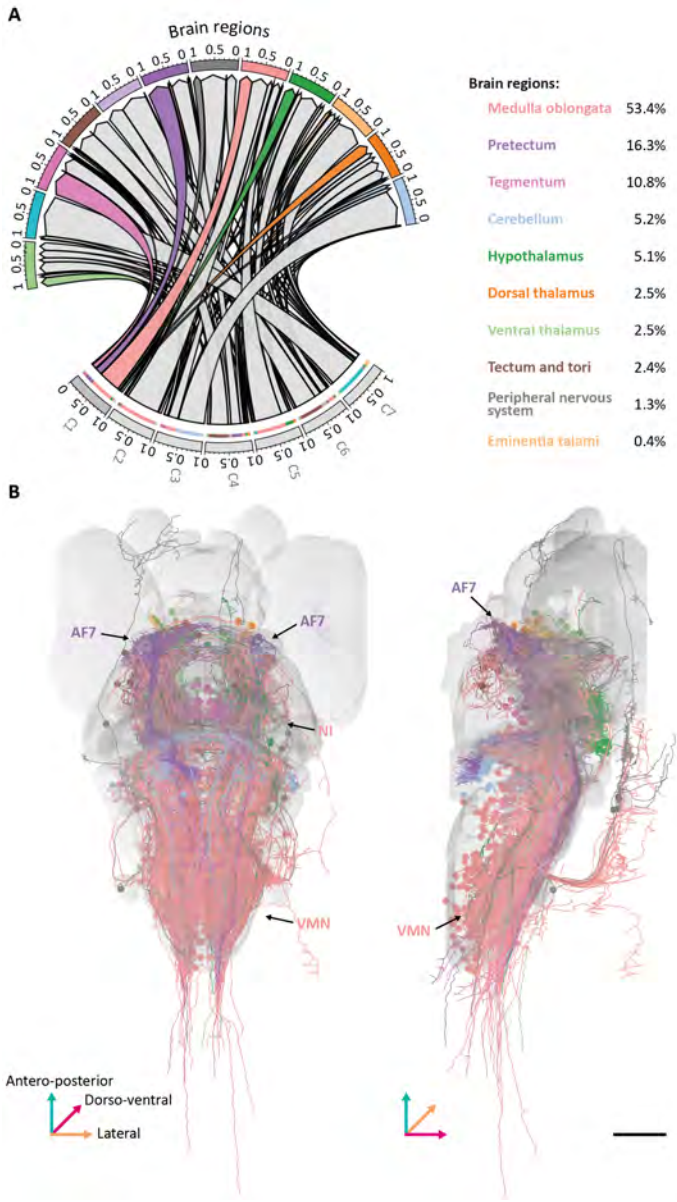

Figure 3.5: Community 1.
A) Neurons are distributed across multiple brain regions at different amounts. **B)** Projections of the neurons found in the community. Colors are assigned based on soma location. VMN: vagal motor nucleus, AF7: arborization field 7, NI: nuclei isthmi. Scale bar = 100 μm

3.3.2 Community 2

It is mainly represented by neurons in the medulla oblungata, cerebellum and peripheral nervous system (Figure 3.6A).

Neurons located in the posterior lateral line ganglion (pLLG) and the octaval ganglion (OG) form connections with the medial octavolateralis nuclei (MON) (Figure 3.6B, Supplementary Figure 7.7). These connections are involved in the detection of water flow [159, 160]. Connections between gangliar neurons and the eminentia granularis (EG) of the cerebellum also contribute to this process [161]. Neurons located in the MON and nearby regions (Figure 3.6B, Supplementary Figure 7.8, Supplementary Figure

7.10) provide non-retinal inputs to the deep layers of the tectum [161–163] as well as neurons located in the glutamatergic part of the NI (Figure 3.6B, Supplementary Figure 7.9) [27]. These non-retinal inputs to the tectum could subserve rheotaxis [163].

In summary, neurons in community 2 are involved in the processing of sensory input from the lateral line system and the projection of this information to the optic area. These neurons may be involved in the detection and interpretation of water flow.

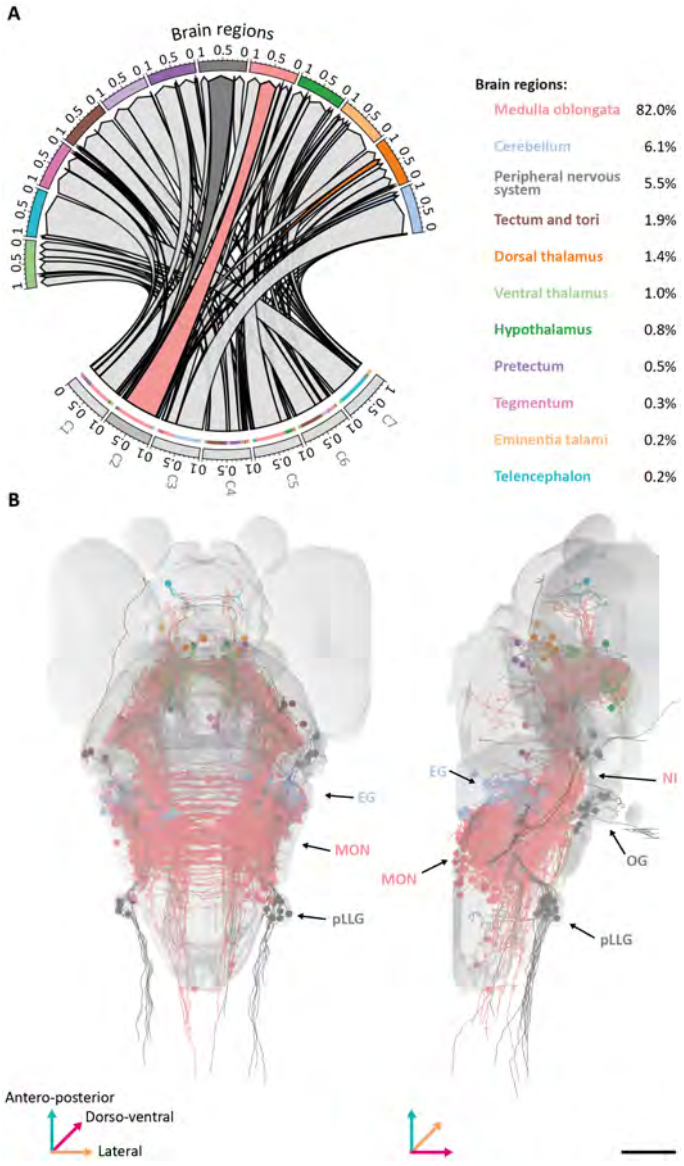

Figure 3.6: Community 2.
A) Neurons are distributed across multiple brain regions at different amounts. **B)** Projections of the neurons found in the community. Colors are assigned based on soma location. EG: eminentia granularis, MON: medial octavolateralis nuclei, NI: nuclei isthmi, OG: octaval ganglion, pLLG: posterior lateral line ganglion. Scale bar = 100 μm

3.3.3 Community 3

It is mainly represented by neurons in the cerebellum, medulla oblungata and tegmentum (Figure 3.7A).

The connections formed between neurons located in the medulla oblongata, cerebellum, and tegmentum (Figure 3.7B, Supplementary Figure 7.14, Supplementary Figure 7.15) are associated with vestibulo-ocular reflex (VOR) [164]. The ascending and ascending / descending tangential neurons are located in the medial octavolateral nucleus (MON) in the medulla (Figure 3.7B, Supplementary Figure 7.14, Supplementary Figure 7.15), the recipient of utricular input. These neurons project to the controlateral trochlear nucleus (nIV), the oculomotor nucleus (nIII), and the nucleus of the medial longitudinal fasciculus (nMLF), where extraocular motor neurons mediate gaze stabilization [164]. Furthermore, connections between neurons located in the cerebellum have been shown to be involved in VOR [165, 166]. The cerebellum displays a spatially segregated pattern of distinct cells, with lateral Purkinje cells that project to the MON (Supplementary Figure 7.13) and eurydendroid cells located in the middle with less specific projections (Supplementary Figure 7.12, Supplementary Figure 7.16) [27, 167].

In summary, neurons in community 3 are involved in the control of eye movement and stabilize gaze. Additionally, the cerebellum contains various types of neurons that are separated into distinct subcommunities.

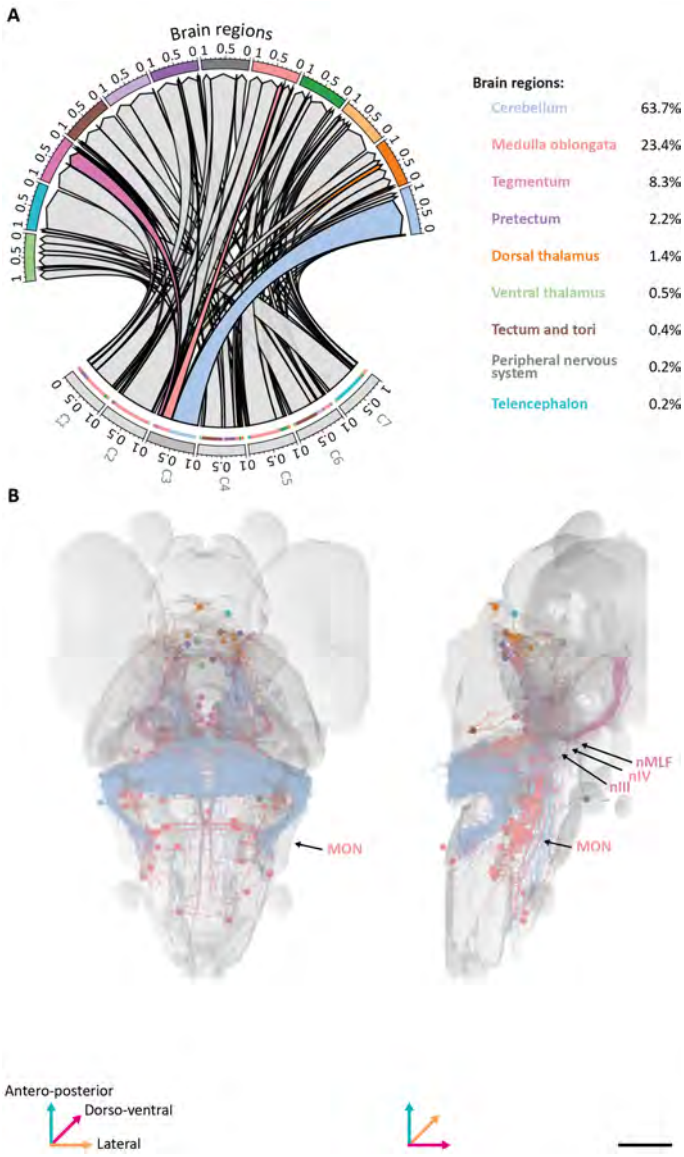

Figure 3.7: Community 3.
A) Neurons are distributed across multiple brain regions at different amounts. **B)** Projections of the neurons found in the community. Colors are assigned based on soma location. nIII: oculomotor nucleus, nIV: trochlear nucleus, nMLF: nucleus of the medial longitudinal fasciculus, MON: medial octavolateral nucleus. Scale bar = 100 μm

3.3.4 Community 4

It is mainly represented by neurons in the tectum with the tori, pretectum, medulla oblongata, retina, ventral and dorsal thalamus, and hypothalamus (Figure 3.8A).

The pattern of connections formed between neurons located in the retina and neurons located in an area comprising the pretectum, dorsal and ventral thalamus (Figure 3.8B, Supplementary Figure 7.17) is likely associated in the visual processing. These neurons project from the retina to retinorecipient regions, such as AF 4 and 5, which are known to be associated, respectively, with neurons located in the ventral/dorsal thalamus and pretectum [168, 169]. AF4 and 5 respond to dimming visual stimuli and

direction stimuli, respectively [170–172]. Furthermore, pretectum neurons that project to the cerebellum are part of direction-selective neurons, located near AF4, associated with motion-opponent responses (Figure 3.8B, Supplementary Figure 7.17) [141]. The connections formed between neurons in the retina and neurons located in the controlateral tectum (Figure 3.8B, Supplementary Figure 7.18) are associated with the processing of visual stimuli [173, 174]. The information processed in the tectum is then conveyed to the hindbrain premotor nuclei throughout the tectobulbar tract (Figure 3.8B, Supplementary Figure 7.20) [174].

In summary, neurons in community 4 are involved in the processing of various visual stimuli and the transformation into premotor commands.

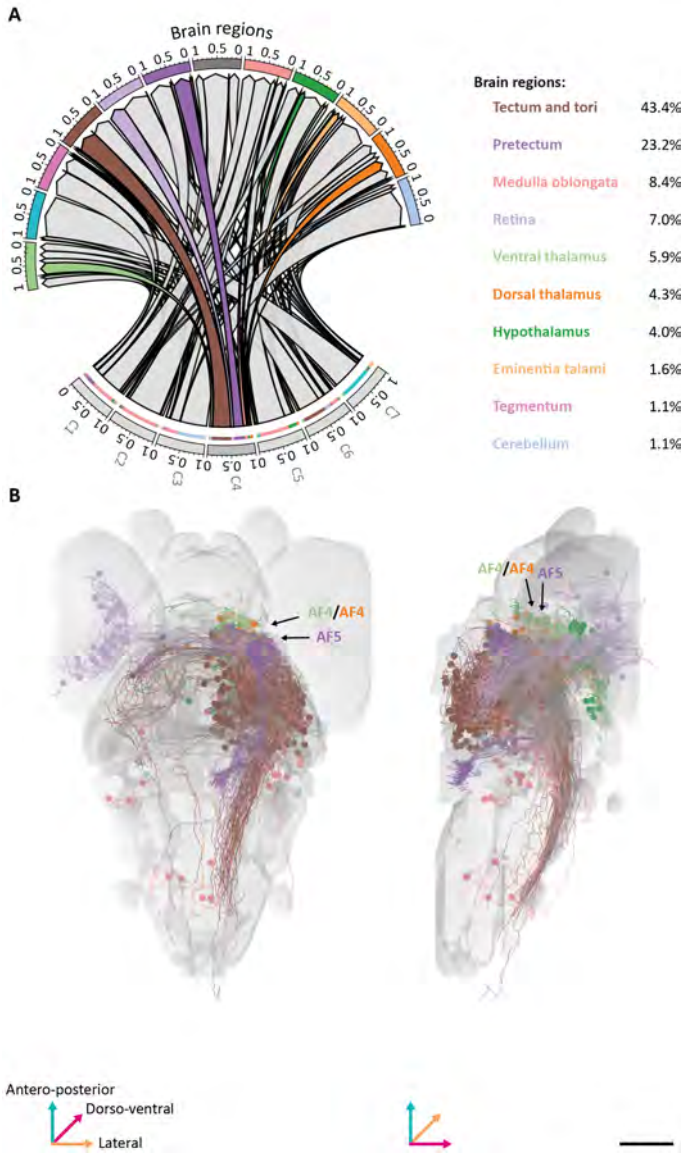

Figure 3.8: Community 4.
A) Neurons are distributed across multiple brain regions at different amounts. **B)** Projections of the neurons found in the community. Colors are assigned based on soma location.
AF4: arborization field 4, AF5: arborization field 5
Scale bar = 100 μm

3.3.5 Community 5

It is mainly represented by neurons in the medulla oblongata and hypothalamus (Figure 3.9A). Neurons in the medulla oblongata are highly segregated in the superior part of the region, comprising the raphe and the interpeduncular nucleus (iPN).

The connections formed between neurons located in the dorsal thalamus, precisely in the habenula (Hb), and neurons located in the iPN (Figure 3.9B, Supplementary Figure 7.26, Supplementary Figure 7.28) are associated with the habenulo-interpeduncular pathway involved in the tuning of adaptative behaviours by regulating monoaminergic nuclei [175–178]. The connections formed between neurons located in the iPN and the hypothalamus and telencephalon (Figure 3.9B, Supplementary Figure 7.25, Supplementary Figure 7.28) as well as those within the hypothalamus and telencephalon (Figure 3.9B, Supplementary Figure 7.27) are likely involved in modulating behavioral states [179, 180].

In summary, neurons in community 5 are involved in the limbic system.

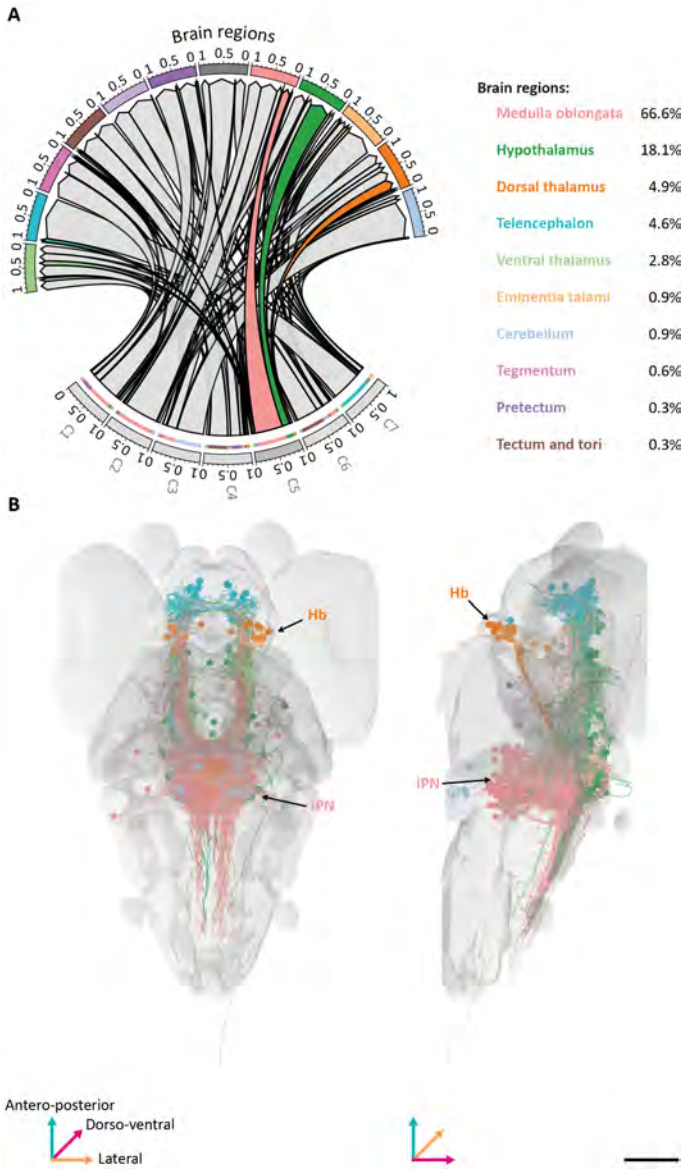

Figure 3.9: Community 5.
A) Neurons are distributed across multiple brain regions at different amounts. **B)** Projections of the neurons found in the community. Colors are assigned based on soma location. Hb: habenula, iPN: interpeduncular nucleus
Scale bar = 100 μm

3.3.6 Community 6

It is mainly represented by neurons in the tectum with the tori, medulla oblongata, the retina, the pretectum, and the ventral thalamus (Figure 3.10A). The community shows the connections on the opposite side of the brain from those depicted in community 4, with few variations. Specifically, it does not include pretectum neurons involved in motion-opponent responses (these neurons can be found in community 1, Supplementary Figure 7.6).

In summary, neurons in community 6 are involved in the processing of various visual stimuli and the transformation into premotor commands.

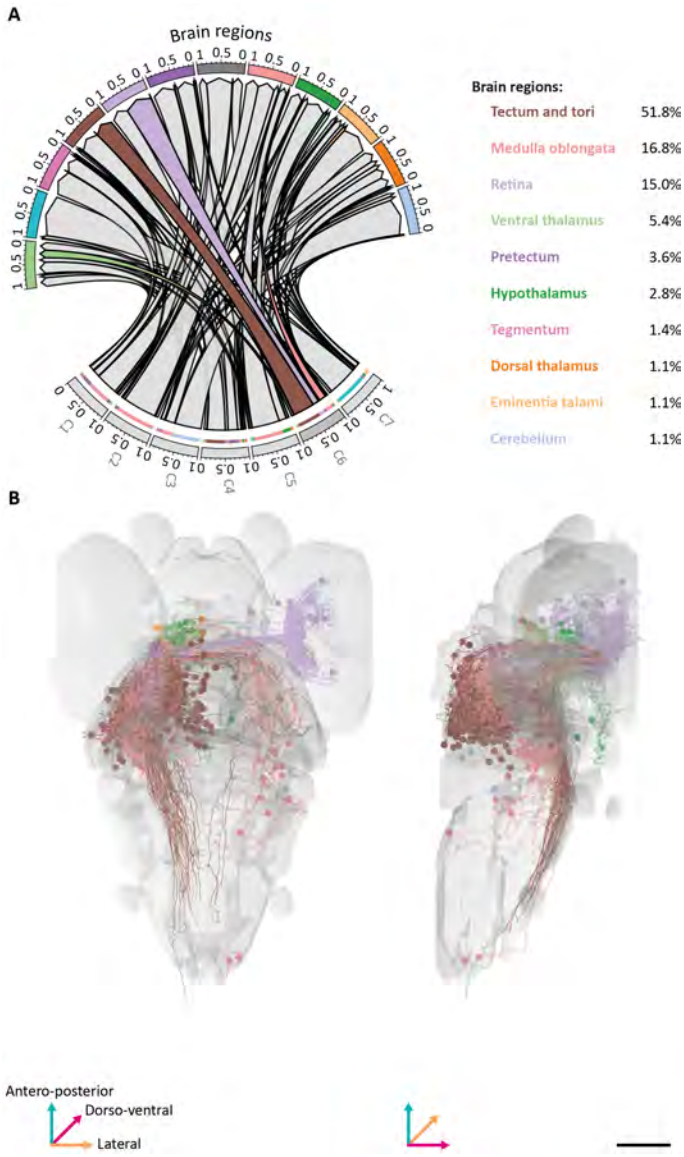

Figure 3.10: Community 6.
A) Neurons are distributed across multiple brain regions at different amounts. **B)** Projections of the neurons found in the community. Colors are assigned based on soma location.
Scale bar = 100 μm

3.3.7 Community 7

It is represented mainly by neurons in the telencephalon, eminentia talami, and perypheral nervous system (Figure 3.11A).

The olfactory epithelium (OE), located in the peripheral nervous system, sends olfactory information to neurons in the olfactory bulb (OB) through connections (Figure 3.11B, Supplementary Figure 7.39). Mitral cells then project the information to higher olfactory centers in the caudal brain, such as the habenula (Hb) and hypothalamus (Figure 3.11B, Supplementary Figure 7.35,Supplementary Figure 7.37) [27, 181]. In addition, pallial and subpallial neurons branch out in similar forebrain regions to mitral cells, which may suggest communication between these neurons (Figure

3.11B, Supplementary Figure 7.36, Supplementary Figure 7.38) [27].

In summary, neurons in community 7 are involved in the processing of olfactory stimuli.

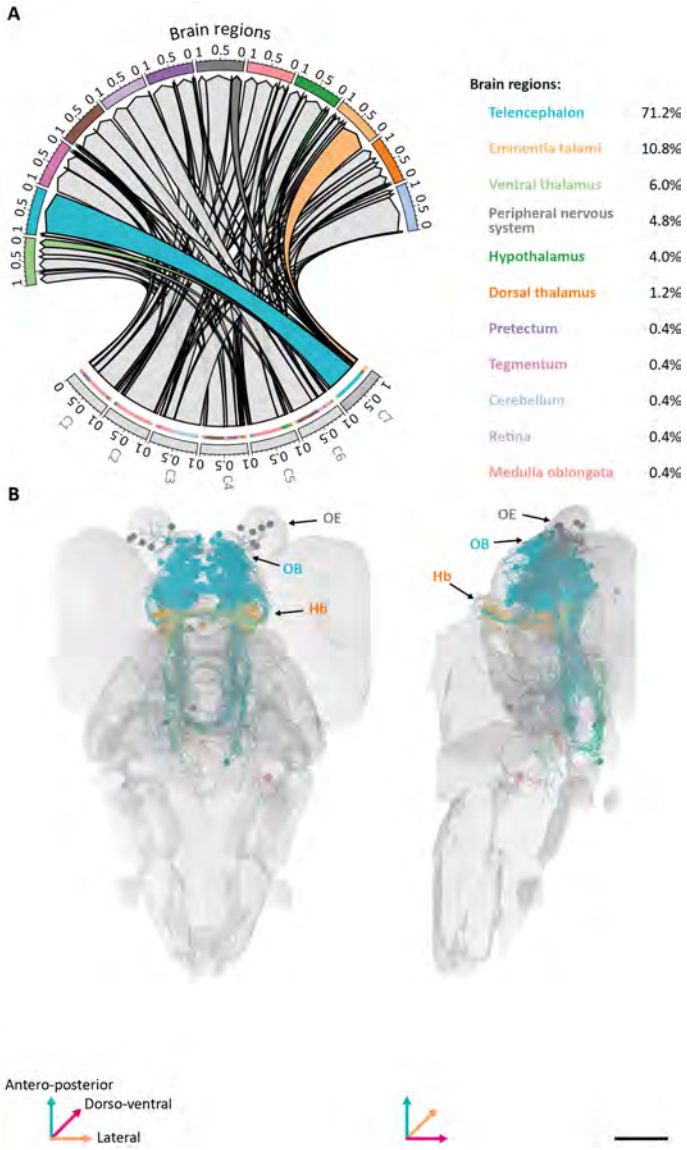

Figure 3.11: Community 7.
A) Neurons are distributed across multiple brain regions at different amounts. **B)** Projections of the neurons found in the community. Colors are assigned based on soma location.
Hb: habenula, OB: olfactory bulb, OE: olfactory epithelium.
Scale bar = 100 μm

3.4 Relationships between communities

The existence of principal networks supported by communities of neurons showing a relatively higher connection degree leaves open the question on how the different identified network could interconnect one another. In order to investigate this aspect, we evaluated the links formed across different communities (Figure

3.12). This analysis showed a rather heterogenous scenario, with some communities characterized by a relevant proportion of connections with a particular community (e.g. C7 - C5 in Figure 3.12), while in other cases it appears a more homogeneous pattern (e.g. C1 in Figure 3.12).

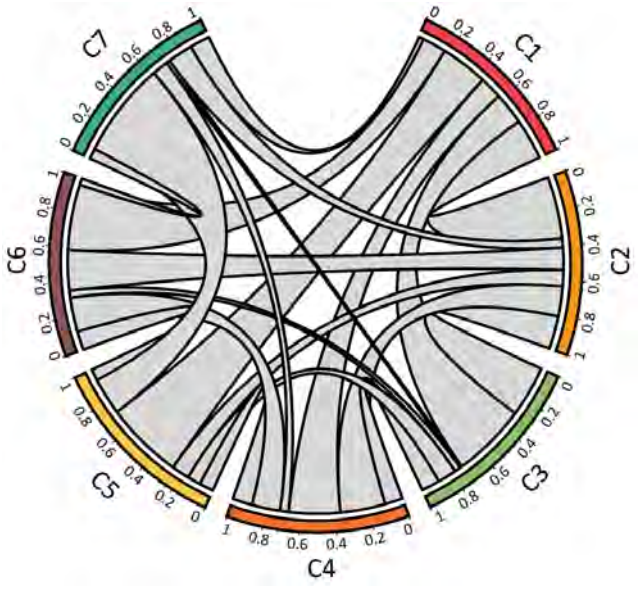

Figure 3.12: Relationships between communities.
Distribution of connections between the communities.

3.5 Conclusions

We used a network analysis algorithm for community detection to reveal the wiring diagrams of neuronal networks and their underlying organization. We tested this approach on a synthetic connectome generated from a database of more than 3,000 anatomical reconstructions of neuronal cells from the zebrafish larval brain. This led to the identification of 49 groups, comprising 7 main communities and 42 lower order sub-communities, of highly connected neurons spanning multiple brain regions. Importantly, for most of the identified modules, it was possible to identify, either based on anatomical reports or on functional characterizations, a functional role.

Results: Whole brain imaging at cellular resolution

4

The chapter is adapted from candidate first-author research paper [135].

4.1 Development of a configuration for 3D scanning multiphoton microscopy

To reconstruct neuronal dynamics at a cellular resolution across the whole brain of the zebrafish larva, we developed a raster scanning setup that incorporates an electrically tunable lens (ETL) onto a commercially available multiphoton microscope equipped with an 8 kHz resonant scanner (Figure 4.1A - blue components). We positioned the ETL upstream to the galvo mirrors, in a position that ensures the imaging beam to fit within the lens's optical window without overfilling it. The ETL works in continuous z-scanning mode, wherein the focal position moves linearly during the volume acquisition (ramping phase), followed by a rapid return to the initial position (reset phase). To achieve this, we synthesize a quasi-sawtooth waveform to control the ETL driving current (Figure 4.1B left - Magenta line) using a pre-calibrated look-up table (LUT) based on the volume scanning settings. As a consequence, the waveform show two phases: one where the input current to the ETL is steadily increasing according to the LUT (ramping phase) and the other (reset phase) where the input current is quickly brought back to the original level of 0 mA. The cycle repeats every 30 frames. The LUT links the driving current for the ETL and the effective focus position (Figure 4.2B). This allows for control of the excitation spot within the designated z-range (z_{min}, z_{max}) using an ETL-current value within the corresponding range (I_{min}, I_{max}) (Figure 4.1B center - Cyan line). In this type of optical configuration, maintaining tight synchronization between lateral (XY) and longitudinal (Z) scanning is crucial to prevent artifacts. To minimize the possibility of image acquisition drifts and jitters, we developed a simple electronic circuit using a microcontroller. Specifically, we employed the frame clock of the microscope control unit (Frame Sync, Methods 2.2.3) as the clock for a digital incremental counter

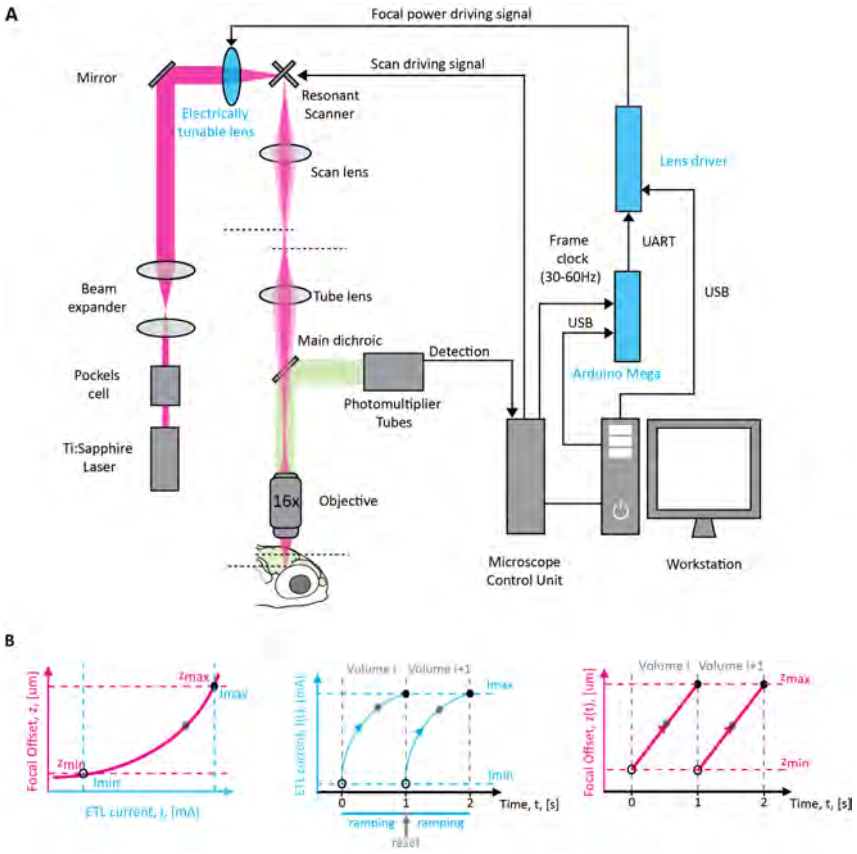

Figure 4.1: The layout of the optical configuration and the properties of the ETL.
A) Implementation of the electrically tunable lens along the optical path, the lens driver and the microcontroller (blue components). **B)** The ETL input current works in a quasi-sawtooth pattern. The pattern is composed of two phases. A ramping one, where the input current to the ETL is continuously increased according to the LUT; and a reset one, where the input current is reset to 0 mA. The cycle occurs every 30 frames. **C)** At the level of the sample, this pattern is translated in a continuous and linear change of the focus. Adapted from [135]

on the microcontroller board that controls the ETL driver. The microcontroller is programmed to start generating the current ramp, based on the measured LUT, every time the counter reaches a defined number of frames. Control of the ETL driving current is achieved by sending serial commands from the Arduino Mega to the ETL driver unit, which encode current values $I(t)$ corresponding to the expected time t and position z calculated from the LUT.

4.2 Optical properties of the 3D scanning configuration

When integrating components for remote control of focus, such as ETLs, modifications to the optical properties can occur, affecting the spatial resolution and field of view (FOV) size. To assess these effects, we evaluated the system's resolution by quantifying the lateral and axial extension of the Point Spread Function (PSF) - measured as the full width half maximum (FWHM) along the x-y and z directions, respectively. We acquired a series of z-stacks

of fluorescent polystyrene beads with a nominal diameter of 0.2 μm at eight different positions within the z-range of 0 to 233 μm, by mechanically moving the objective relative to the sample. We observed a progressive increase in the size of the PSF as the amount of defocus introduced by the ETL increased. At the center of the FOV, the $FWHM_{x,y}$ increased from 0.54 μm $\pm$ 0.08 μm to 1.25 μm $\pm$ 0.12 μm, while the $FWHM_z$ increased from 2.82 μm $\pm$ 0.30 μm to 17.28 μm $\pm$ 1.88 μm. The non-uniform diffraction efficiency of optical elements can cause degradation of optical performance which can vary depending on the radial distance from the center of the FOV. At 300 μm from the FOV origin, the PSF showed similar trends. However, the effective size of the imaged FOV changed by about 3% with respect to the area addressed with the ETL set at the middle of its z-range.

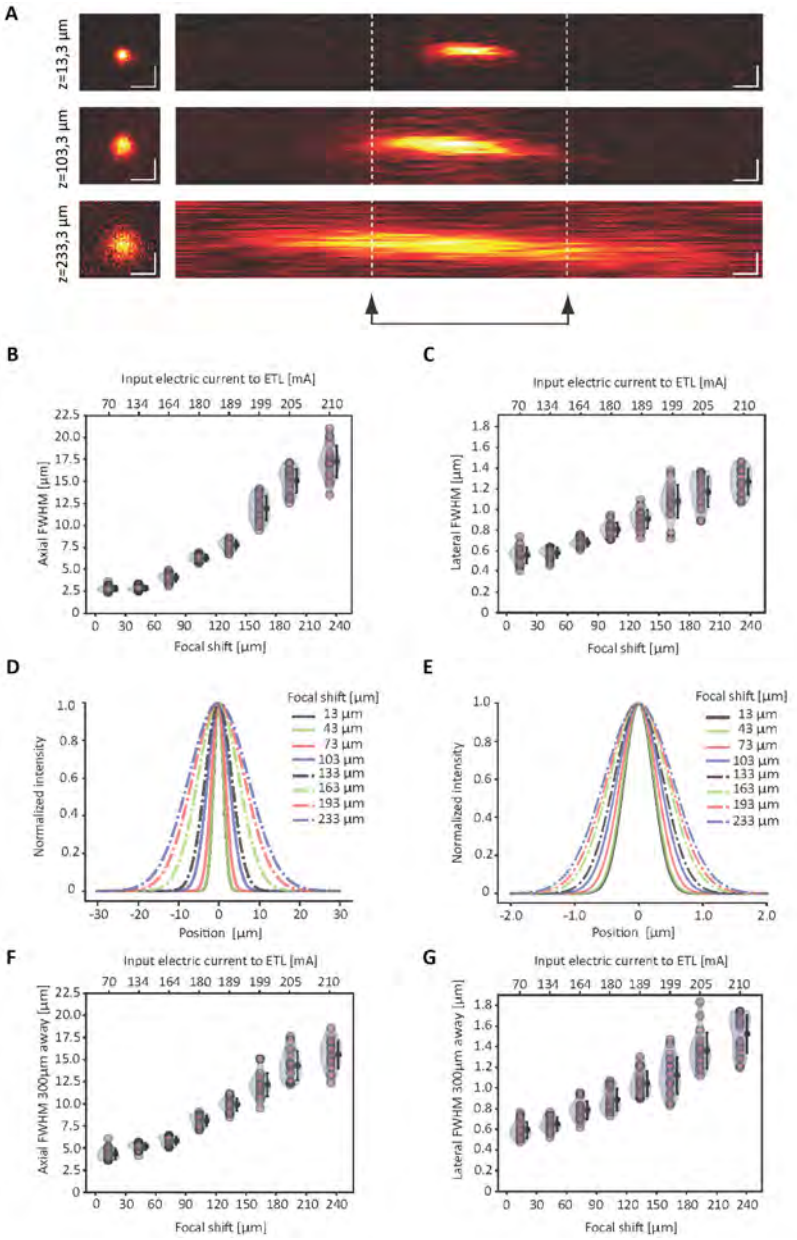

Figure 4.2: Optical performances of the system.
A) Average intensity projections (left with top-view XY, right with side view ZX) of the point spread function (PSF) measured at 920 nm on 0.2 μm fluorescent beads at three different settings of the ETL tuning range. Highlighted with dashed lines is the typical cell size (6 μm). Scale bar = 1 μm. **B,C)** Axial and lateral FWHM of the PSF as function of the ETL defocus and of the corresponding ETL driving current, for beads measured within 50 μm from the center of the FOV. **D,E)** Axial and lateral intensity profile of the PSF for beads measured within 50 μm from the center, corresponding to eight different settings of the ETL. **F,G)** Axial and lateral FWHM of the PSF as function of the ETL defocus and of the corresponding ETL driving current, for beads measured at 300 μm from the center of the FOV.
Adapted from [135]

4.3 Whole brain neuronal recordings

To densely record neuronal activity throughout the brain, we configured the acquisition parameters to sample a volume corresponding to approximately 800 × 400 x 180 μm3 (W × L × H), including almost completely the zebrafish brain. Taking into account the typical average cell diameter of 6 μm, such a volume can be conveniently sampled in 30 planes of 1024 x 512 pixels, corresponding to 1 volume per second (vps) (Figure 4.3), or 512 x 256 pixels, corresponding to 2 vps. Because the sawtooth control signal driving the ETL causes each plane to tilt slightly in the shorter direction of the frame (axis Y), the last pixels row averages 6 μm lower than the first pixels row of the same frame. In the typical 1 vps acquisition scenario, the average spatial sampling is 57.2 pixels per cell, with an integration time of 3.2 μm. To optimize spatial sampling and facilitate automatic segmentation of cells, it is common to use zebrafish larvae that express the nuclear localized activity reporter GCaMP6s, e.g. line *Elavl:H2B-GCaMP6s*. This version of the fluorescence reporter presents a characteristic response decay time between 3.5 and 4.1 s. Therefore, sampling cell activity at 1 vps still allows a good reconstruction of the neuronal activity profiles.

We applied our configuration to map the brain activity on non-anesthetized 5 dpf gel-embedded zebrafish larvae presented with monocular visual stimulation (Figure 4.4). We recorded 5 minutes of spontaneous activity followed by 30 minutes of sensory-evoked activity. The stimulation protocol consisted of a series of looming dots presented every 150 s on a screen placed at the side of the fish. The recorded planes (Figure 4.4A-C, left panels) were processed using a computational pipeline for semi-automatic segmentation and identification of the activity of individual neurons, resulting in maps of brain dynamics at high resolution (Figure 4.4A-C, right panels). This procedure was based mainly on the open platform 'suite2p' and relied on an automatic cell classifier trained with datasets obtained using *Elavl:H2B-GCaMP6s* larvae. Briefly, following a plane-by-plane motion correction, de-interleaved data corresponding to individual planes were filtered with a short-window running average kernel and then processed for the automatic cell segmentation routine to identify region of interest (ROI) corresponding to the individual neurons. This routine, depending on

the acquisition Signal to Noise Ratio (SNR), typically led to the automatic identification of 30,000–50,000 putative cells (Figure 4.5A, the grey trace at the bottom indicates the stimulation).

To identify neurons with the most prominent responses to visual stimulation, we used a generalized linear regression model to fit the activity profile of each segmented neuron with a regressor, corresponding to the presentation of the visual stimulus (Methods 2.3.2). For each neuron, we computed a score defined as the regression coefficient divided by the mean squared error. We considered a neuron to respond to stimulation if it presents a score within the top 5% of the complete distribution of the scores, in all identified cells and trials. From the complete activity dataset, we were able to extract a subset of 2400 neurons whose activity profile increased in response to the presentation of the stimuli (Figure 4.5A). The application of a hierarchical clustering analysis revealed the presence of four main groups (black, orange, blue and bluish green sub-trees), with distinct profiles of response to repeated visual stimulation (Figure 4.5B).

The functionally identified clusters were mapped on the corresponding zebrafish larvae brain (Figure 4.6). Stimulus-responsive cells were located, as expected, in the optic tectum contralateral to the stimulated eye, in regions in proximity of some of the deeper arborization fields, in the pretectum, in the nuclei isthmi, and in few regions of the hindbrain (Figure 4.6B, C). These maps revealed that, even though the clusters show a certain degree of overlap, some regions do present a pronounced enrichment for one of the clusters identified. This is particularly true for cluster 4 which is highly represented in the optic tectum and in areas located close to the deeper arborization fields of the contralateral side of the brain. Cluster 2 mainly populates the midbrain region corresponding to the optic tectum. Cluster 1 is mainly located at the level of the tectum opticum and in the ipsilateral hindbrain regions. Finally, cells belonging to cluster 3 are mainly located ventrally in areas of the pretectum and thalamus.

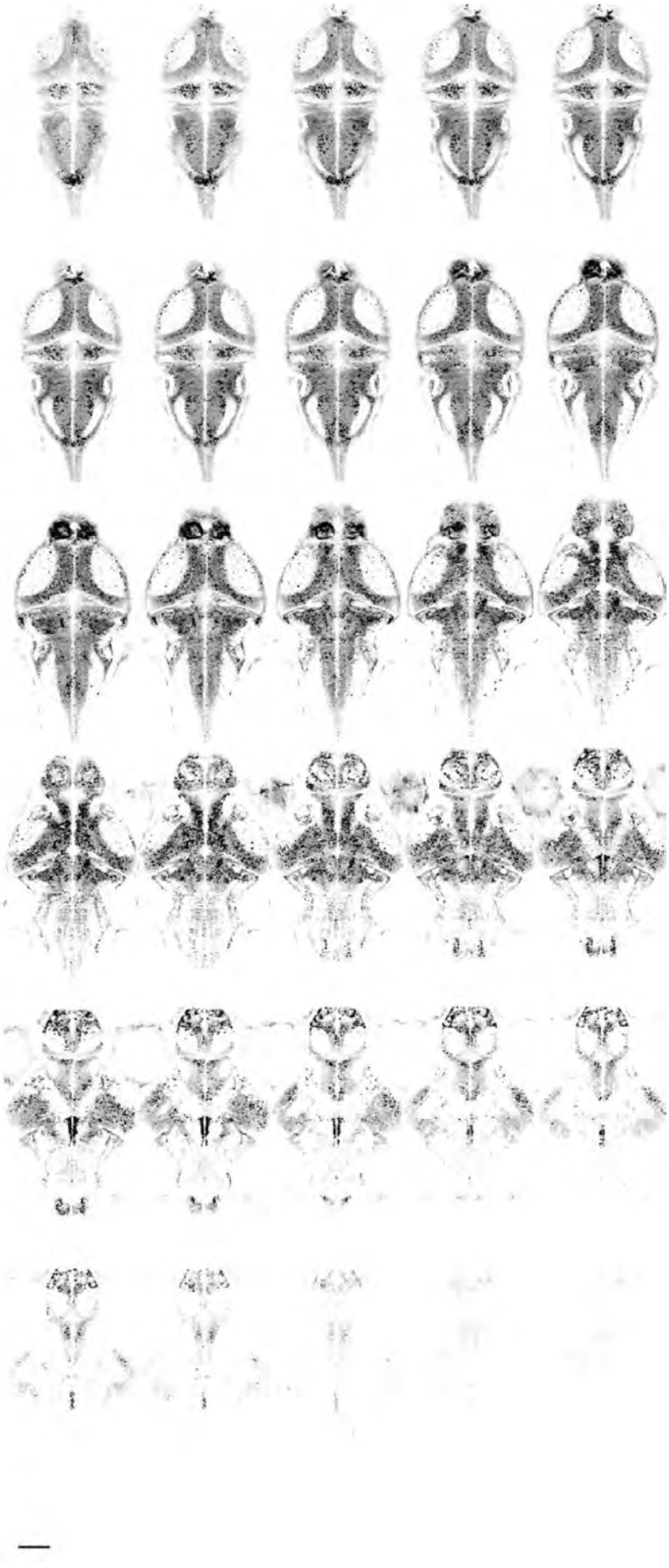

Figure 4.3: Multiplane imaging of the zebrafish brain.
Average intensity projections of 30 planes, encompassing almost the entire volume of the zebrafish larvae, sampled during an acquisition. Scale bar = 100 μm.
Adapted from [135]

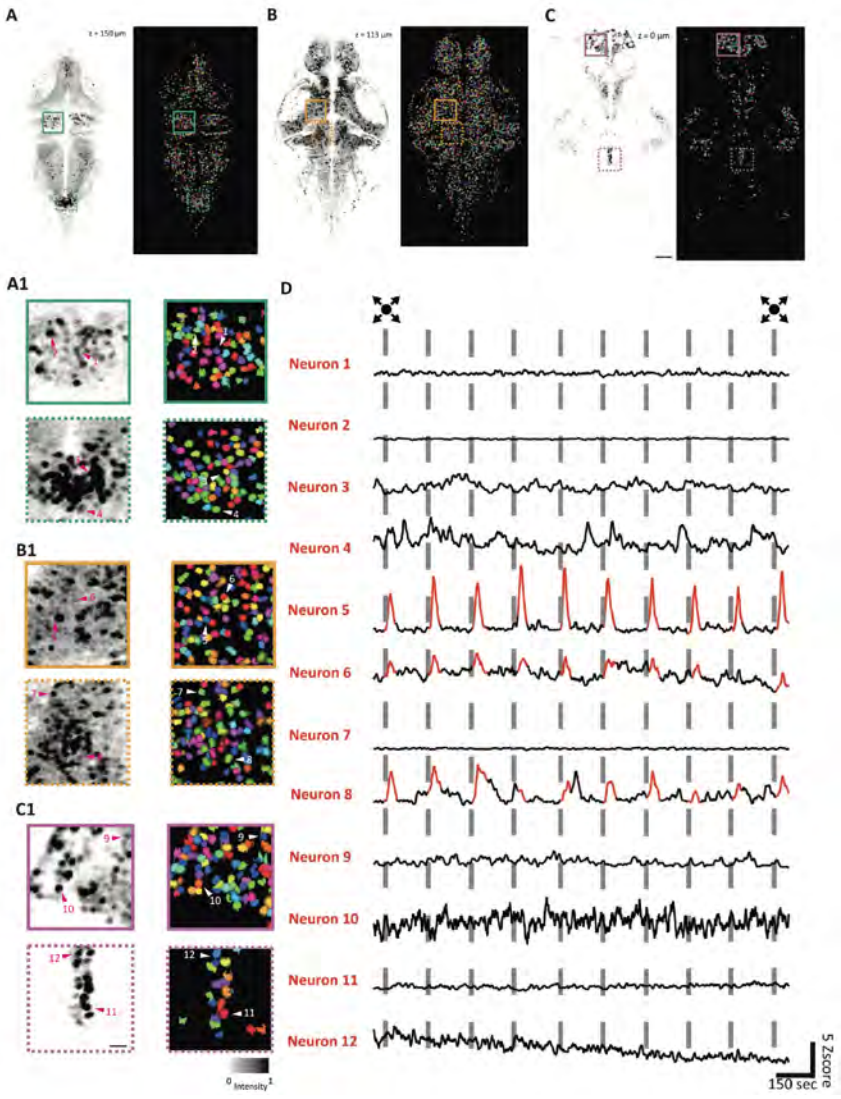

Figure 4.4: Whole brain calcium imaging - segmentation.
A–C) Average intensity projections (left) and the results of the cell segmentation process (right) for a dorsal (A), central (B) and ventral (C) planes of the fish corresponding to the z-levels at +150 μm, +113 μm and +0 μm, respectively. The colored boxes indicate the areas of the inset (A1–C1). Scale bar = 50 μm. **A1–C1)** Representative fields of view of the average intensity projections (left) and of the segmentation (right) extracted from (A–C). Arrows indicate corresponding cell bodies. Scale bar = 10 μm. **D)** The activity profiles expressed as z-score for the neurons highlighted in (A1–C1).
Adapted from [135]

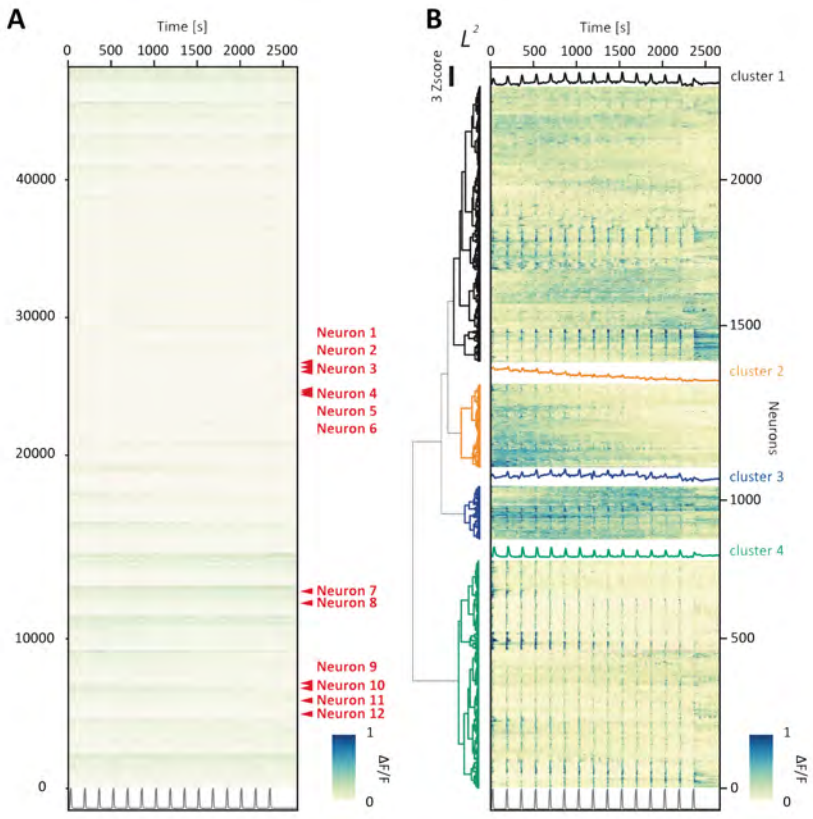

Figure 4.5: Whole brain calcium imaging - neural activity.
A) Raster plot showing the activity profiles of the complete dataset of 47,992 neurons segmented as function of time. The neurons corresponding to the Figure 4.4A1-C1 insets are indicated in red. The grey trace at the bottom indicates the stimulation. The vertical bars indicate the presentation of the looming stimulation. **B)** Hierarchical clustering and raster heatmap of the 2400 stimulus-responding neurons identified with the regression analysis. For each cluster the average response is overlaid in the corresponding color. The grey trace at the bottom indicates the stimulation. Adapted from [135]

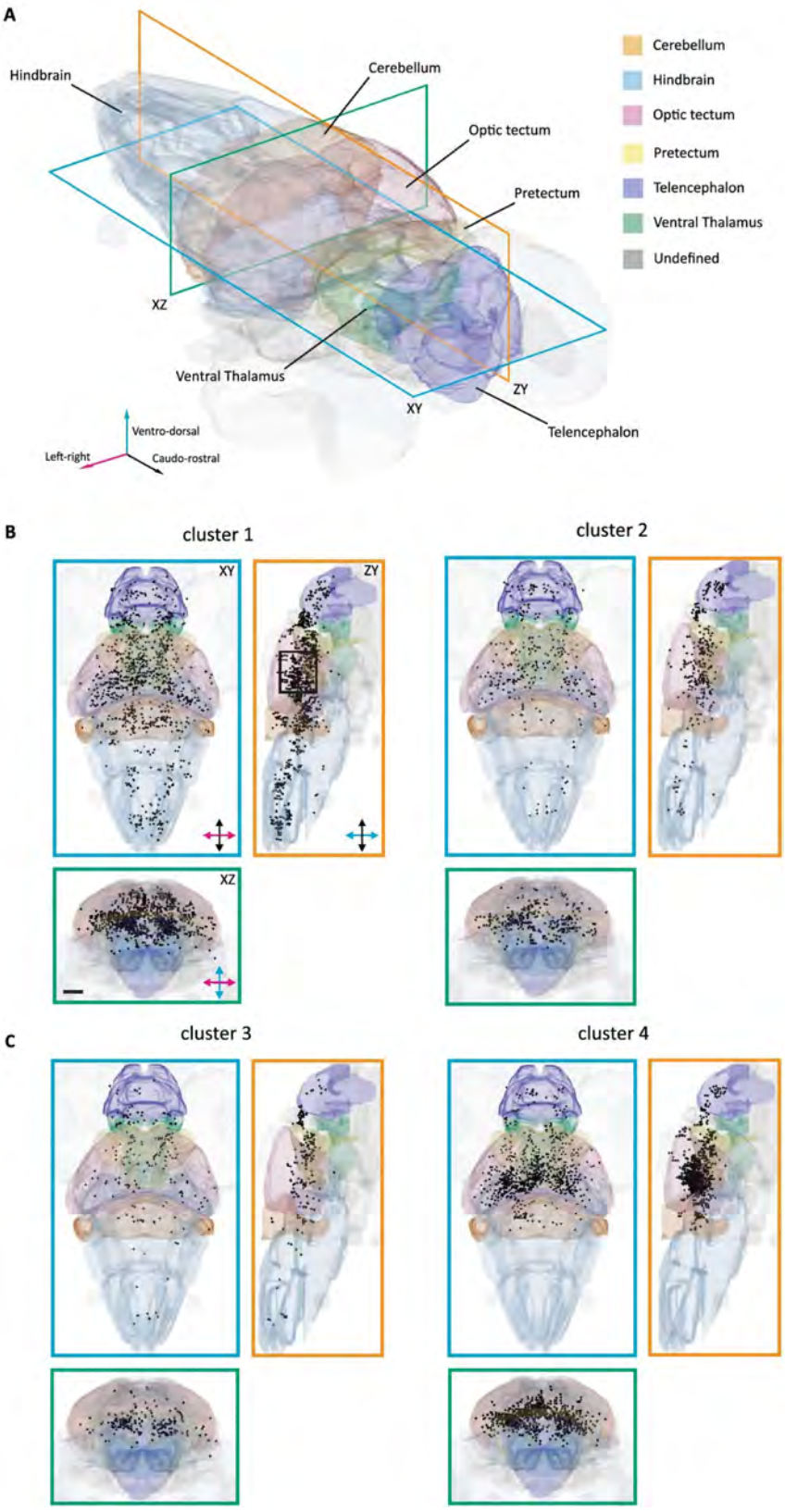

Figure 4.6: Anatomical representation of the identified clusters of visually responsive cells.
A) Three-dimensional representation of the brain of the larva with some of the most prominent region indicated. Three sectioning planes are overlaid to indicate the corresponding viewports for the following orthoviews. **B)** Horizontal (cerulean), sagittal (orange) and coronal (bluish-green) views of the brain, with the projection of the stimulus-responsive cells belonging to the cluster 1. Scale bar = 100 μm. **C)** Horizontal, sagittal and coronal views of the brain, with the projection of the stimulus-responsive cells belonging to the cluster 2, 3 and 4. Scale bar = 50 μm.
Adapted from [135]

4.4 Conclusions

We developed an alternative design for fast volumetric cell-resolution brain imaging in zebrafish larvae by integrating an ETL in a multi-photon microscope. This approach was used to study whole brain dynamics during sensory stimulation, and with a refined analysis pipeline, we obtained a large datasets containing 47992 neurons. From this dataset, we identified 2,400 stimulus-responding neurons and using a hierarchical clustering approach, we were able to identify functionally defined clusters. By mapping these groups to the reference brain atlas, we found a heterogeneous scenario with clusters distributed across multiple anatomical regions, with a significant presence in the optic tectum.

Results: Analysis of Galn$^+$- and Crh$^+$-neurons

5

Stress is an internal state strongly influencing animal behavior. In zebrafish, the hypothalamus plays a central role in controlling responses to stress via the hypothalamic-pituitary-interrenal (HPI) axis, homologous of the mammalian hypothalamic-pituitary-adrenal (HPA) axis. Galn$^+$-neurons are crucial for regulating behavioral responses by reducing the stress induction. However, it is not clear how Galn$^+$-neurons affect the neurons responsible for producing corticotropin-releasing hormone (*Crh*), which are the main activators of the HPI axis. Although transgenic lines have been produced to label Galn$^+$-neurons, identification of Crh$^+$-neurons in zebrafish is still performed through post-mortem labeling, thus limiting the investigation from a functional point of view.

In the chapter, we overcome this limitation by bridging information between live functional recording and post-mortem immunostaining in zebrafish larvae. In the first section, we describe the application of an anatomical registration pipeline based on Methods 2.4.1 to bring into the same anatomical space the neuronal activity of a live fish and its post-mortem immunostaining of Crh$^+$-neurons. In the second section, we characterize the activities of the identified neurons. The chapter is adapted from [155].

5.1 Identification of Crh$^+$-neurons in the zebrafish preoptic area

We implemented an anatomical registration pipeline based on Methods 2.4.1 to link Crh$^+$-neurons, identified by fluorescence in situ hybridization chain reaction (HCR), with functionally recorded neurons from the same fish (Figure 5.1). The method is similar to the MultiMAP approach [182].

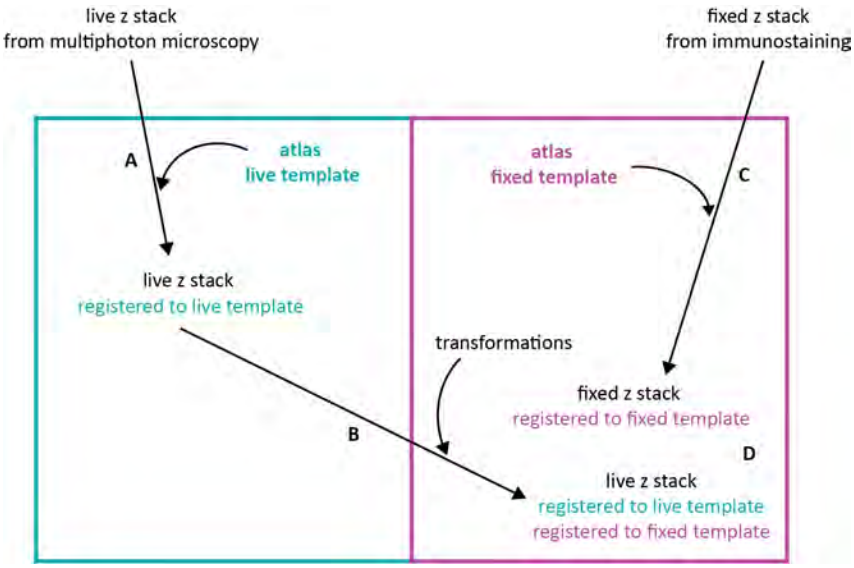

Figure 5.1: Workflow to bring recordings in the same anatomical space.
A) The live z-stack is registered with the reference live template. **B)** The registration output undergoes an additional registration based on the fixed template with a series of refined transformations previously established in [27]. **C)** The fixed z-stack is registered with the reference fixed template. **D)** At the end of the pipeline, the live z-stack obtained from multiphoton microscopy and the fixed z-stack obtained from immunostaining are in the same anatomical space.

First, we monitored the activity of neurons located in the PoA, a hypothalamic structure, before and after exposure to an osmotic stressor (100 mM NaCl). We employed a multiphoton system (Methods 2.2.2) equipped with an ETL for multiplane imaging (Methods 2.2.3). The recordings were made in 5 dpf *galn:Gal4; UAS:NTR-mCherry; elavl3:H2BGCaMP6s* larvae, where we sampled a volume (400 x 200 x 180 μm^3) encompassing the PoA at 30 planes per second, with 1024 x 512 pixels per plane and a relative z-spacing of approximately 6 μm. After functional recordings, high-resolution z-stacks of the entire brain were acquired (Figure 5.2A). Galn$^+$-cells were identifiable during live imaging by expression of NTR-mCherry. Crh$^+$-neurons were identified postmortem. The larvae were anesthetized with tricaine and fixed with 4% PFA in PBS overnight at 4°C. Following fixation, the subjects were sent to the Max Delbruck Center in Berlin where the fluorescence in situ HCR v.3.0 method was employed to detect *crhb* mRNA. The stacks obtained resulted in three types of signals, the pan-neuronal *GCaMP from elavl3:H2BGCaMP6s* (Figure 5.2B), the *Galn*$^+$ from

galn:Gal4; UAS:NTR-mCherry (Figure 5.2 left - red) and the *crhb* mRNA from in situ HCR v.3.0 (Figure 5.2C - right).

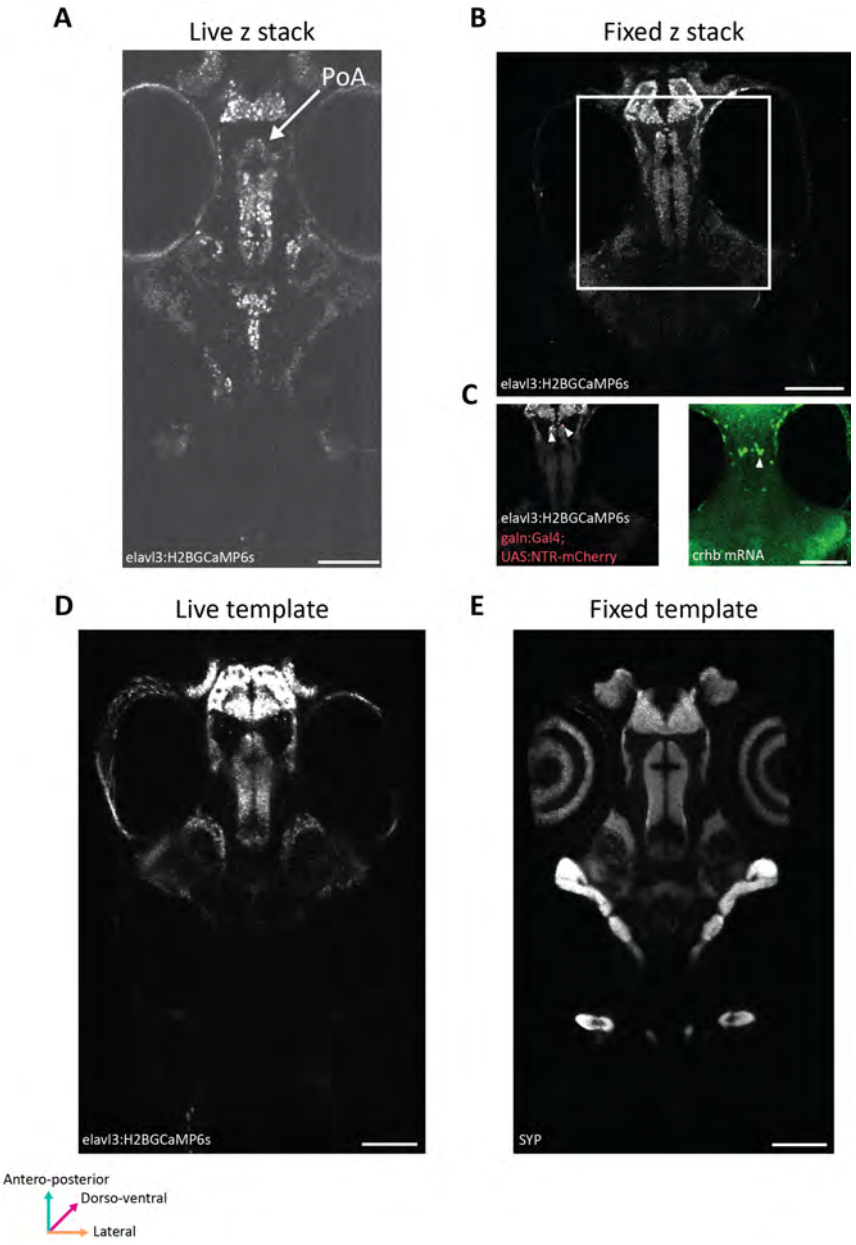

Figure 5.2: Representative planes of the acquired z-stacks and reference templates.
A) Representative longitudinal plane of a z-stack acquired at the multiphoton microscope. The live fish express pan-neuronal GCaMP (white). PoA: Preoptic Area. **B)** Representative longitudinal plane of a z-stack, from the same fish, acquired after fixation and in situ HCR. White box refers to C. The fixed fish express *elavl3:H2BGCaMP6s* (white). **C)** Detail of the region highlighted by the white box in B. Left: The fixed fish express *elavl3:H2BGCaMP6s* (white) and *galn:Gal4; UAS:NTR-mCherry*. Arrowheads indicate positive neurons. Right: The fixed fish is labelled for *crhb* mRNA (green). Arrowheads indicate positive neurons. **D)** Representative longitudinal plane of the reference' live template. White: GCaMP. **E)** Representative longitudinal plane of the reference' fixed template. White: SYP.
Scale bar= 100μm.

We registered the GCaMP channel of the z-stack acquired from each live fish to the same channel of the live template from the reference brain (Figure 5.3A) and applied the transformation already refined in [27] to obtain the anatomical space corresponding to the GCaMP channel of the fixed reference brain available in the reference (Figure 5.3B).

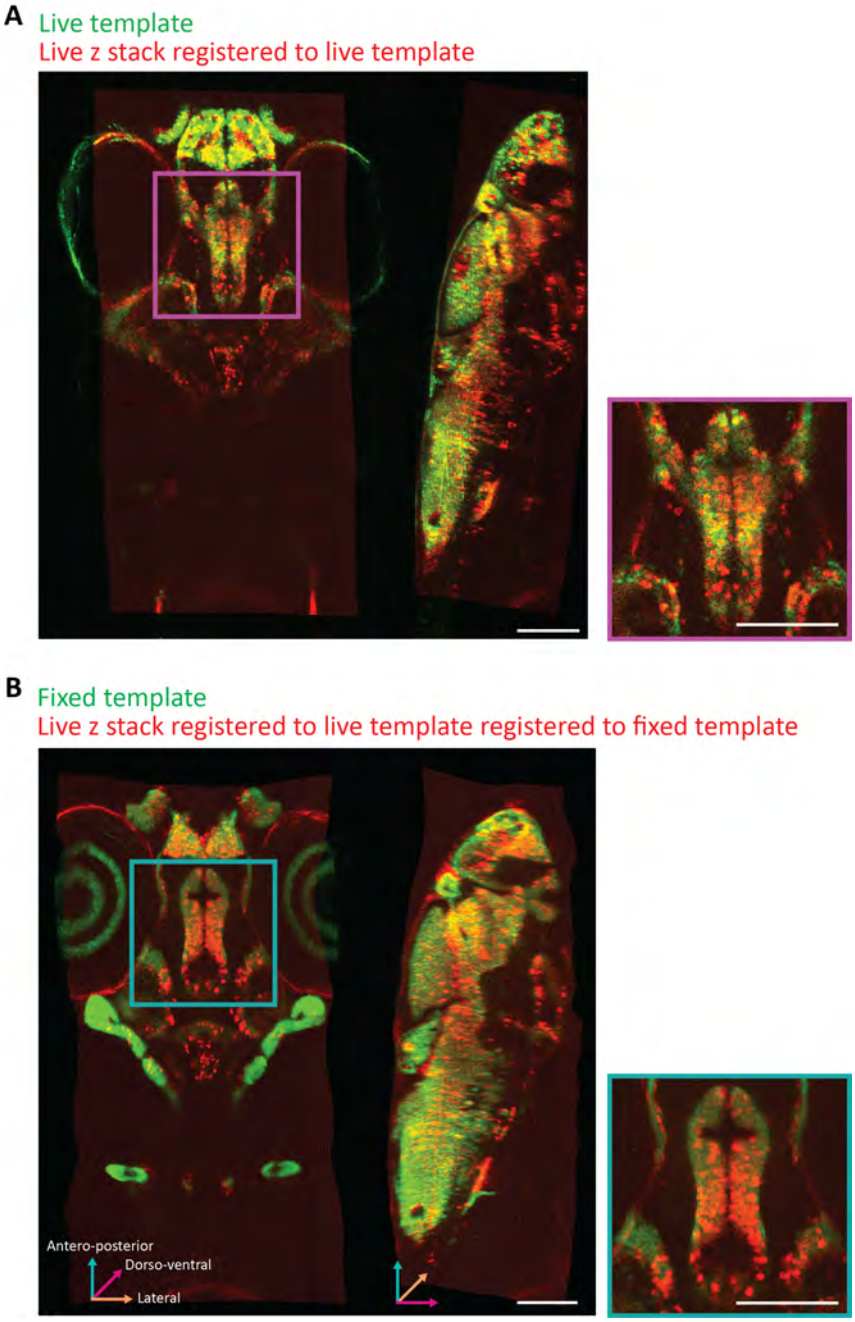

Figure 5.3: Registrations of the live z-stack.
A) The live z-stack registered to the reference live template (red) superimposed on the reference live template (green). **B)** The live z-stack registered to the reference live template an then to the reference fixed template (red) superimposed on the reference fixed template (green).
Scale bar= 100μm.

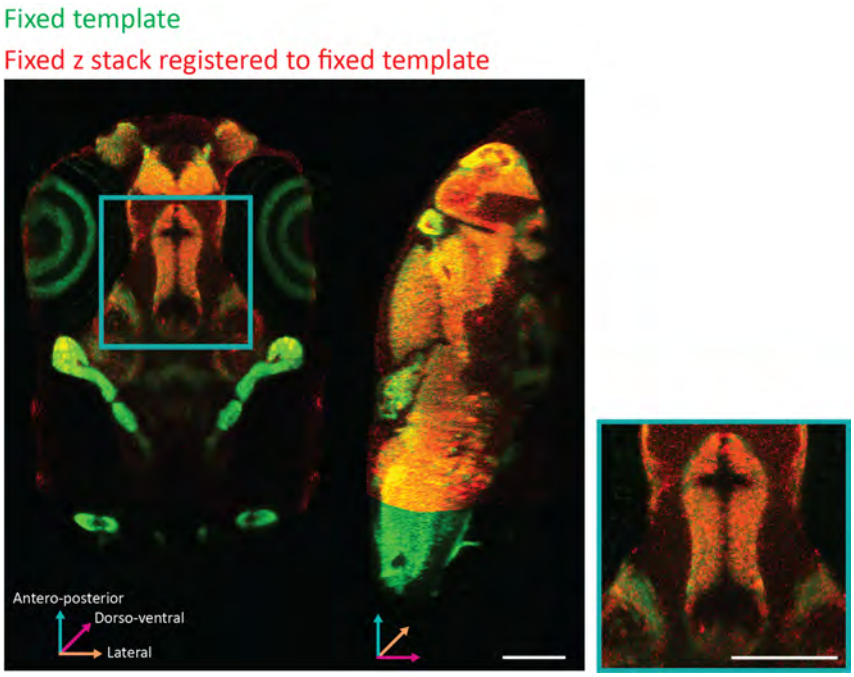

Figure 5.4: Registration of the fixed z-stack.
The fixed z-stack registered to the reference fixed template (red) superimposed on the reference fixed template (green).
Scale bar= 100μm.

We registered the GCaMP channel of the z-stack acquired from each fixed fish to the same channel of the fixed template of the reference brain (Figure 5.4). After the various registration processes are completed, both the live z-stack and the fixed z-stack are within the same anatomical space, allowing for direct comparison (Figure 5.5).

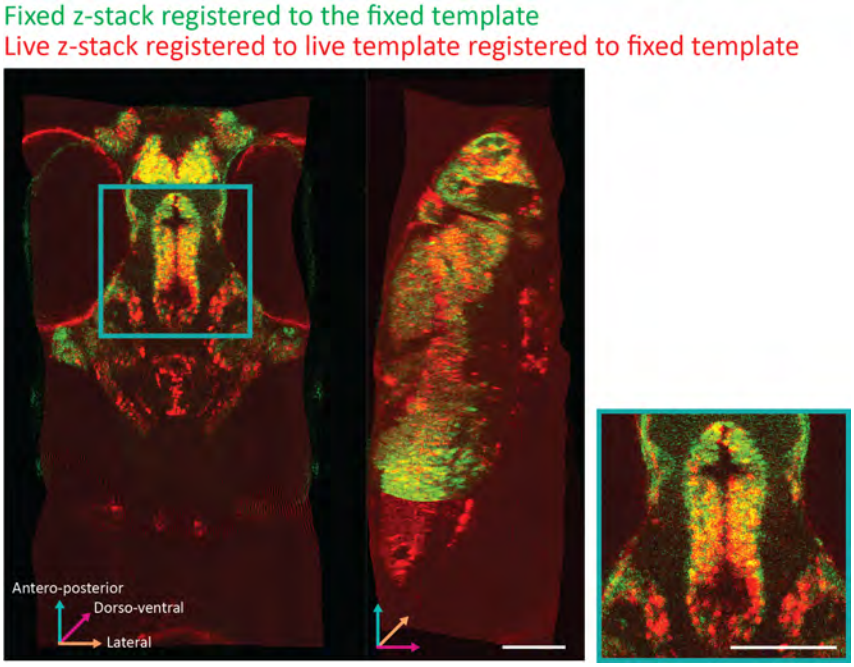

Figure 5.5: Registration of the fixed z-stack.
The fixed z-stack registered to the reference fixed template (red) superimposed on the reference fixed template (green).
Scale bar= 100μm.

The recorded neurons were segmented as described in Methods

2.3.1 and the x, y, z coordinates of the identified GCaMP expressing neurons underwent the same workflow as the live z-stack (Figure 5.1A,B). The neurons in the fixed z-stack were segmented as described in Methods 1.1 and the x, y, z coordinates of the identified Chr$^+$ neurons undergo the same workflow as the fixed z-stack (Figure 5.1C). After these steps, the spatial coordinates of GCaMP-expressing neurons and Chr$^+$ neurons are registered in the same anatomical space (Figure 5.1D). Neuronal activity obtained by GCaMP-expressing neurons is assigned to Chr$^+$ neurons whether colocalization between the two different spatial coordinates occurs.

5.2 Characterization of Galn$^+$- and Crh$^+$-neurons responses

We observed the presence of several types of stressor-induced responses in both Galn$^+$- and Crh$^+$-neurons. We identified distinct populations of neurons displaying either an increase of activity or a decrease of activity. However, a population did not respond to the stressor (Figure 5.6). These results are in line with previously reported findings [183].

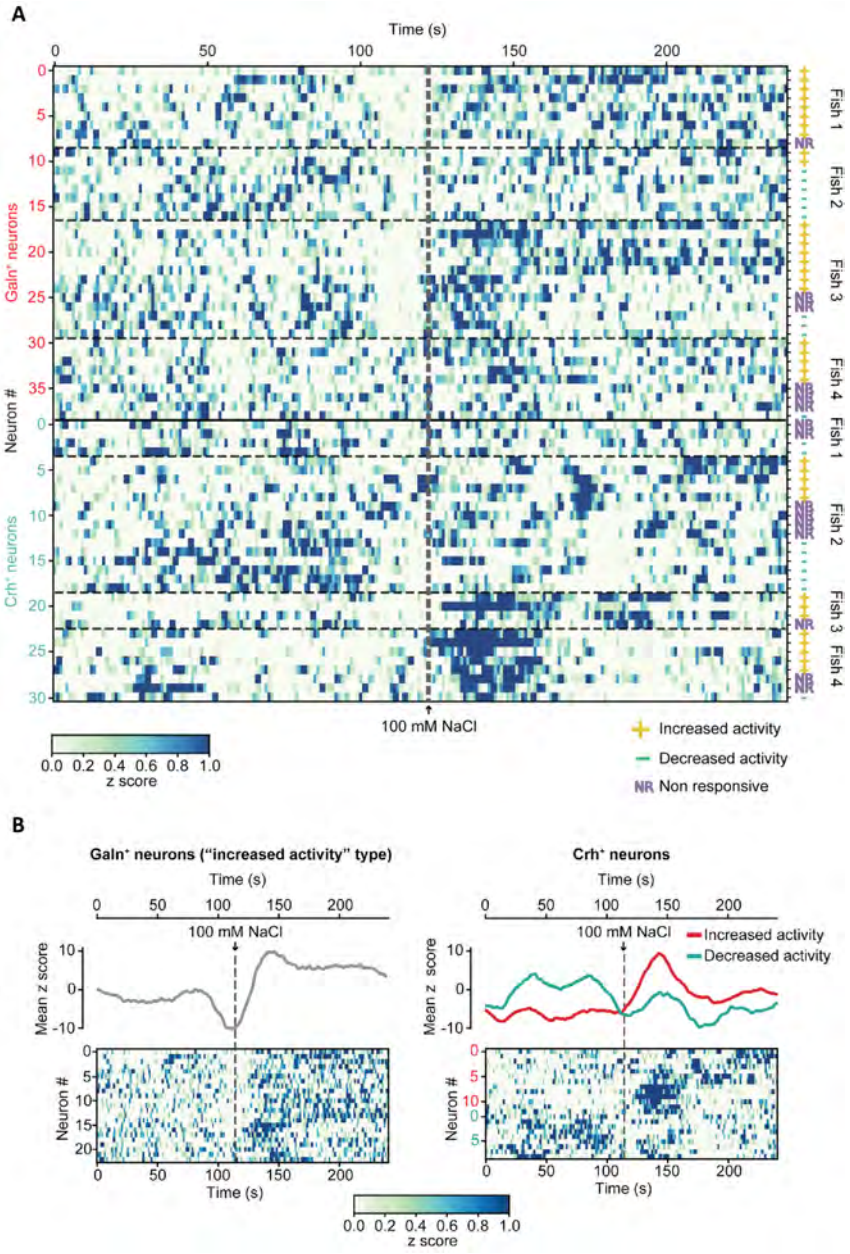

Figure 5.6: Activity of Galn⁺- and Crh⁺-neurons.
A) Activity of Galn⁺- and Crh⁺-neurons in the PoA of four 5 dpf *galn:Gal4; UAS:NTR-mCherry; elavl3:H2B-GCaMP6s* larvae before and after exposure to 100 mM NaCl. Responses are classified as "increased activity"(+), "decreased activity" (-), and non responsive (NR). **B)** (Top) Mean activity (Z score) of "increased activity" type Galn⁺-neurons (left) or Crh⁺-neurons (right) in the PoA of four 5 dpf *galn:Gal4; UAS:NTR-mCherry; elavl3:H2B-GCaMP6s* larvae, before and after exposure to 100 mM NaCl (dashed lines). Crh⁺-neurons were subdivided in "increased activity" or "decreased activity" types. (Bottom) Activity of individual Galn⁺- and Crh⁺-neuron. Red: Crh⁺-neurons of the "increased activity" type, teal: Crh⁺-neurons of the "decreased activity" type.
Adapted from [155].

5.2.1 Conclusions

We used a pipeline comprising a series of anatomical registrations to bring into the same anatomical space Crh$^+$-neurons identified with fluorescence in situ HCR and functional activity acquired from the same fish expressing GCaMP. This allowed us to assign with good confidence peculiar activity profiles to a population of Crh$^+$-neurons that are identifiable only by means of postmortem HCR and are not labelled in any transgenic line currently available. This confirms the efficacy of our approach linking anatomical (HCR in this case) with functional information (GCaMP signals).

6 Discussion

To obtain a more comprehensive understanding of the brain, it is important to examine both its activity and anatomical organization. Although advances in technology have allowed reconstruction of the synapses of almost all neurons, the relationship between structural connectivity and function is not yet fully understood.

Analysis of the zebrafish larva brain wiring diagram The advancement of increasingly powerful techniques has allowed for the creation of detailed and comprehensive reconstructions of neuronal anatomy throughout the entire brain, with a level of resolution that can depict individual synapses. However, these reconstructions have yet to reveal the overall connections and functional organization of neuronal circuits across the brain. Typically, these datasets are analyzed starting from a specific neuron and building upon its connections to reveal the organization of a single circuit of interest. Despite having knowledge of the synaptic input/output relationship for all neurons, there are currently no established methods for identifying highly connected neuronal communities and their connectivity patterns. Using a recently published dataset of anatomically reconstructed neurons and a proximity range, we generate the first complete brain cell resolution connectome of zebrafish larvae. The application of a community detection algorithm led to the discovery of independent groups of highly connected morphological neurons. The vast majority of reconstructed neurons belong to seven groups that span multiple brain regions and recapitulate known functional networks of behavioral relevance. This is in line with a similar approach, published after conceptualizing the work presented here, used on a EM-connectome of the zebrafish brain stem in which authors identify two communities with functional relevance [134]. The iteration of the algorithm within each community led to the identification of finer structural patterns. This approach of multi-level analysis of the communities considers the parent community an isolated identity. This of course represents an approximation that however we found useful for better describing the community structure in terms of sub-components.

Three principles have emerged from our analysis. First, the pattern of the communities is heterogeneous, with some more clustered and segregated than others. We found that the connectivity pattern of the telencephalon is highly segregated within the region, suggesting a localize information processing. This is consistent with its known function as a region that receives multiplexed input from mitral cells in the olfactory glomeruli and processes olfactory information before sending it to higher regions of the brain [181, 184–186]. The spontaneous activity of the telencephalon is also highly segregated from the rest of the zebrafish brain, further supporting the idea that it promotes segregated information processing [123]. Second, functional networks of behavioral significance are characterized by strong connectivity patterns. The intrinsic structure of the brain's spontaneous activity can significantly influence how it functions during stimulus-evoked conditions, as seen in both its connectivity patterns and modular structure [123]. Research has shown that the resting-state network of the brain has a stable modular core, surrounded by a flexible periphery of nodes that reconfigure their connections in response to stimuli [123]. One example of a stimulus is the looming dot, which is commonly perceived as threatening. Its presentation elicits widespread, bilaterally symmetric activity in various brain regions. The activity of looming selective neurons can be clustered in different neuronal population, including populations of direction-selective cells in the optic tectum and anterior hindbrain, as well as bilaterally responsive cells in the diencephalon and medial hindbrain [187]. The optic tectum, which is homologous to the superior colliculus in mammals, has been identified as a central hub for visuomotor transformations [174]. From here, neurons project to the pretectal area and the tectobulbar tract, which is involved in the transformation of these signals into motor commands. Our approach was able to identify circuit wiring diagrams that resemble these connections. Additionally, the directed and undirected network exhibit conserved patterns of connectivity, implying that the primary mode of connection is through axon-dendritic projections. This finding is consistent with the results observed in the Drosophila larva connectome [58]. Third, different types of neurons have different connectivity patterns. By iterating the community detection algorithm on the cerebellum module (community 3), we were able to identify fine differences between neuron types and to distinguish Purkinje cells and eurydendroid cells.

There are two key points that suggest potential future applications of this algorithm. First, the successful validation on the Drosophila EM connectome demonstrates the versatility and potential for translation across multiple biological datasets of the method. To our knowledge, this is the first attempt to perform this kind of analysis on a brain-wide EM-connectome. Refinement of the pipeline to generate annotated EM datasets could provide additional benchmarks to test this method [56], as long as sufficient computational resources are available to perform the analysis. Second, the identification of communities with functional relevance in a synthetic structural connectome, where potential connections between neurons are defined by a proximity range[1], demonstrates the reliability and explanatory power of this tool. After the conceptualization of this project, a similar approach has been applied on the EM-connectome of part of the zebrafish brain stem comprising ~3000 neurons and ~75000 synapses. It resulted in the identification of two groups of strongly connected neurons that are involved in the control of the body movement and in the eye movement, respectively [134]. The latter, in particular, comprises neurons in the lateral medulla oblongata that project to abducens nucleis located more rostrally. Without using a EM-connectome, with our approach, we were able to distill from the ~3000 neurons contained in the zebrafish whole brain atlas a network with similar functional properties spanning multiple brain regions (Figure 3.7). This result weights evidence towards the reliability and potency of the tool.

1: Refer to [134] for an analysis on the effect of different proximity ranges on the potential connections

Whole brain imaging at cellular resolution Zebrafish larvae are one of the few model organisms that allows mapping of neuronal activity at cellular resolution across most of its brain. Traditionally, this takes advantage of the combination of fluorescence-based activity reporters expressed in genetically modified zebrafish lines, with microscopy techniques that rely on the extended illumination of the brain and the detection of the signal with a parallel detection. Among the different approaches developed, single-plane illumination or light sheet microscopy has become a powerful and versatile tool to reconstruct the fish neuronal dynamics brain wide. This technique is based on the illumination of the sample from the side with one or more thin sheets of light that are sequentially scanned along the dorso-ventral axis of the sample. The volumetric information is reconstructed with a CMOS or CCD camera by means of a second objective that is placed normally with respect to the

illumination sheet and continuously refocused at the illuminated plane. This approach typically leads to the reconstruction of the brain activity with cellular resolution at 1 or 2 volumes per second. We developed an alternative layout for volumetric imaging using a multiphoton microscope that includes a tunable lens at the back focal plane of the microscope objective, which is easy to implement. When functional recordings were made from an embedded zebrafish larvae during visual stimulation with a looming dot, we were able to segment approximately 48,000 neurons, or about 50% of the total neurons in the zebrafish brain. A hierarchical clustering approach on the identified stimulus-responsive neurons revealed four populations of neurons with distinct activity profiles. We mapped functionally characterized neurons to the brain atlas and found that the four populations are distributed across the brain, with a strong presence in the optic tectum, a result consistent with previous reports [174, 187].

Merging functional activity and circuit wiring diagram The systematic understanding of functional and structural connections between various cell types in the brain remains a challenge. Two methods have been attempted to tackle this issue: one being the use of electrophysiological recordings and dye-filling of randomly selected neuron pairs,followed by inspection of neuronal morphologies [188]. However, this kind of recording can be difficult due to the small sizes and dense packing of neurons. Another method is to use a genetic toolbox that enables in vivo detection of excitatory connections by using photostimulation of single cells and observing the downstream neuronal calcium responses [85]. An approach, that scale at a whole-brain level, involves recording neuronal activity from an organism and subsequently performing an EM reconstruction [29]. Although this method provides accurate results, it lacks the versatility to translate results across multiple individuals. The combination of the two tools presented in this thesis can provide an efficient and reliable pipeline for analyzing neural connectivity throughout the brain (Figure 6.1). For example, by registering in the same anatomical space the spatial coordinates of functionally characterized neurons selective to a particular stimulus (Figure 6.1B) and the one belonging to the identified communities (Figure 6.1C), it is possible to quantify their co-localization and assess the potential participation of the communities in the stimulus response (Figure 6.1D - E). How-

ever, some stimuli selective neurons may not be well co-localized with identified communities because of a lack of reconstructed morphological neurons (Figure 6.1D - white space).

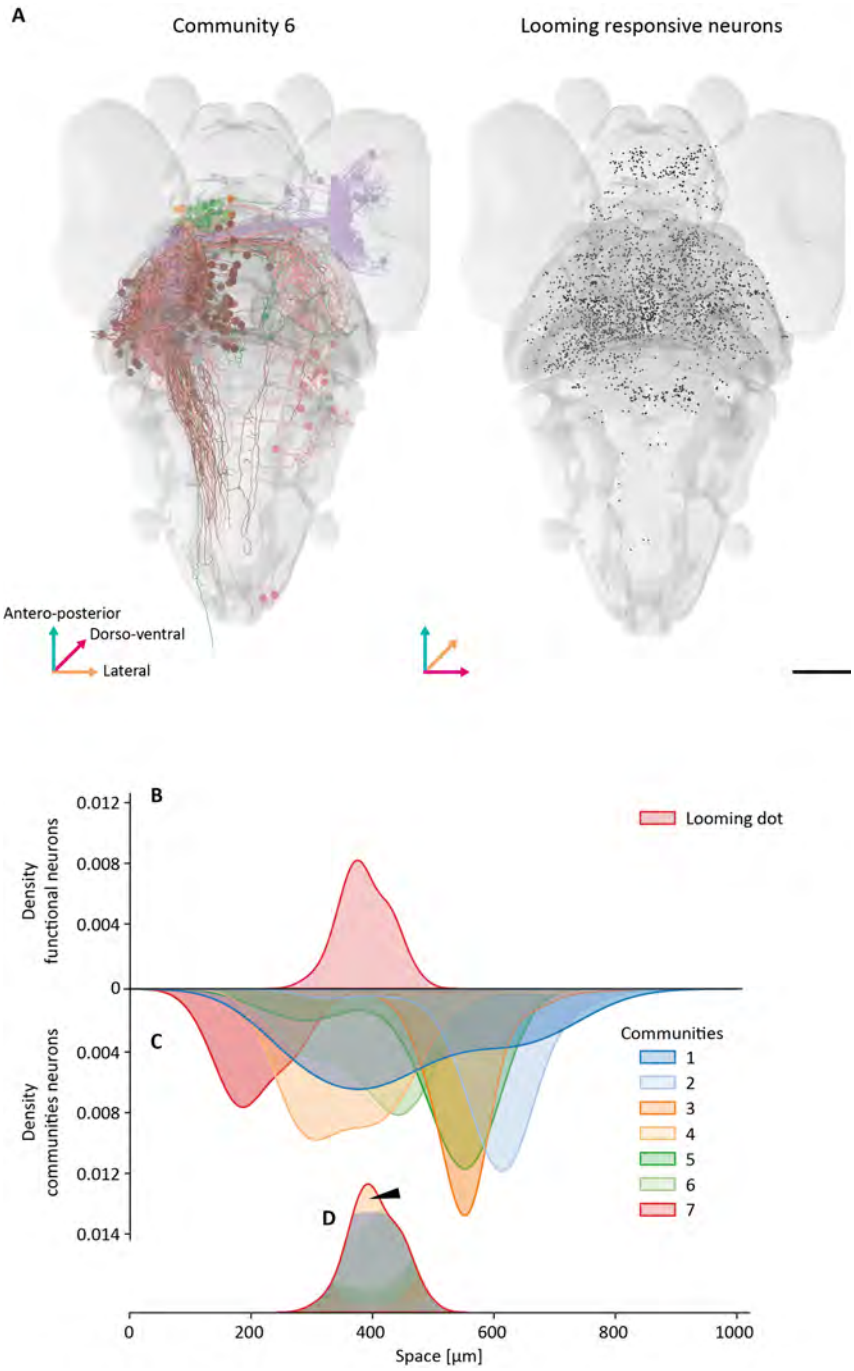

Figure 6.1: Co-localization of stimulus responsive neurons and communities.
(A) Example of neurons belonging to community 6 (left) belonging to a network involved in visuomotor transformations and looming responsive neurons (right). Scale bar = 100 μm. **(B)** Kernel density estimation of the rostro-caudal spatial coordinate of neurons responsive to looming stimuli. **(C)** Kernel density estimation of the rostro-caudal spatial coordinate of neurons belonging to different communities. **(D)** Co-localization of looming responsive neurons with neurons belonging to the communities. Arrow-head indicate more represented community.

Conclusion We have developed a framework to study the brain activity of zebrafish larvae that uses an algorithm to identify functional networks based on structural connectivity patterns and a technique for visualizing neuronal activity throughout the brain at cellular level. The combination of these two tools can

provide deep insight into how nervous system structure supports information flow and prepare a more solid basis to develop circuit explanatory models.

Contribution 7

The contribution to each of the chapters described above is reported. The order of the names reflects the amount of contribution.

- Results: Analysis of the zebrafish larva brain wiring diagram (Chapter 3)
  - Building the zebrafish larva brain connectome (Section 3.1): Karan Manjunatha, Matteo Bruzzone
  - Topological properties of the zebrafish connectome (Section 3.1): Karan Manjunatha, Matteo Bruzzone
  - Identify the communities (Section 3.3): Karan Manjunatha, Matteo Bruzzone
  - Biological description of the communities (Section 3.3): Matteo Bruzzone
- Results: Whole brain imaging at cellular resolution (Chapter 4)
  - Development of a configuration for 3D scanning multiphoton microscopy (Section 4.1): Enrico Chiarello, Matteo Bruzzone
  - Optical properties of the 3D scanning configuration (Section 4.2): Matteo Bruzzone, Enrico Chiarello
  - Whole brain neuronal recordings (Section 4.3): Matteo Bruzzone
- Results: Analysis of $Galn^+$ and Crh^+ (Chapter 5)
  - Identification of Crh^+ neurons in the zebrafish preoptic area (Section 5.1): Matteo Bruzzone, Laura Corradi
  - Characterization of $Galn^+$ and Crh^+ neurons responses (Section 5.2): Matteo Bruzzone

Appendix

Most of the codes related to published data are available at https://github.com/dalMaschio-lab/Bruzzone2021_tunableLens.
Codes used for the analysis of the circuit wiring diagram will be made available upon publication of the related content.

Supplementary Figures

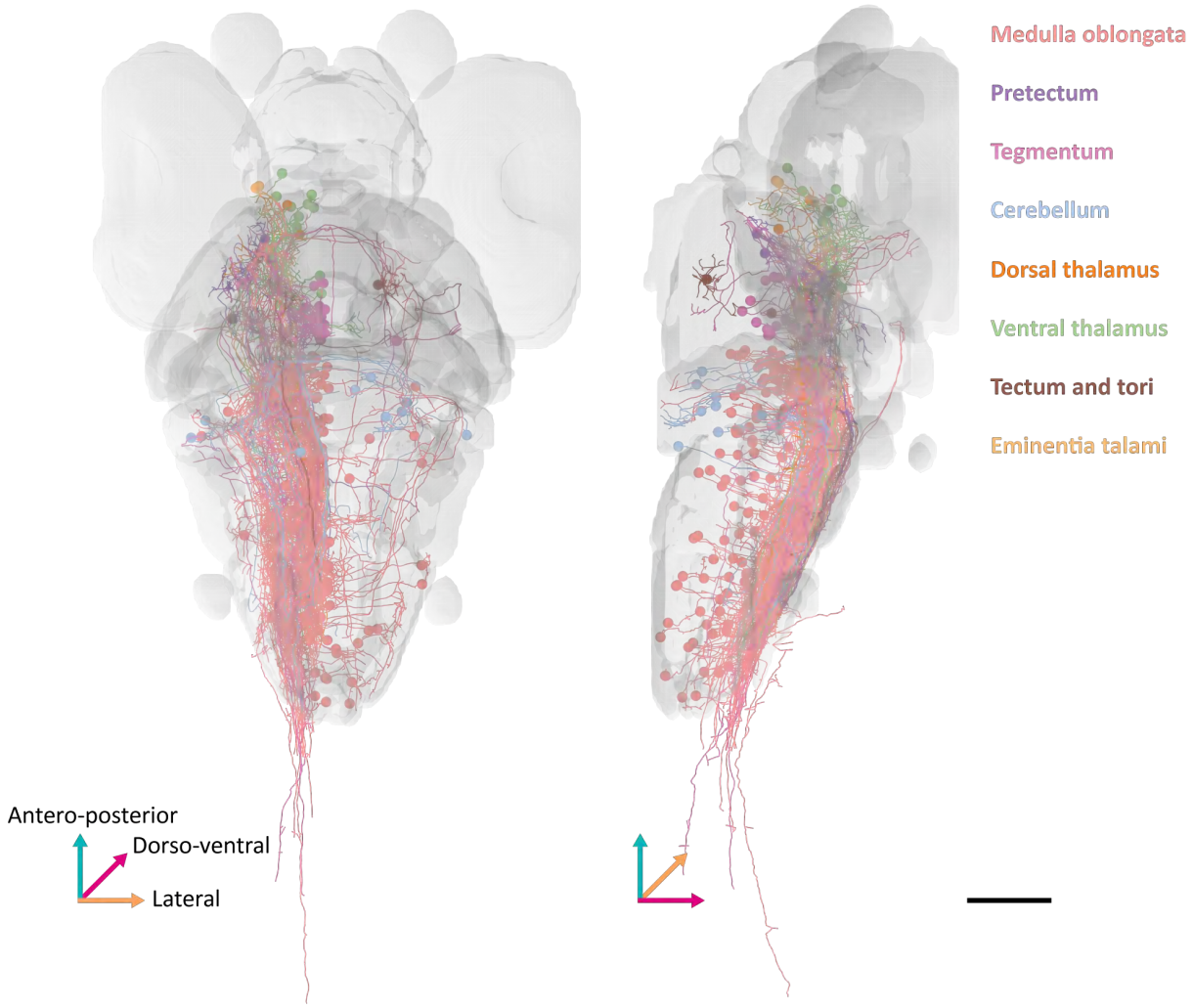

Figure 7.1: Community 1 subcommunity 1.
Projections of the neurons found in the subcommunity. Colors are assigned based on soma location. Scale bar = 100 μm

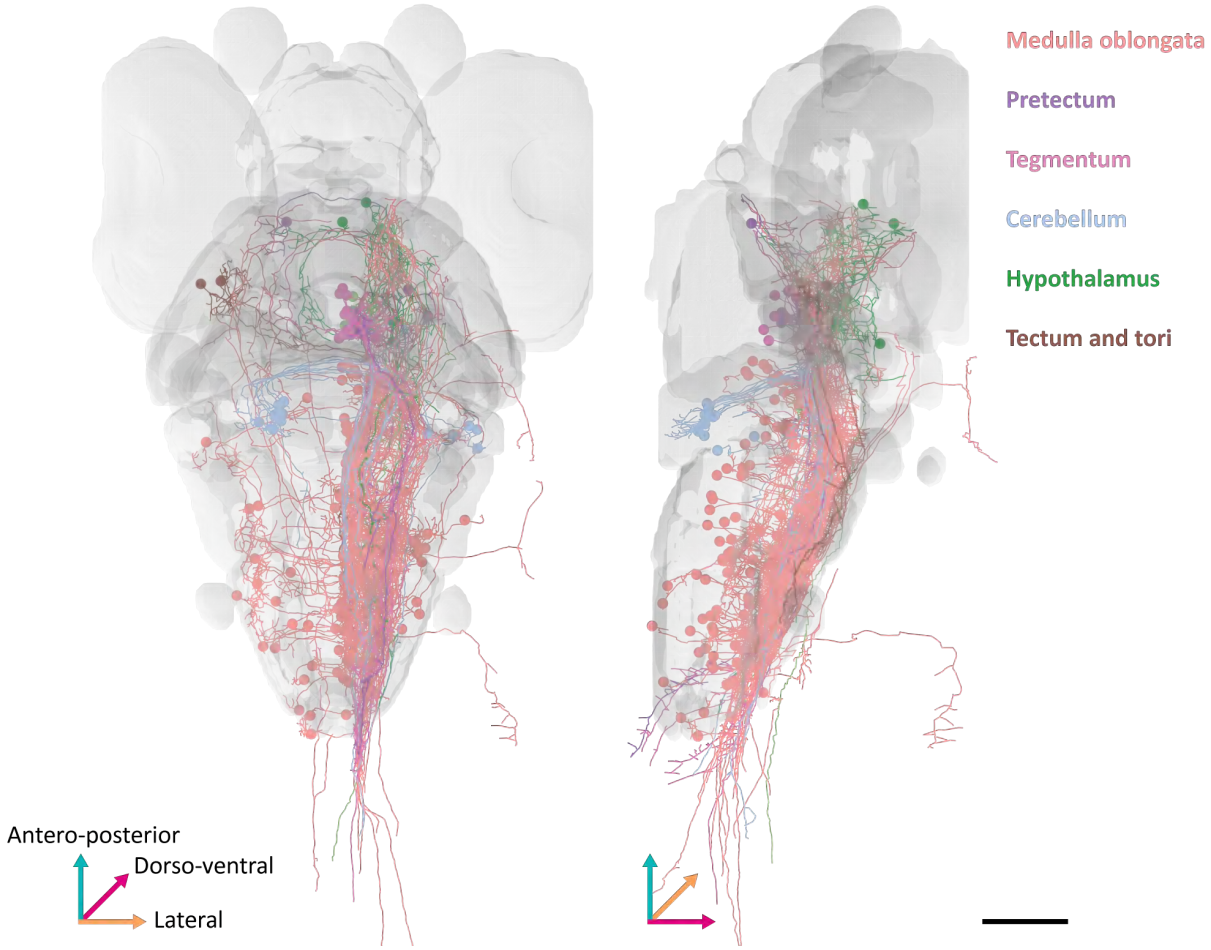

Figure 7.2: Community 1 subcommunity 2.
Projections of the neurons found in the subcommunity. Colors are assigned based on soma location. Scale bar = 100 μm

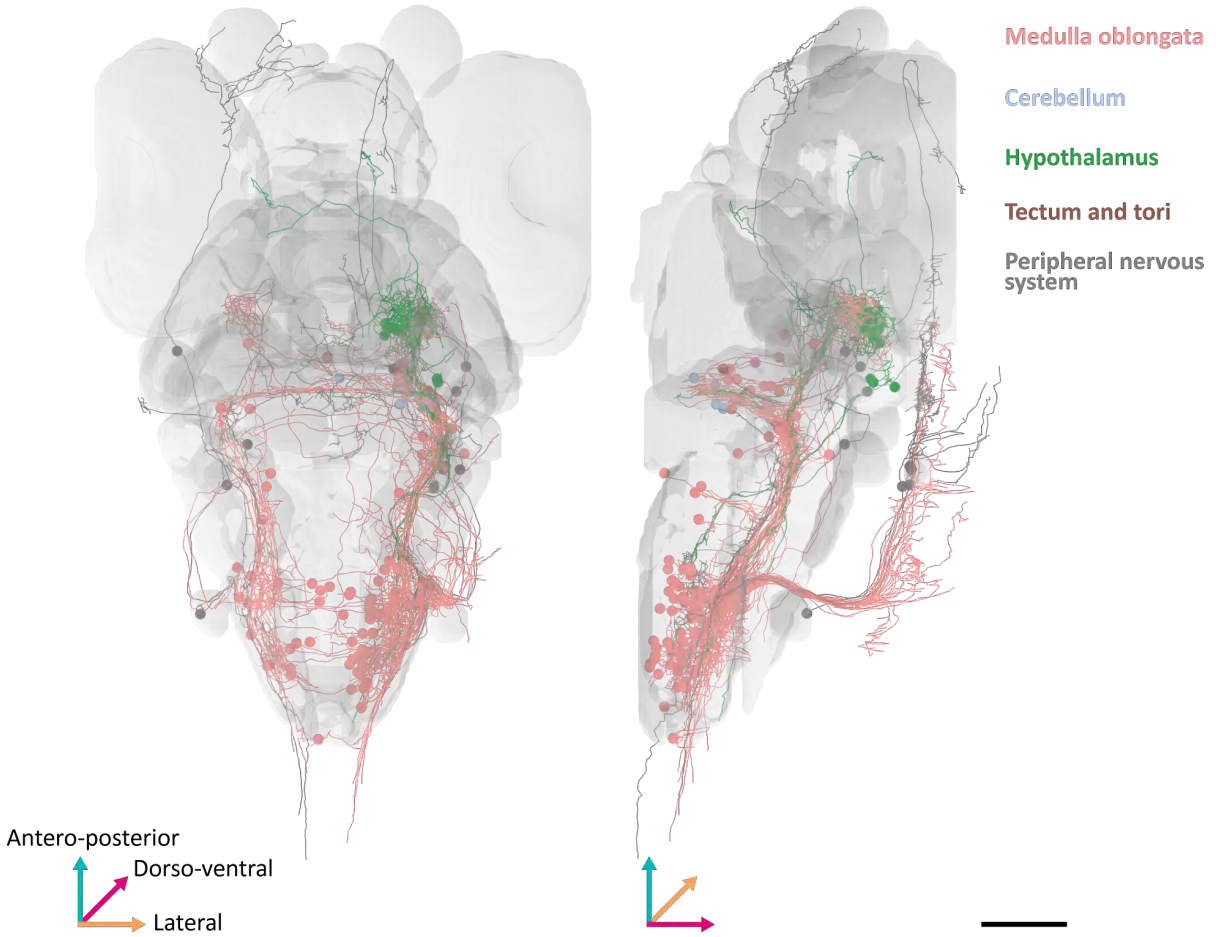

Figure 7.3: Community 1 subcommunity 3.
Projections of the neurons found in the subcommunity. Colors are assigned based on soma location. Scale bar = 100 μm

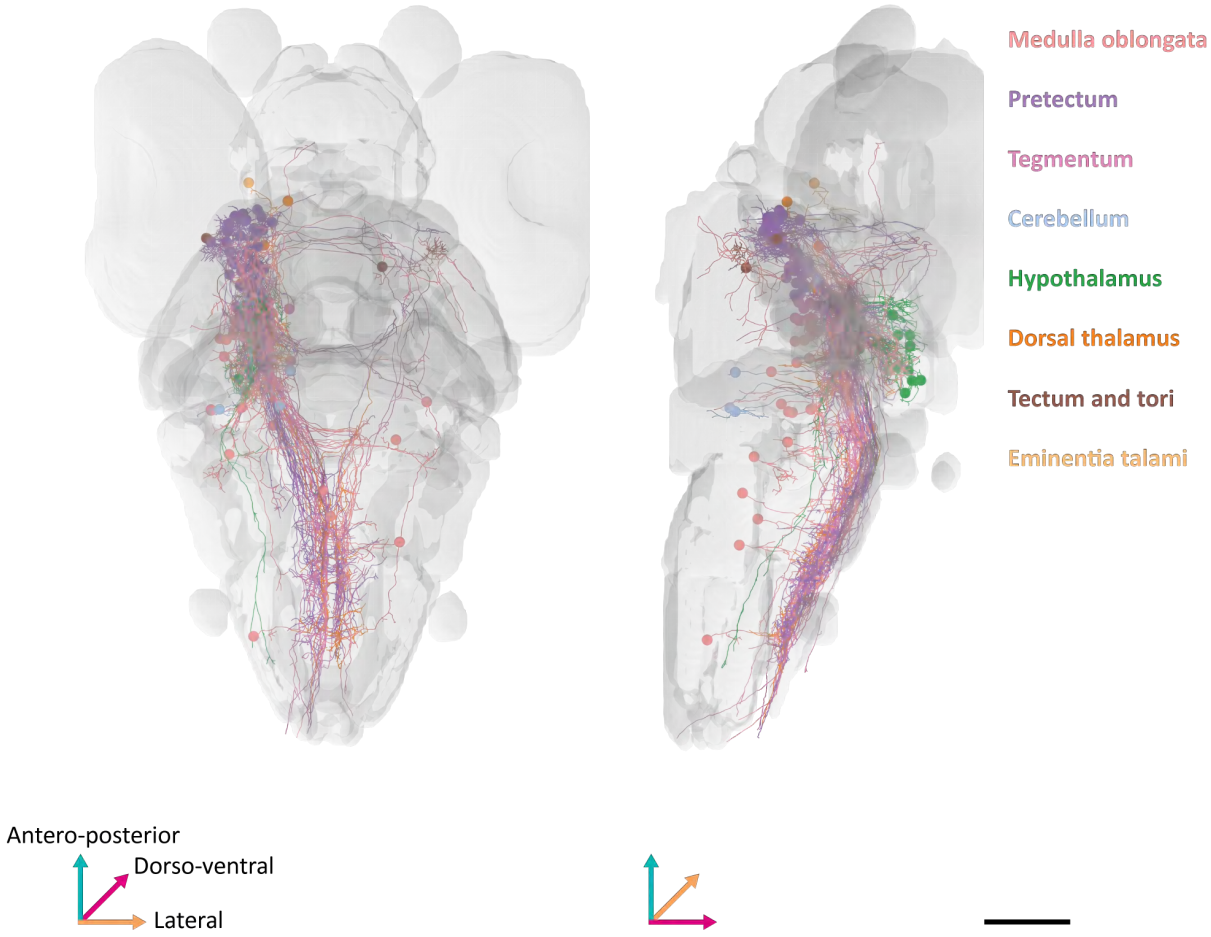

Figure 7.4: Community 1 subcommunity 4.
Projections of the neurons found in the subcommunity . Colors are assigned based on soma location.
Scale bar = 100 μm

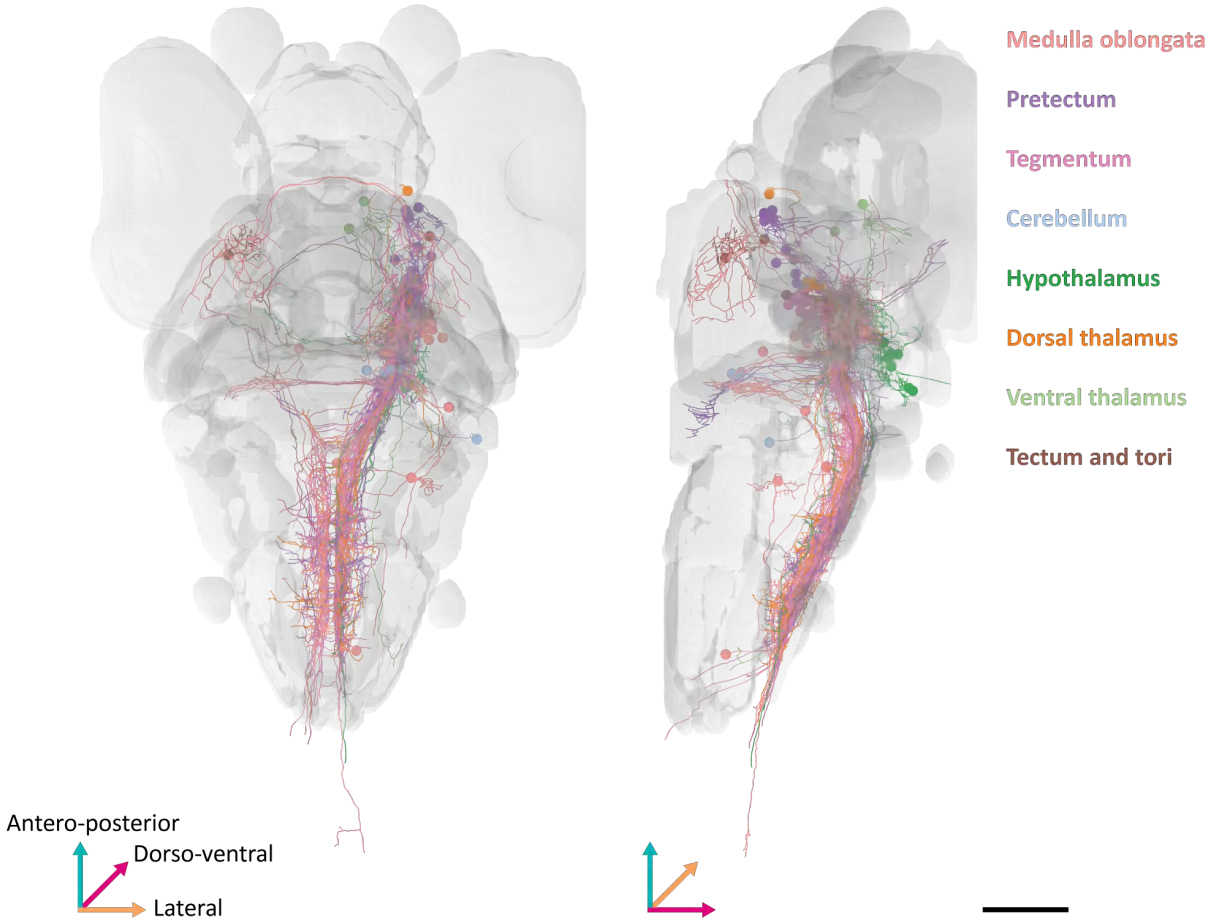

Figure 7.5: Community 1 subcommunity 5.
Projections of the neurons found in the subcommunity. Colors are assigned based on soma location. Scale bar = 100 μm

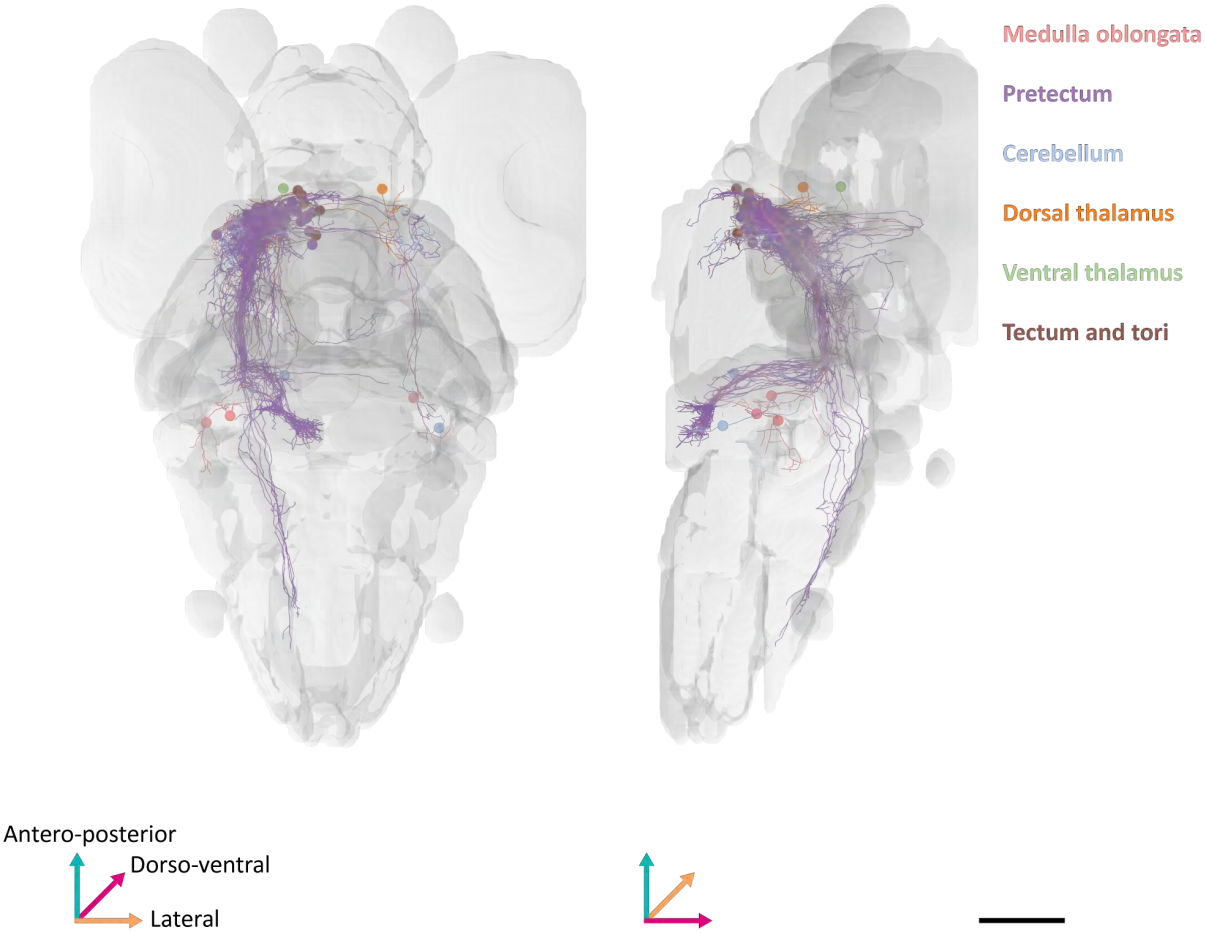

Figure 7.6: Community 1 subcommunity 6.
Projections of the neurons found in the subcommunity. Colors are assigned based on soma location. Scale bar = 100 μm

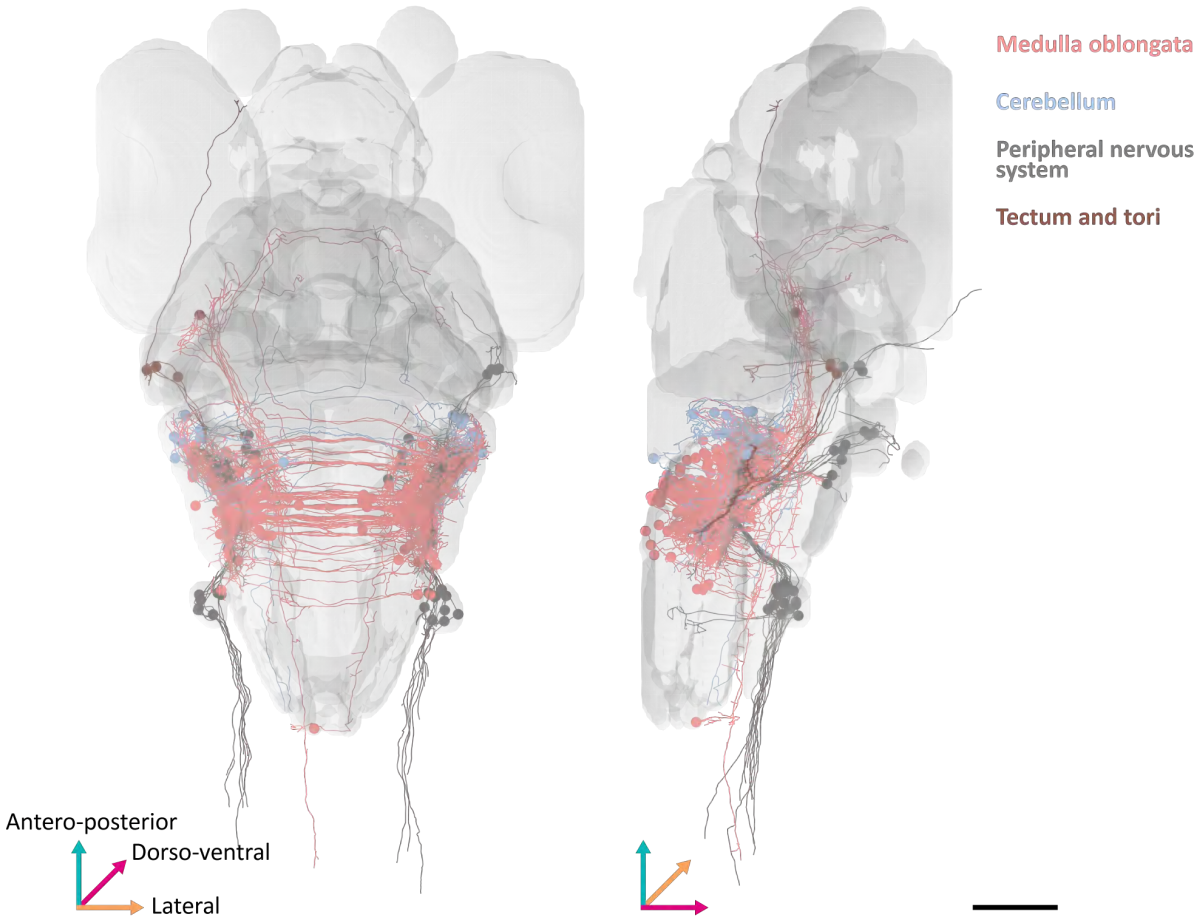

Figure 7.7: Community 2 subcommunity 1.
Projections of the neurons found in the subcommunity. Colors are assigned based on soma location. Scale bar = 100 μm

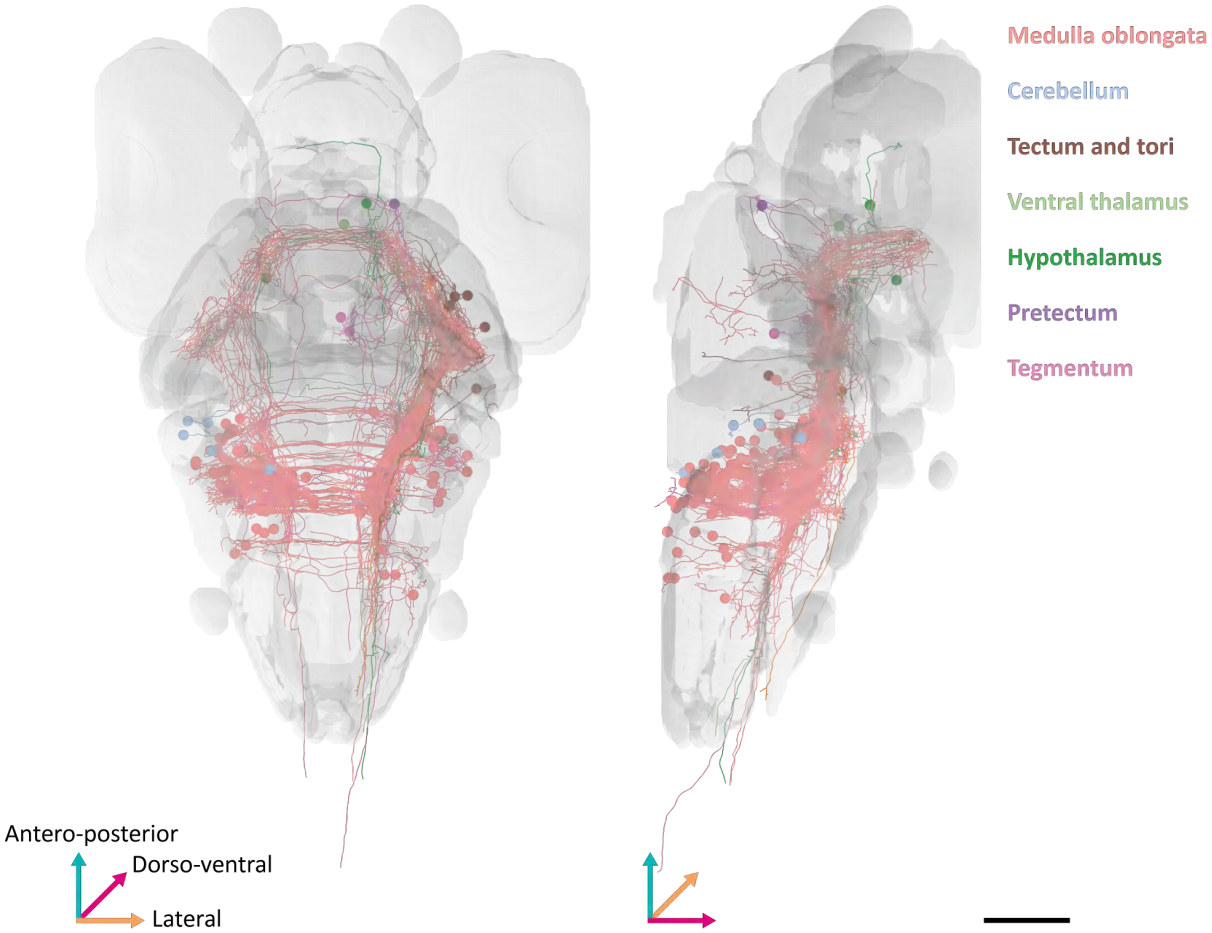

Figure 7.8: Community 2 subcommunity 2.
Projections of the neurons found in the subcommunity. Colors are assigned based on soma location. Scale bar = 100 μm

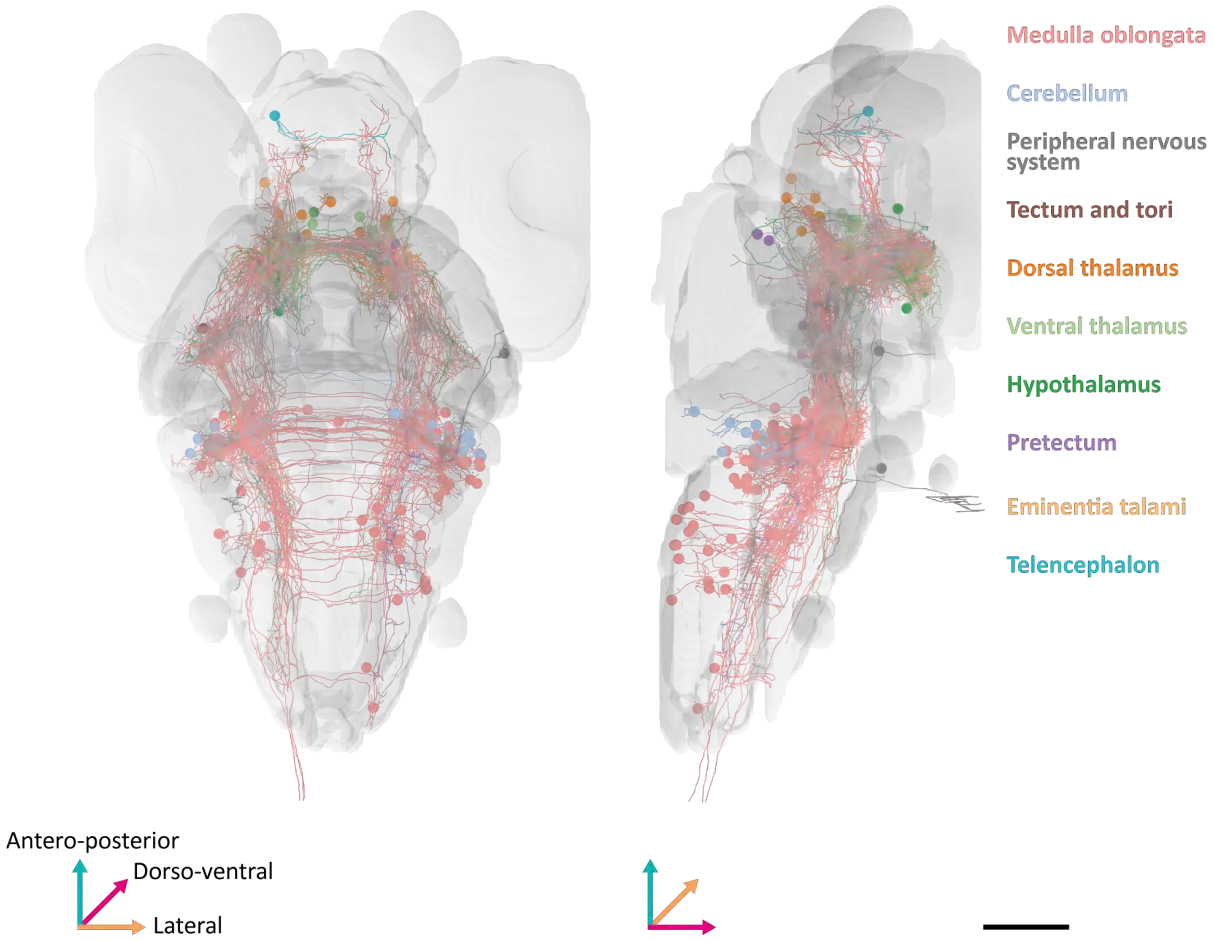

Figure 7.9: Community 2 subcommunity 3.
Projections of the neurons found in the subcommunity. Colors are assigned based on soma location. Scale bar = 100 μm

Figure 7.10: Community 2 subcommunity 4.
Projections of the neurons found in the subcommunity. Colors are assigned based on soma location. Scale bar = 100 μm

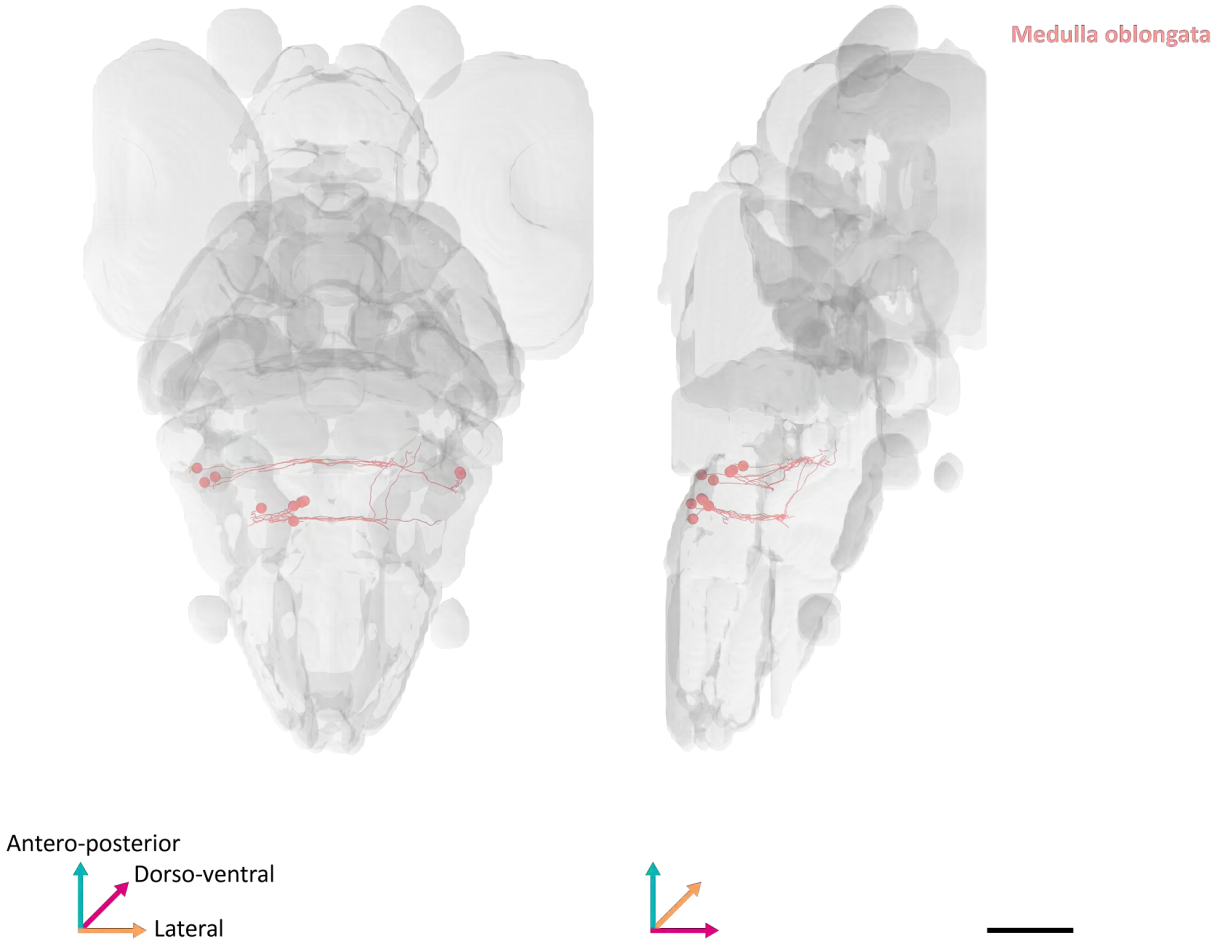

Figure 7.11: Community 2 subcommunity 5.
Projections of the neurons found in the subcommunity. Colors are assigned based on soma location. Scale bar = 100 μm

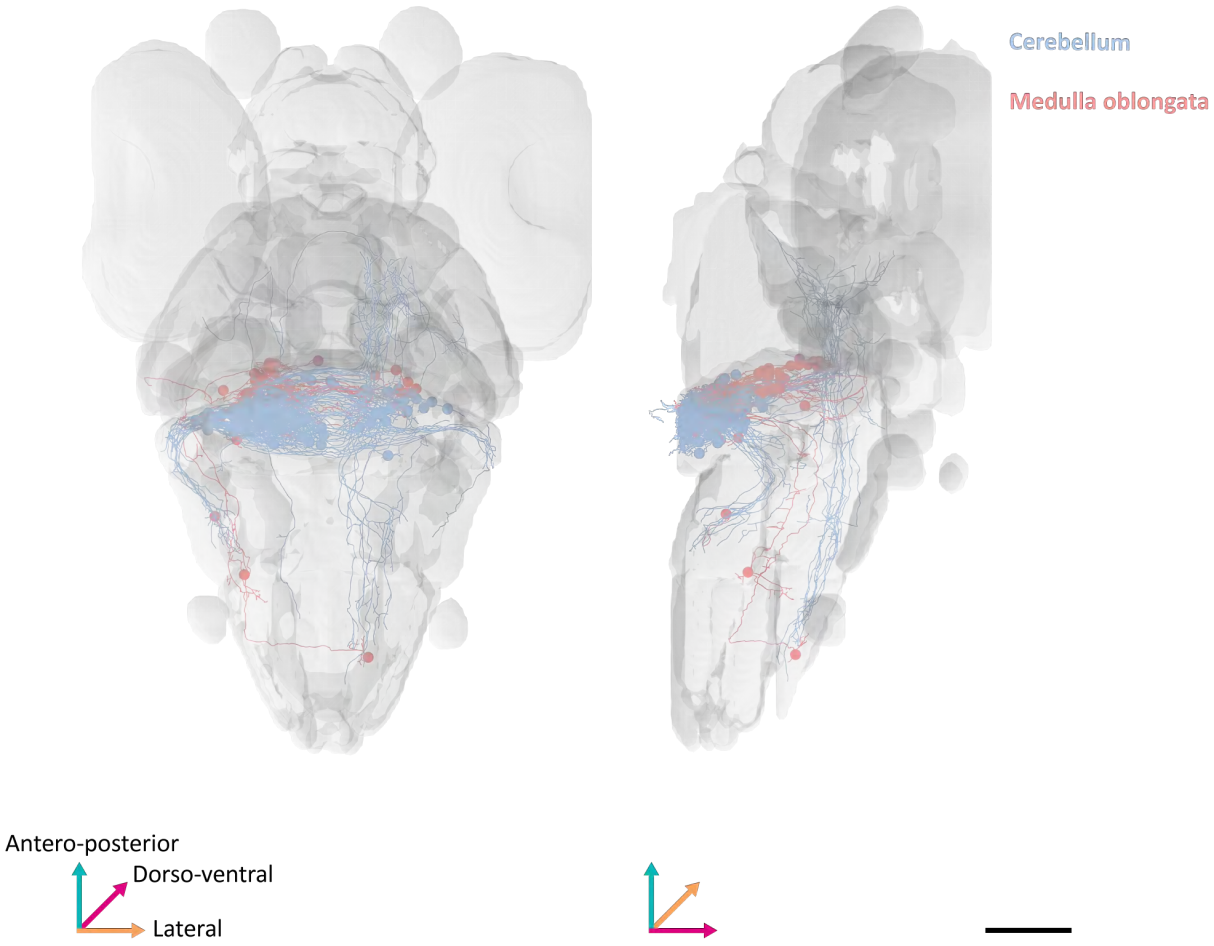

Figure 7.12: Community 3 subcommunity 1.
Projections of the neurons found in the subcommunity. Colors are assigned based on soma location. Scale bar = 100 μm

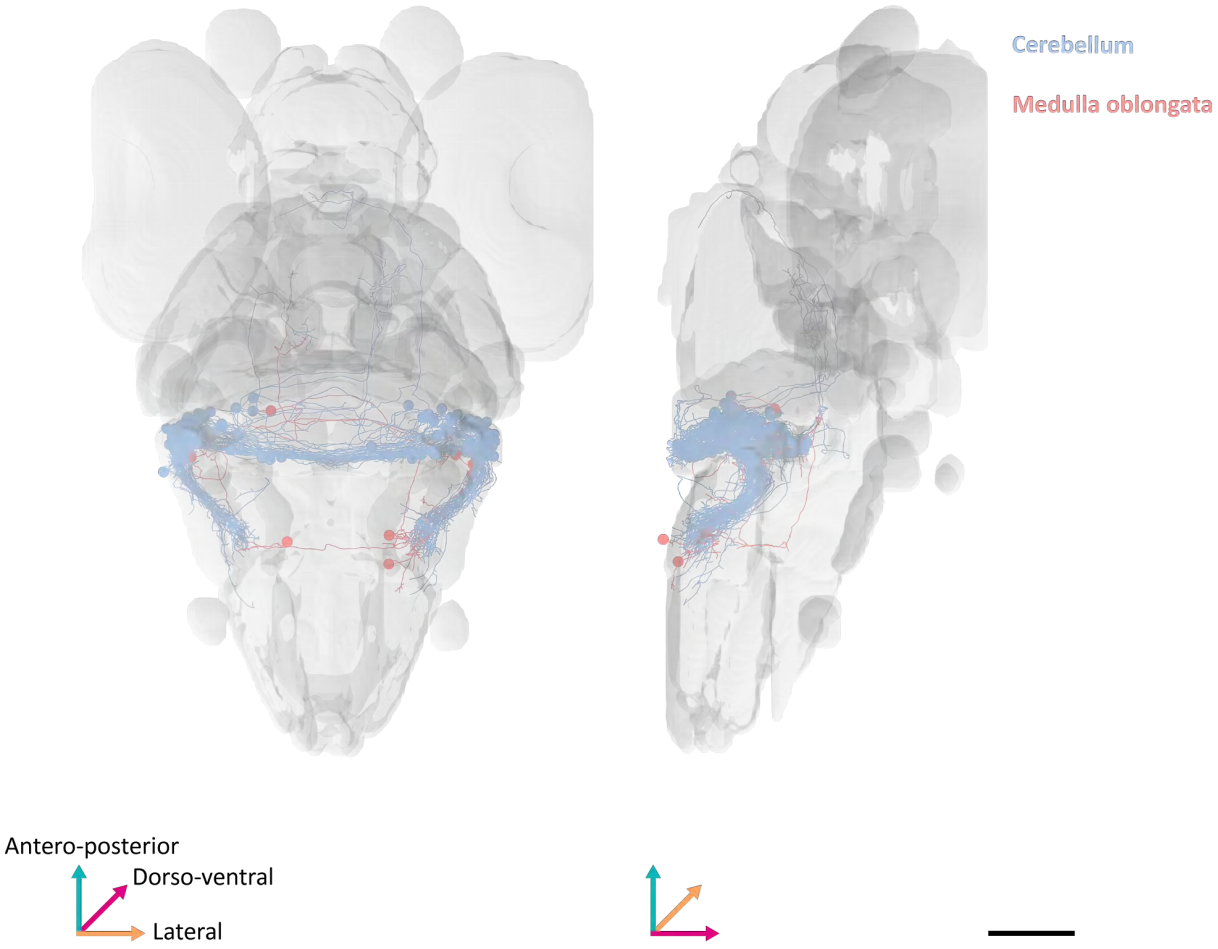

Figure 7.13: Community 3 subcommunity 2.
Projections of the neurons found in the subcommunity. Colors are assigned based on soma location. Scale bar = 100 μm

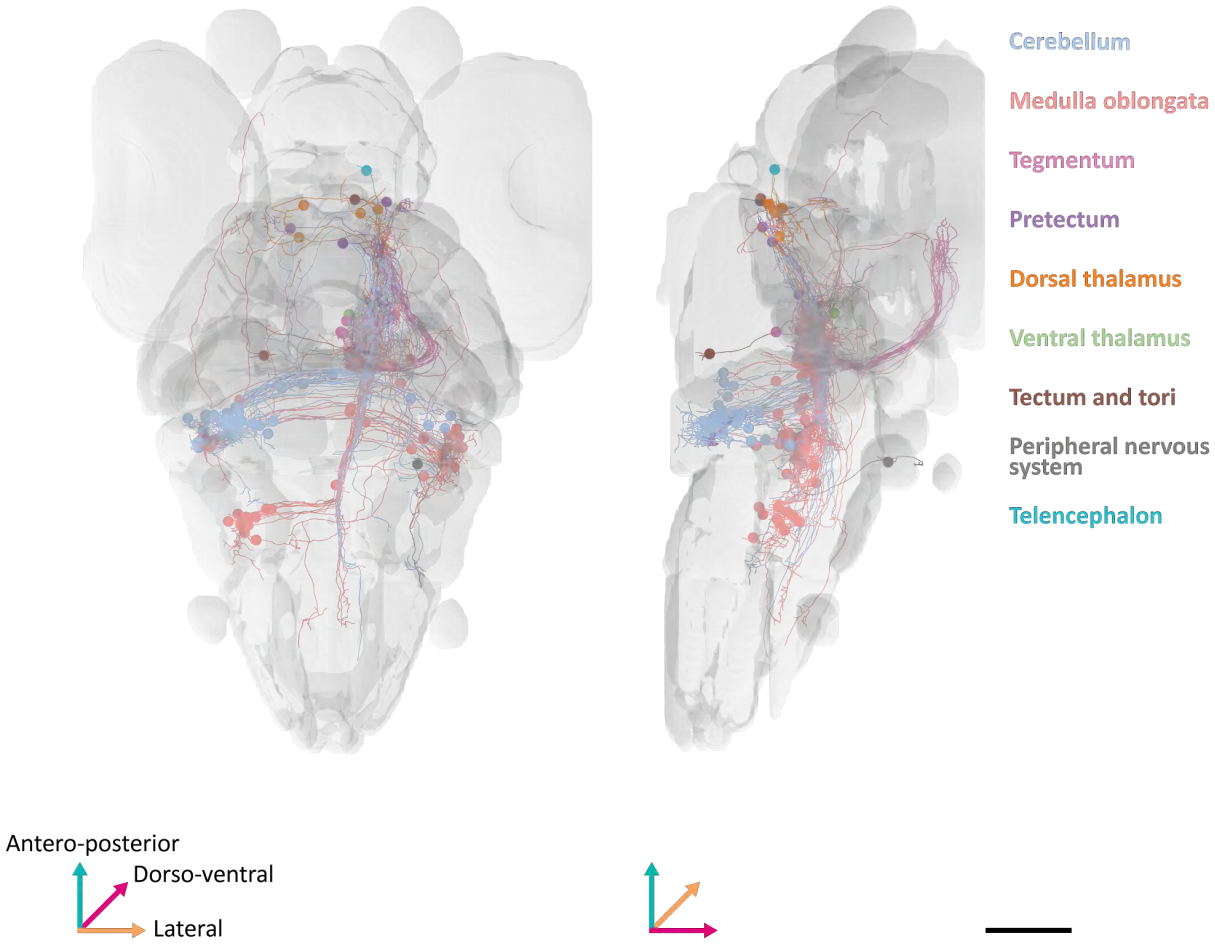

Figure 7.14: Community 3 subcommunity 3.
Projections of the neurons found in the subcommunity. Colors are assigned based on soma location. Scale bar = 100 μm

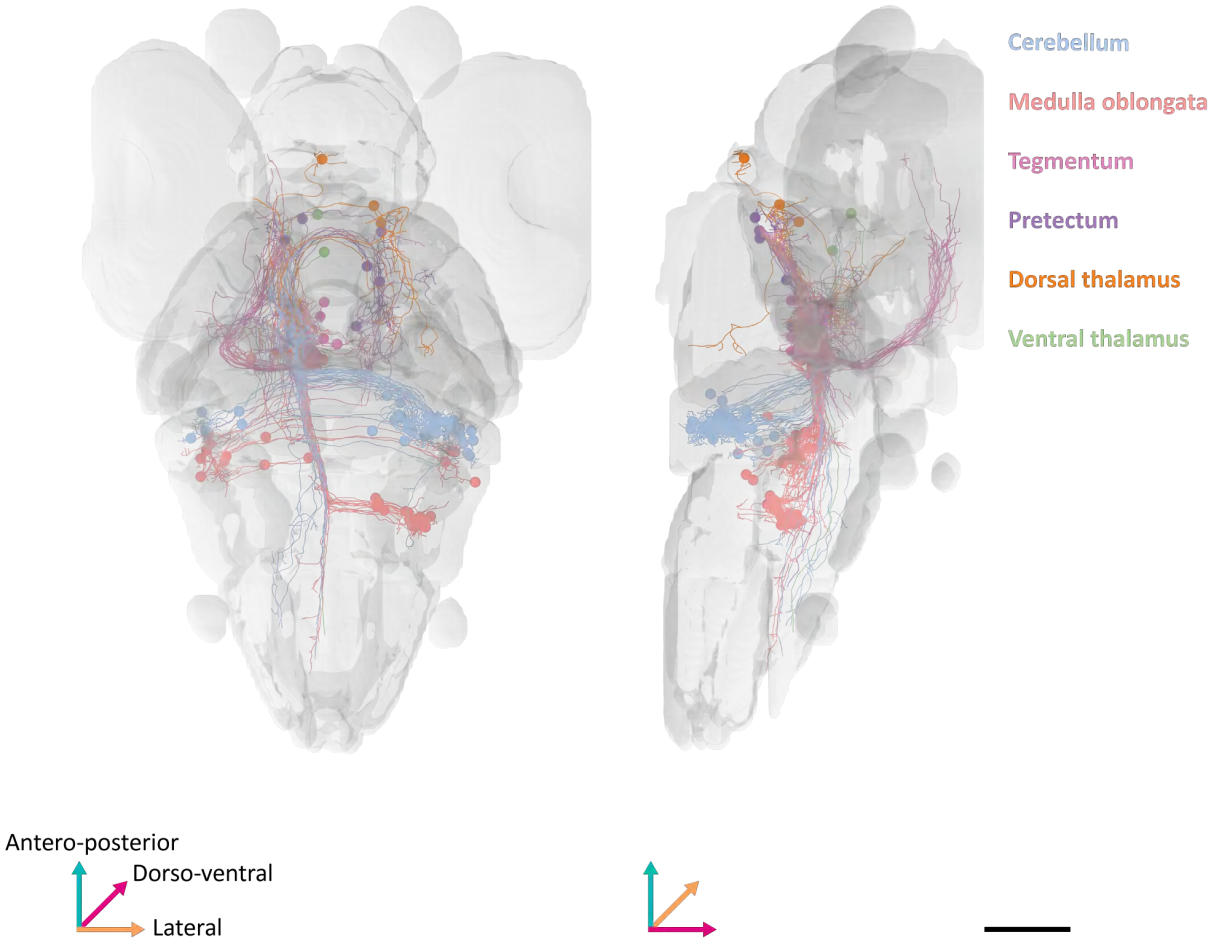

Figure 7.15: Community 3 subcommunity 4.
Projections of the neurons found in the subcommunity. Colors are assigned based on soma location. Scale bar = 100 μm

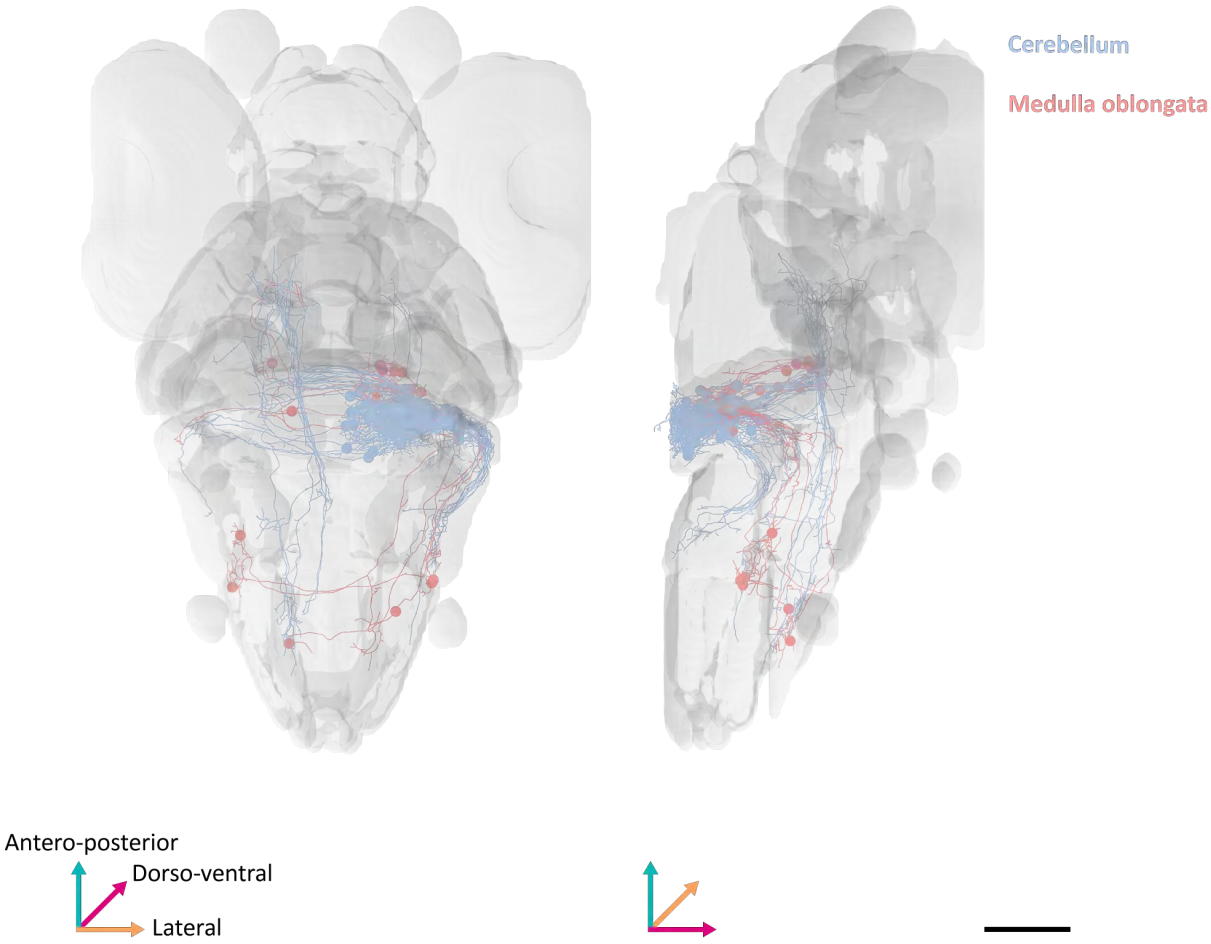

Figure 7.16: Community 3 subcommunity 5.
Projections of the neurons found in the subcommunity. Colors are assigned based on soma location. Scale bar = 100 μm

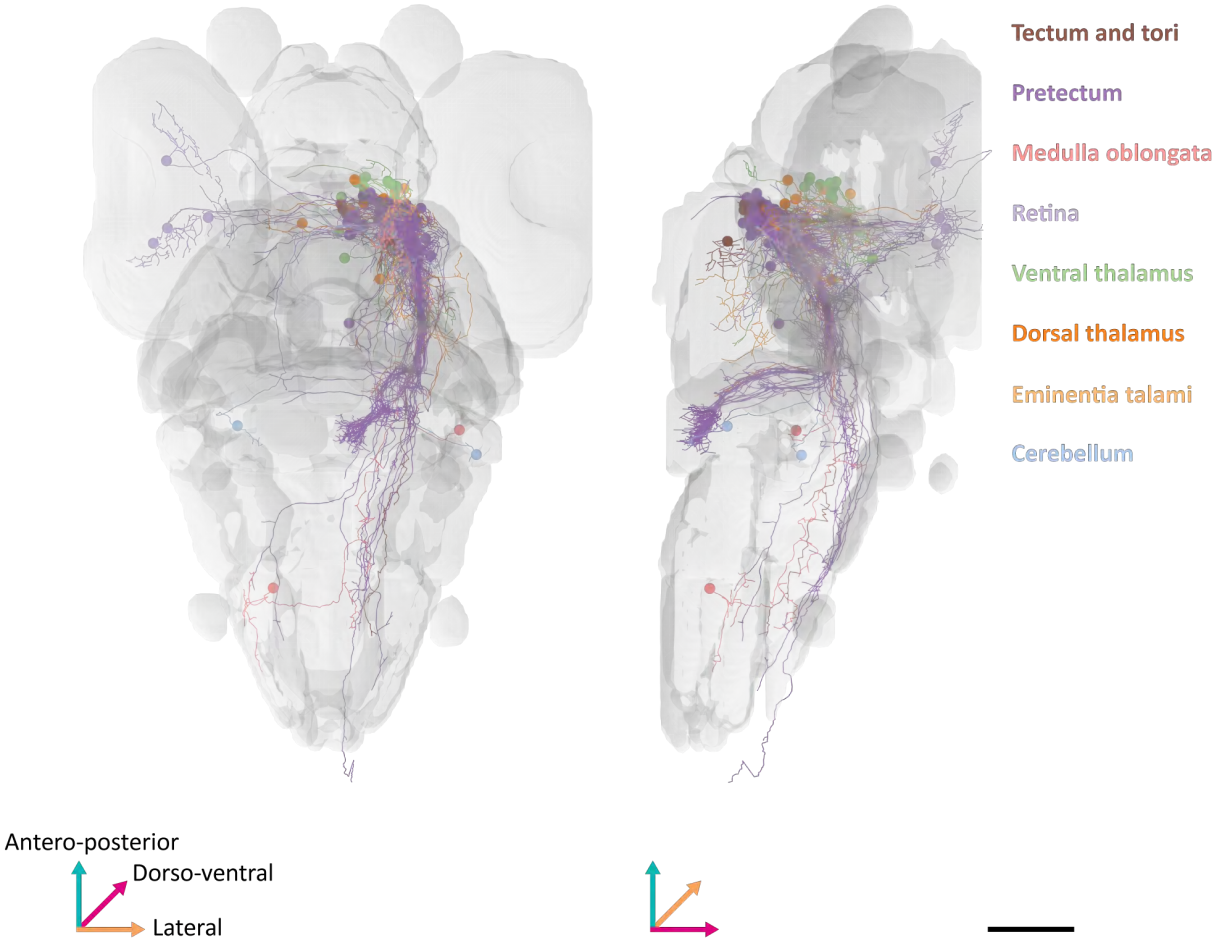

Figure 7.17: Community 4 subcommunity 1.
Projections of the neurons found in the subcommunity. Colors are assigned based on soma location. Scale bar = 100 μm

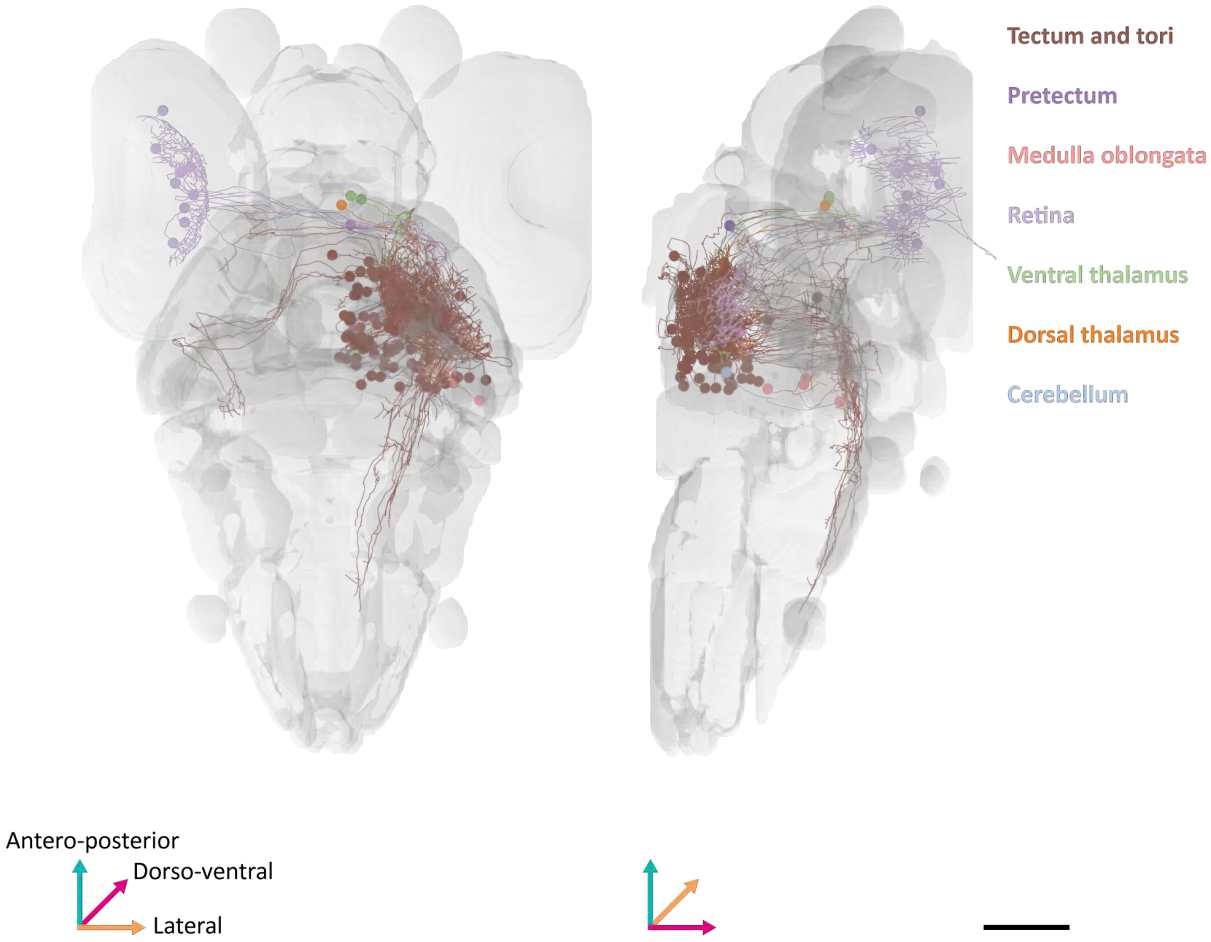

Figure 7.18: Community 4 subcommunity 2.
Projections of the neurons found in the subcommunity. Colors are assigned based on soma location. Scale bar = 100 μm

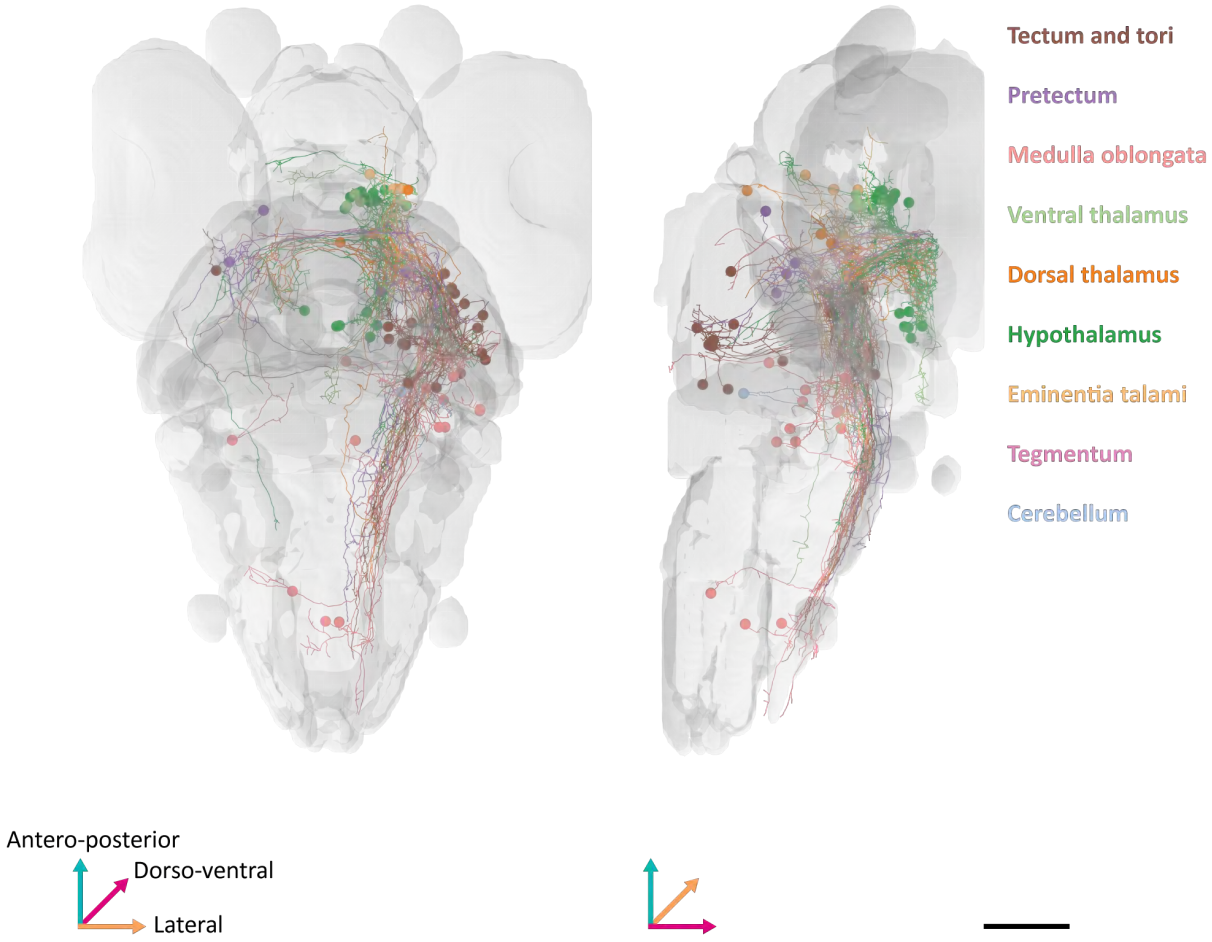

Figure 7.19: Community 4 subcommunity 3.
Projections of the neurons found in the subcommunity. Colors are assigned based on soma location. Scale bar = 100 μm

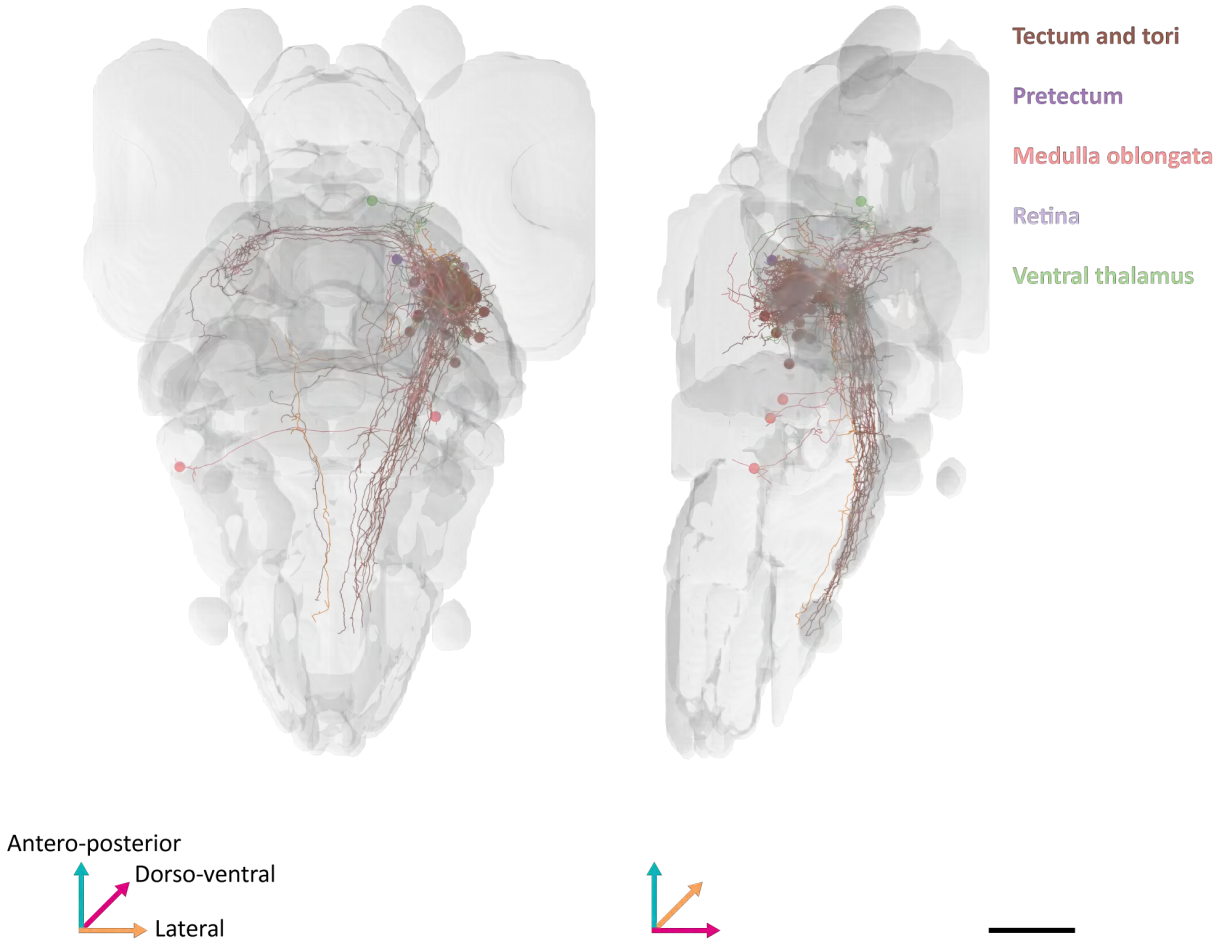

Figure 7.20: Community 4 subcommunity 4.
Projections of the neurons found in the subcommunity. Colors are assigned based on soma location. Scale bar = 100 μm

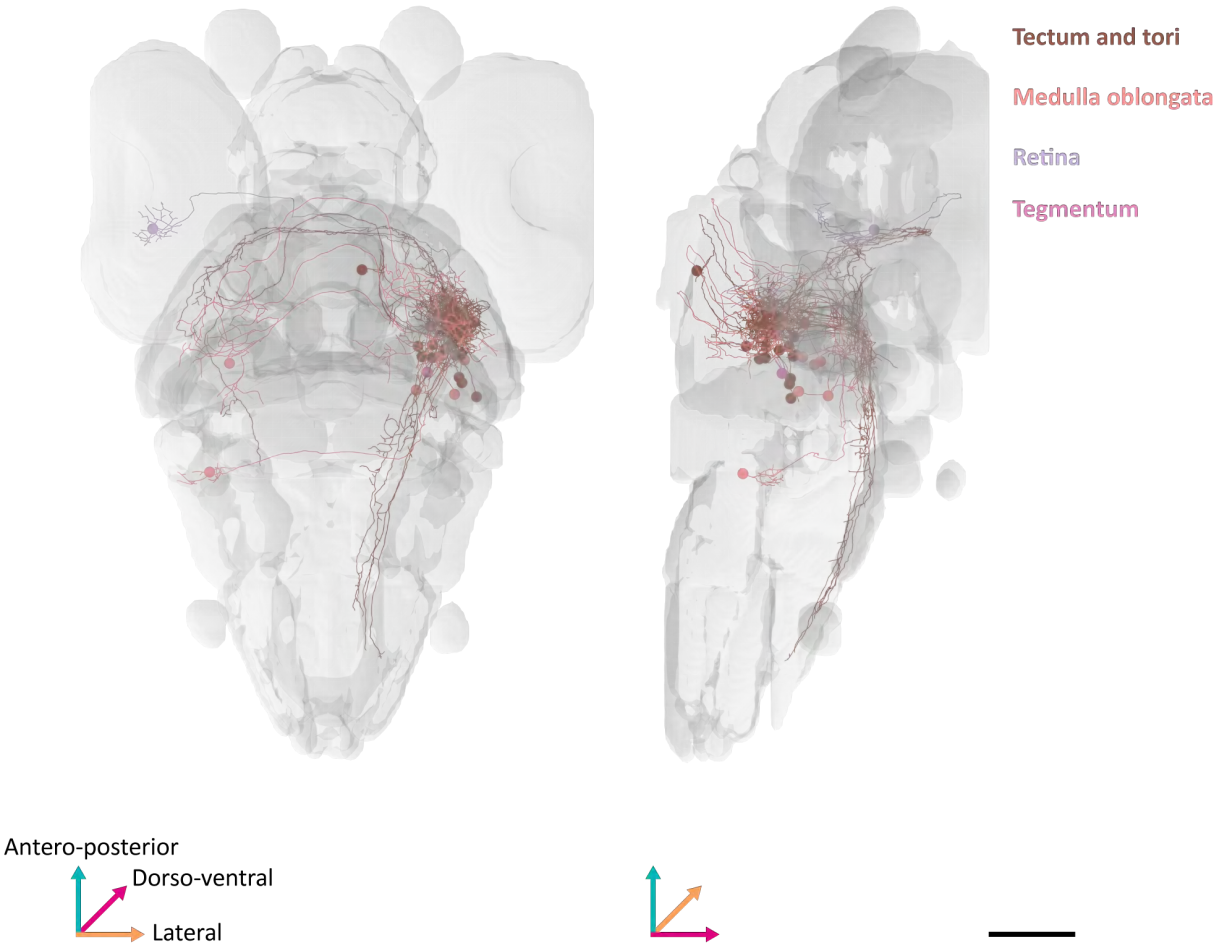

Figure 7.21: Community 4 subcommunity 5.
Projections of the neurons found in the subcommunity. Colors are assigned based on soma location. Scale bar = 100 μm

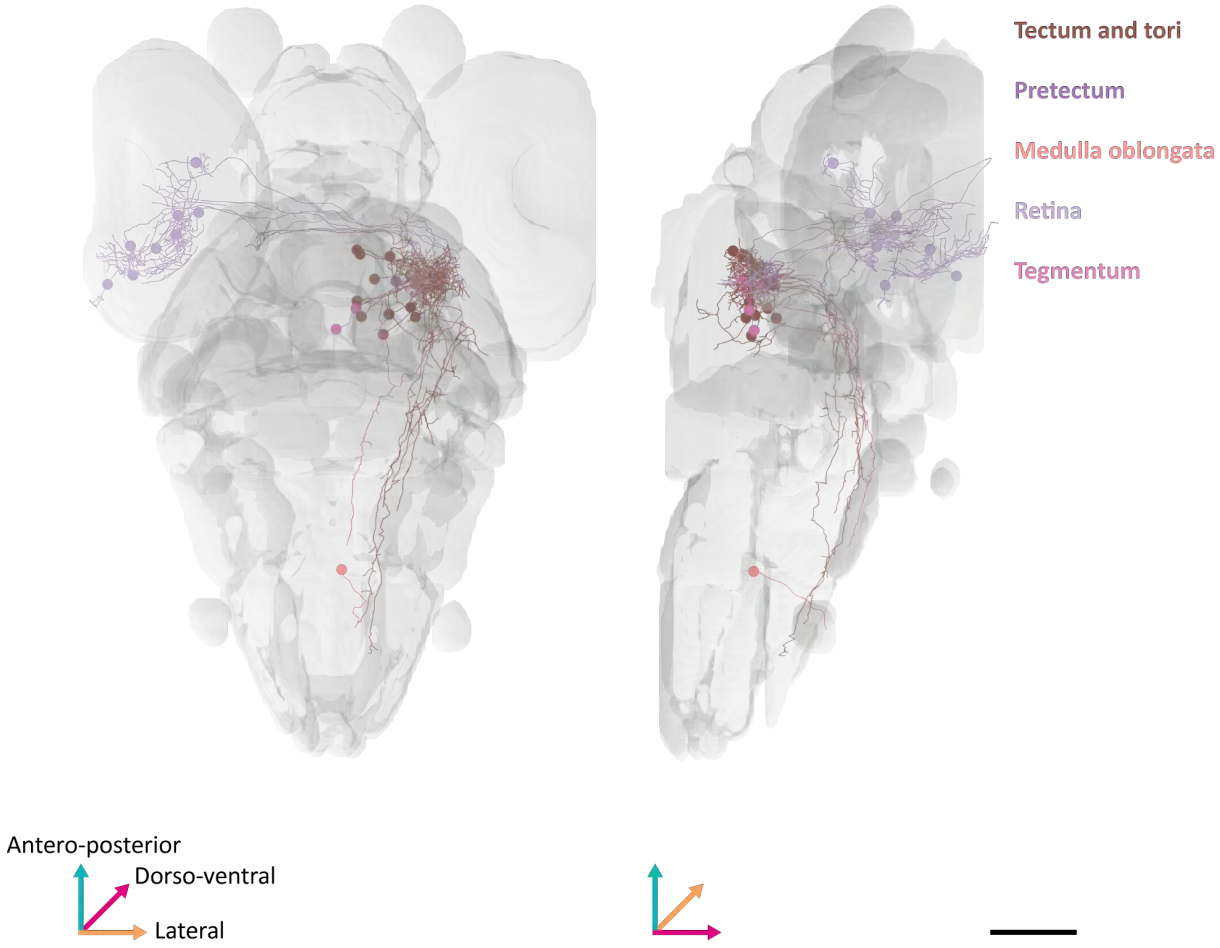

Figure 7.22: Community 4 subcommunity 5.
Projections of the neurons found in the subcommunity. Colors are assigned based on soma location. Scale bar = 100 μm

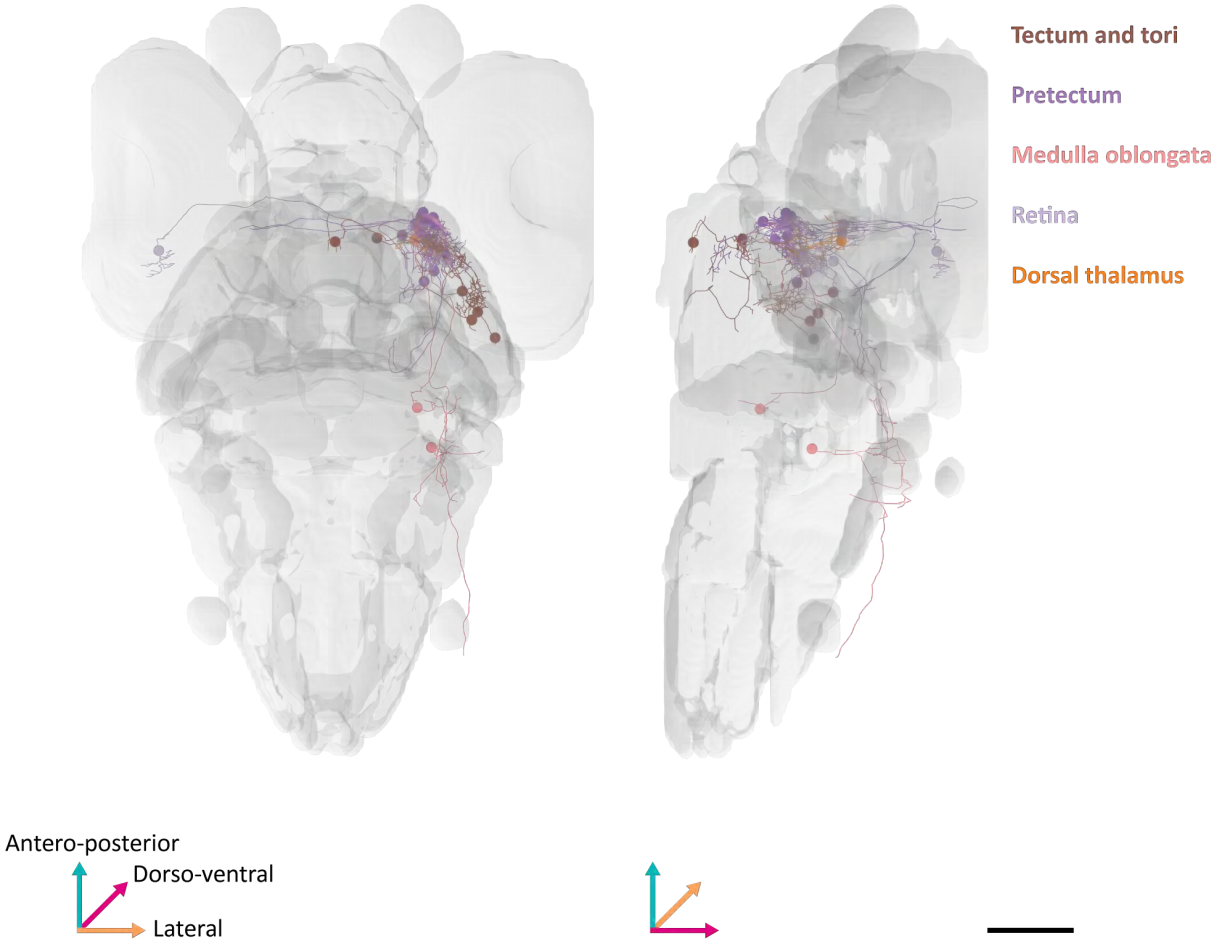

Figure 7.23: Community 4 subcommunity 7.
Projections of the neurons found in the subcommunity. Colors are assigned based on soma location. Scale bar = 100 μm

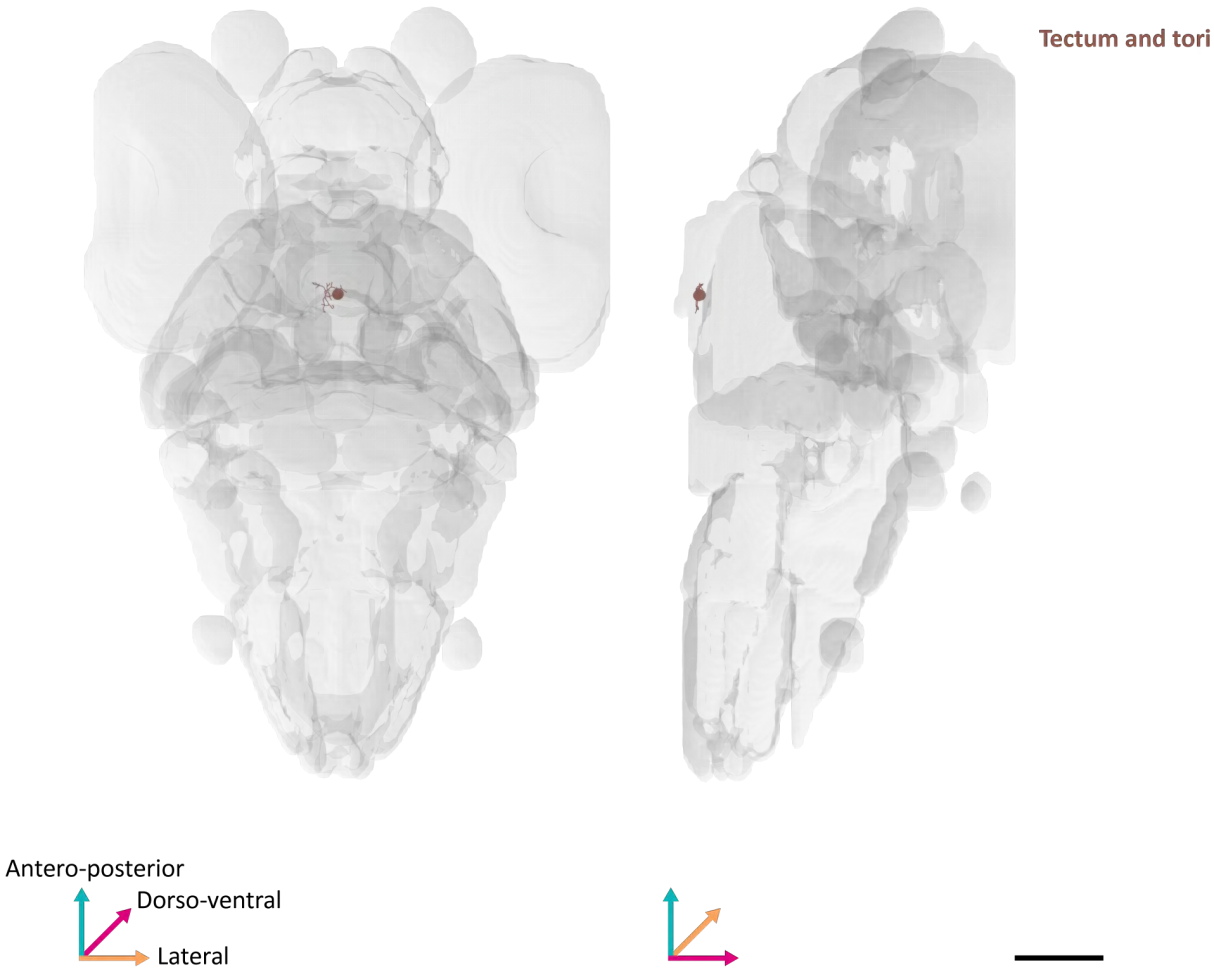

Figure 7.24: Community 4 subcommunity 8.
Projections of the neurons found in the subcommunity. Colors are assigned based on soma location. Scale bar = 100 μm

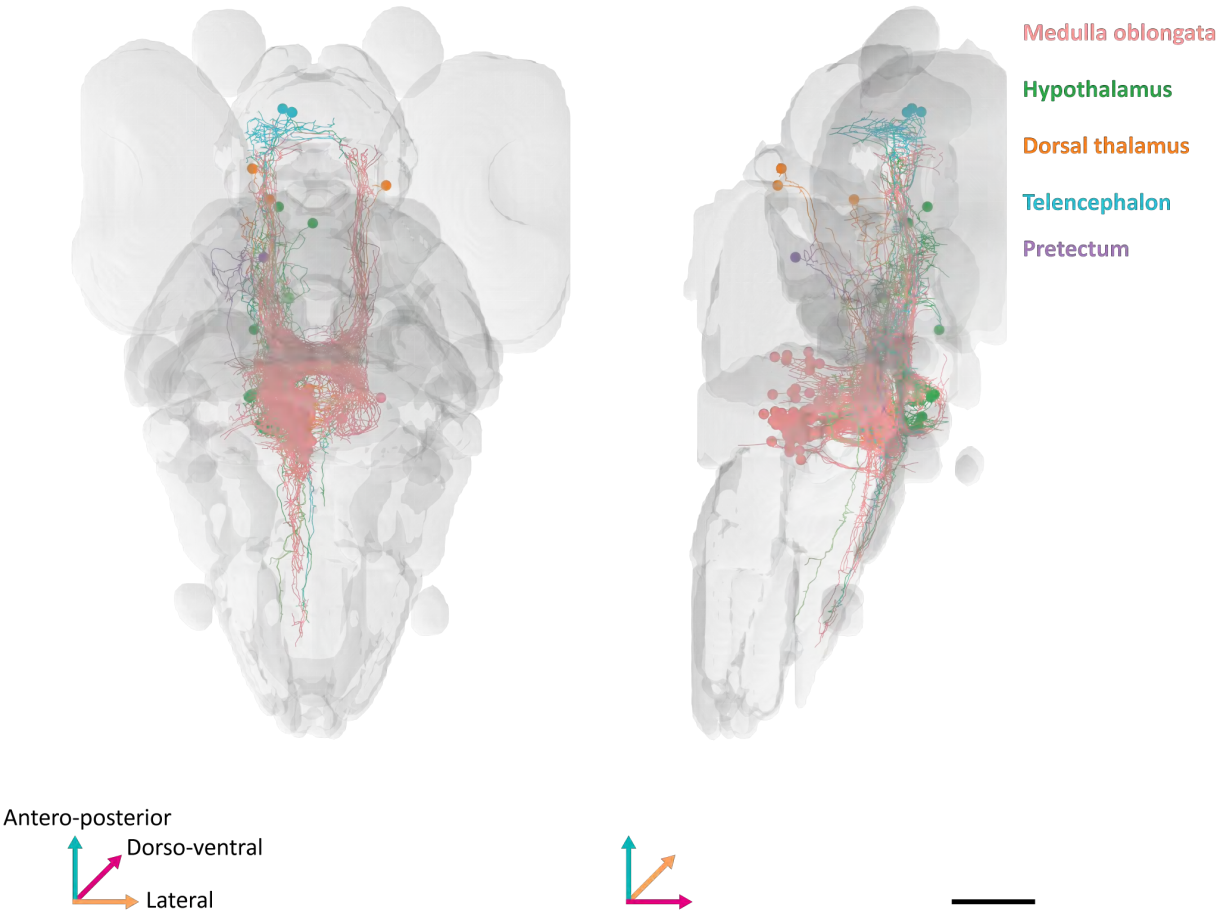

Figure 7.25: Community 5 subcommunity 1.
Projections of the neurons found in the subcommunity. Colors are assigned based on soma location. Scale bar = 100 μm

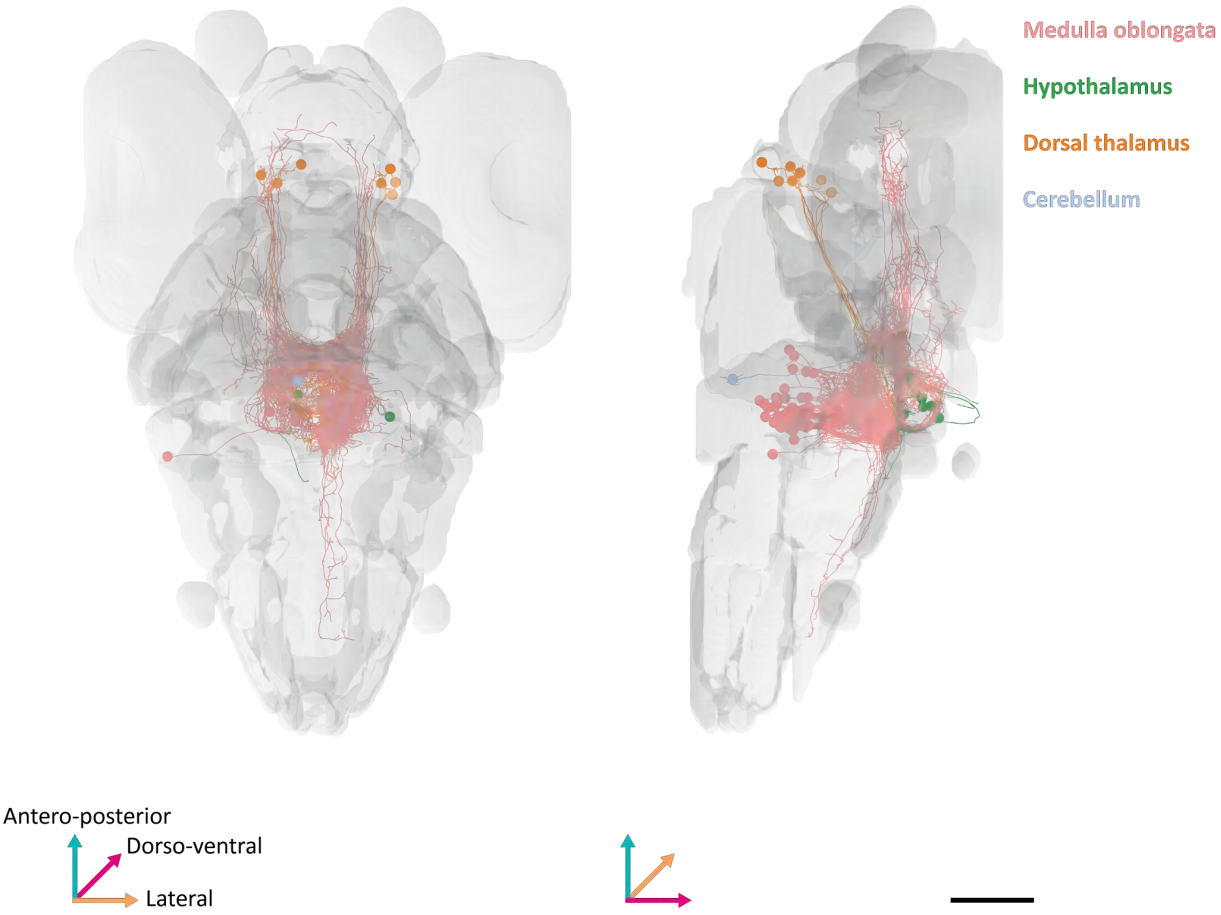

Figure 7.26: Community 5 subcommunity 2.
Projections of the neurons found in the subcommunity. Colors are assigned based on soma location. Scale bar = 100 μm

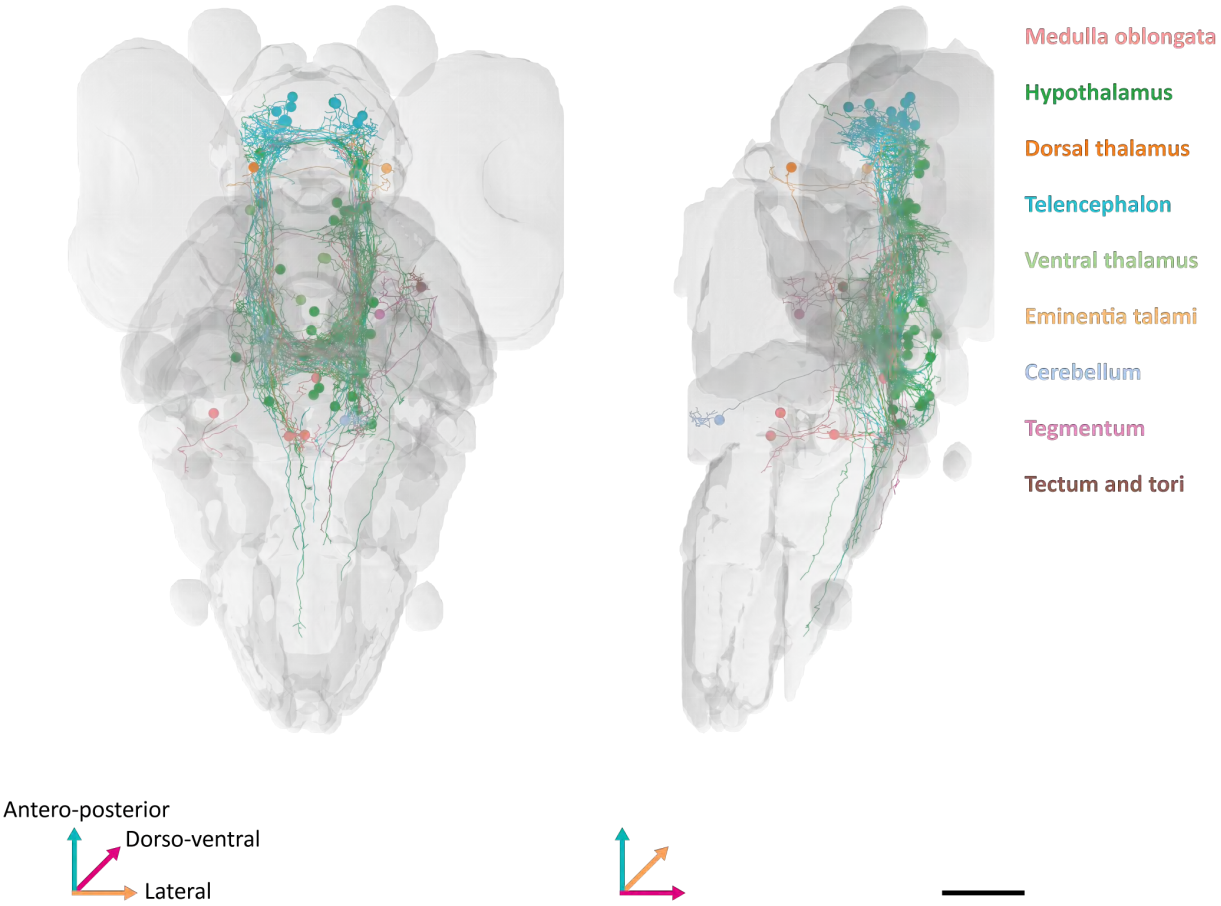

Figure 7.27: Community 5 subcommunity 3.
Projections of the neurons found in the subcommunity. Colors are assigned based on soma location. Scale bar = 100 μm

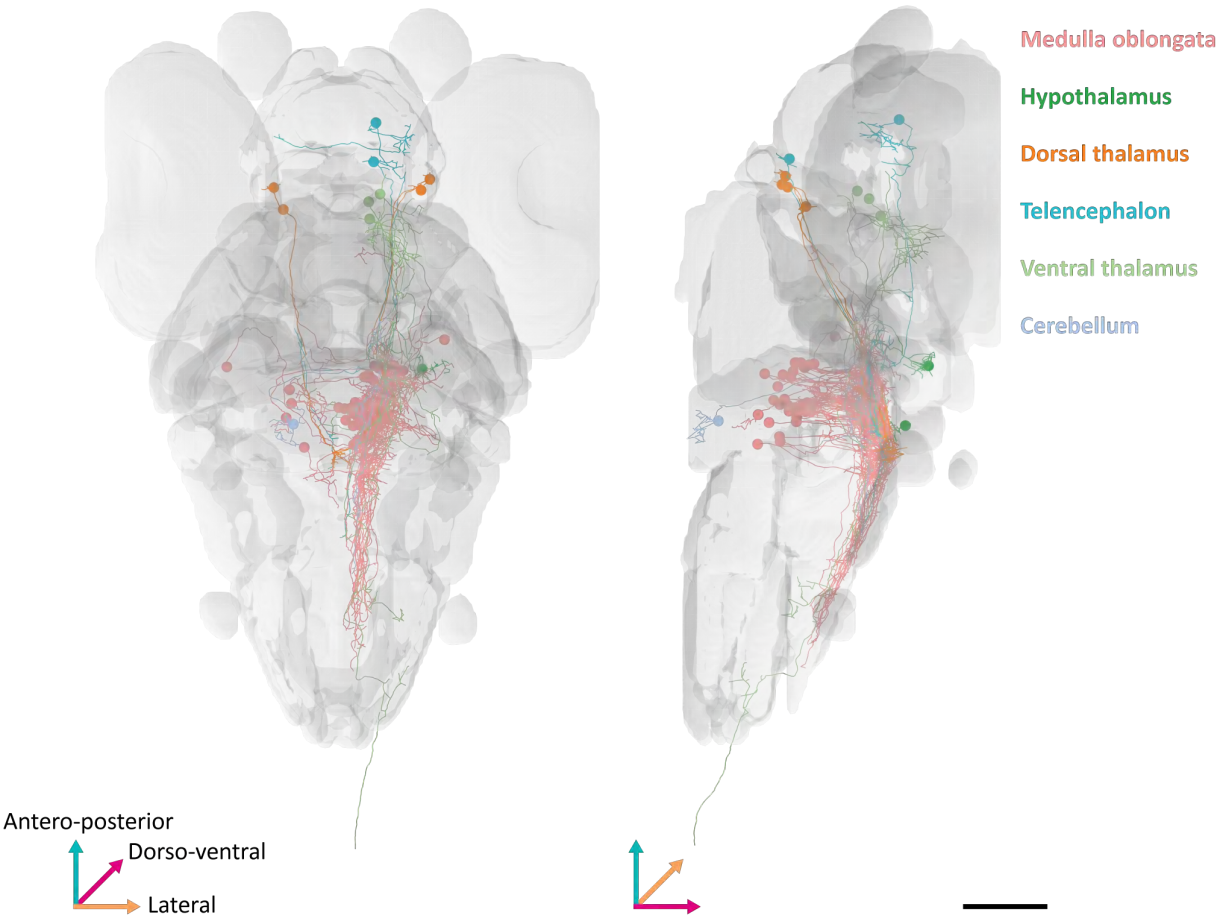

Figure 7.28: Community 5 subcommunity 4.
Projections of the neurons found in the subcommunity. Colors are assigned based on soma location. Scale bar = 100 μm

Figure 7.29: Community 5 subcommunity 5.
Projections of the neurons found in the subcommunity. Colors are assigned based on soma location. Scale bar = 100 μm

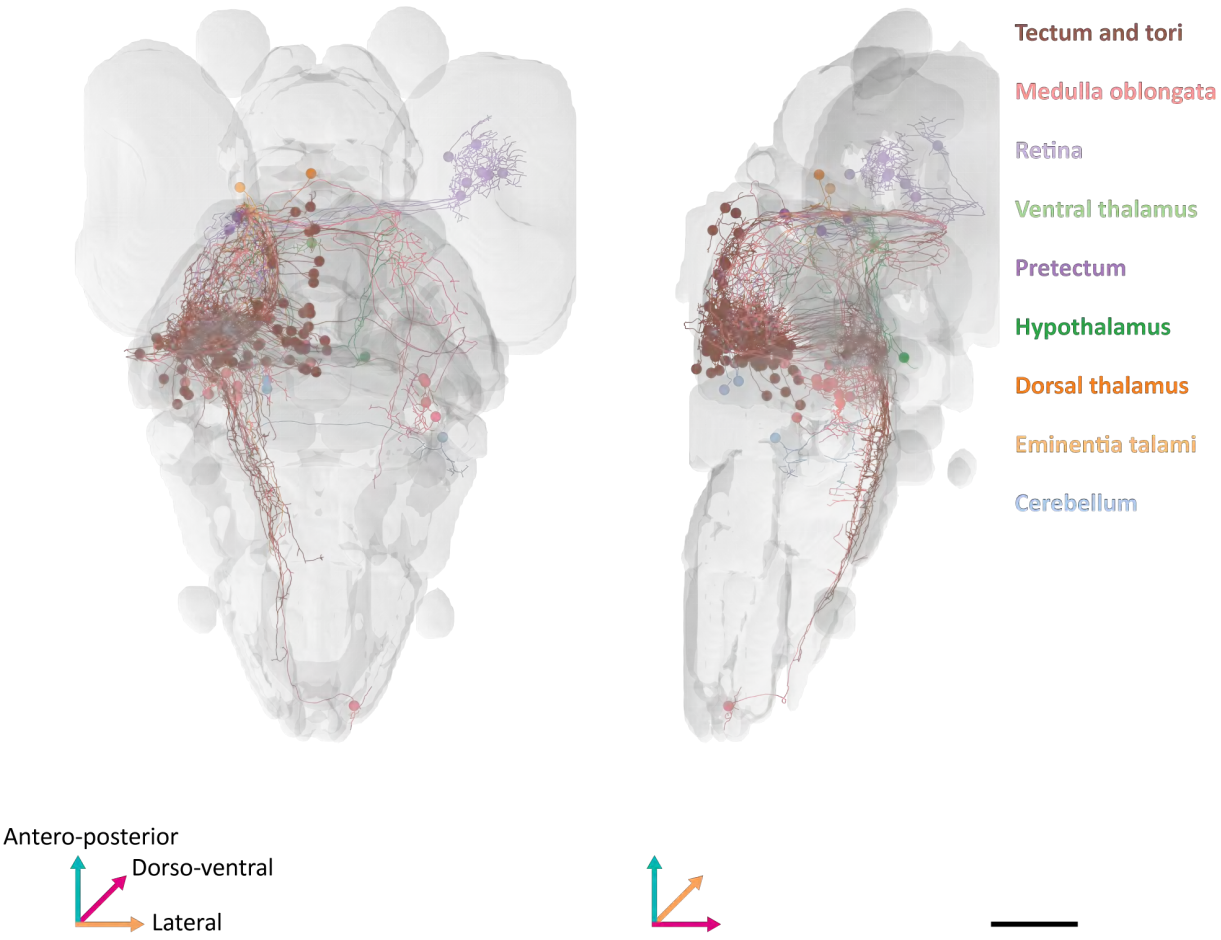

Figure 7.30: Community 6 subcommunity 1.
Projections of the neurons found in the subcommunity. Colors are assigned based on soma location. Scale bar = 100 μm

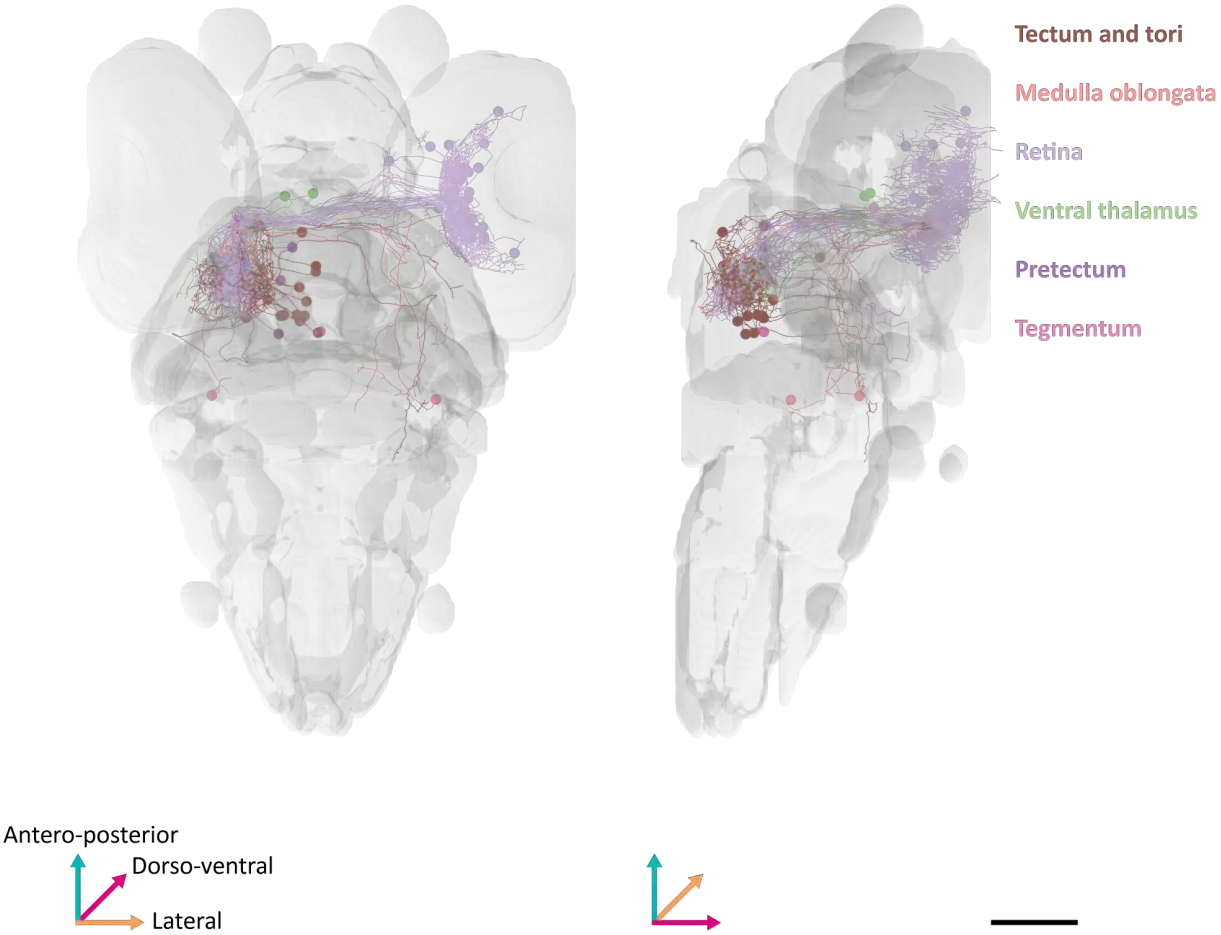

Figure 7.31: Community 6 subcommunity 2.
Projections of the neurons found in the subcommunity. Colors are assigned based on soma location. Scale bar = 100 μm

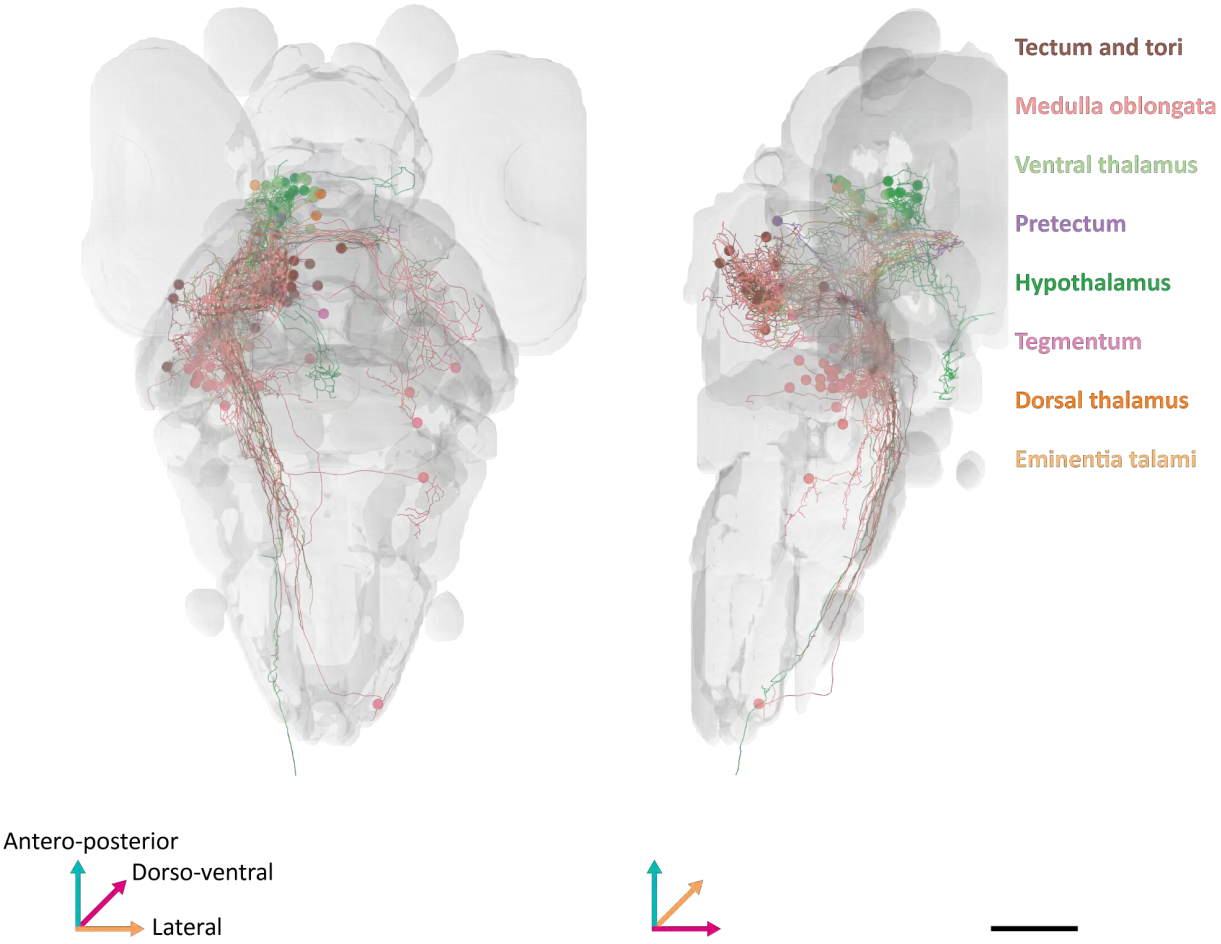

Figure 7.32: Community 6 subcommunity 3.
Projections of the neurons found in the subcommunity. Colors are assigned based on soma location. Scale bar = 100 μm

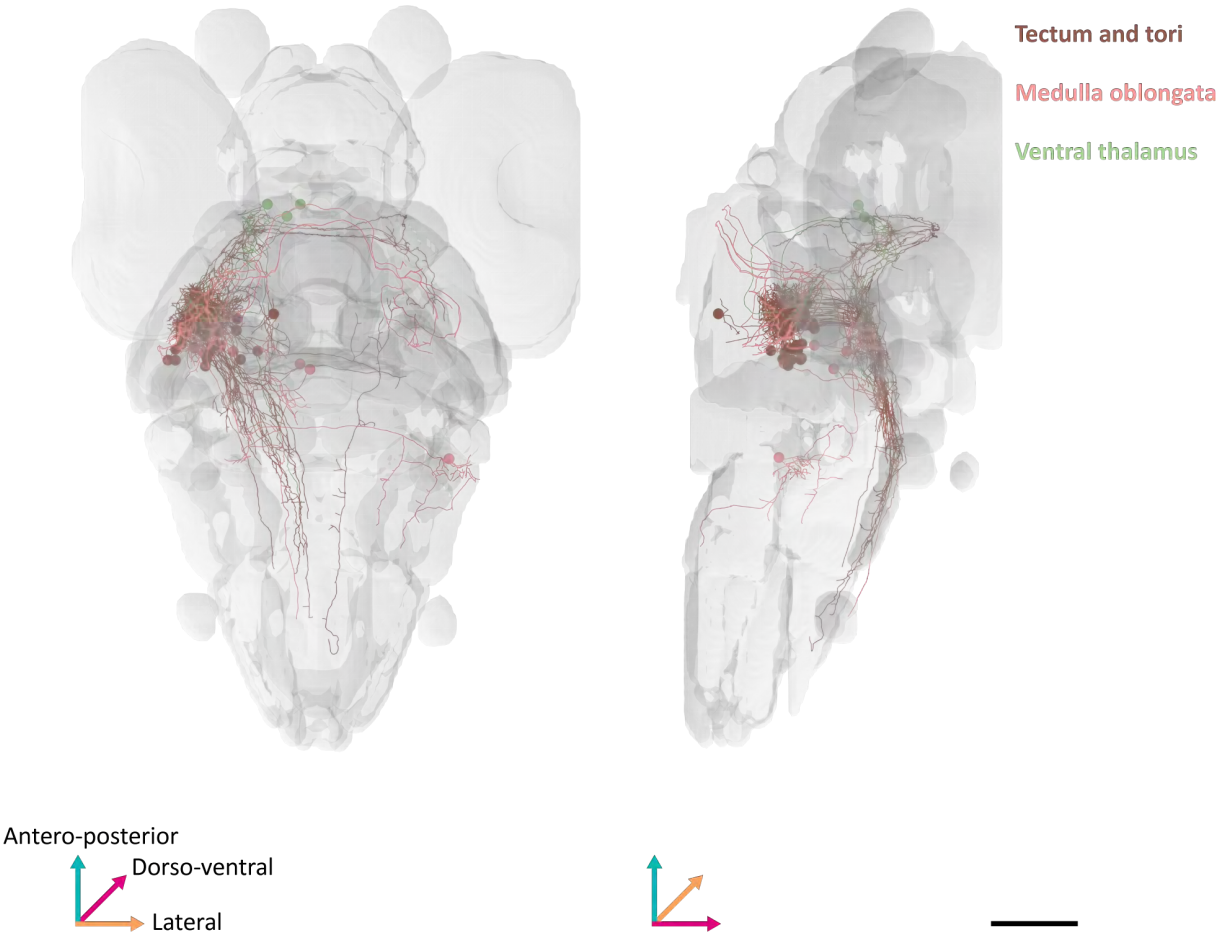

Figure 7.33: Community 6 subcommunity 4.
Projections of the neurons found in the subcommunity. Colors are assigned based on soma location. Scale bar = 100 μm

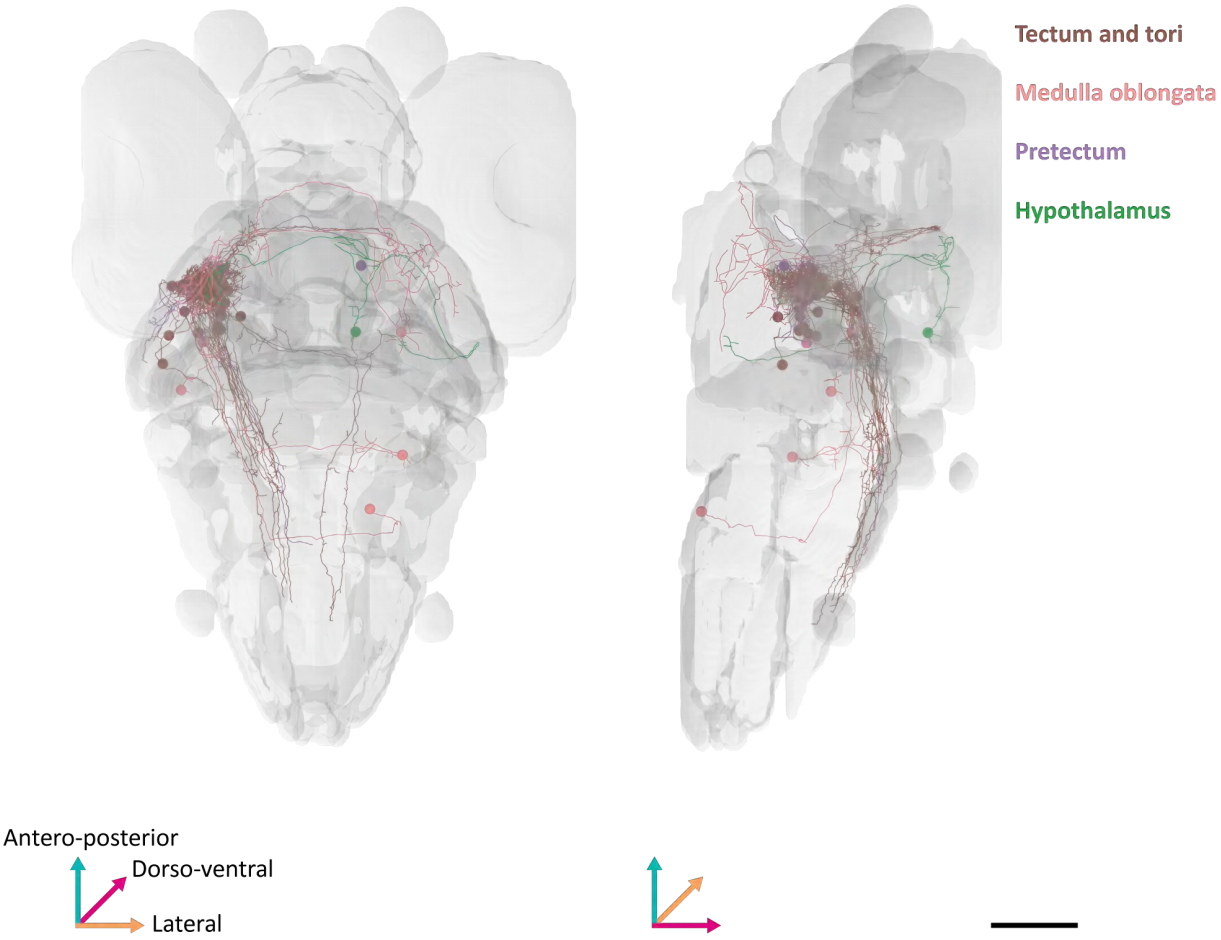

Figure 7.34: Community 6 subcommunity 5.
Projections of the neurons found in the subcommunity. Colors are assigned based on soma location. Scale bar = 100 μm

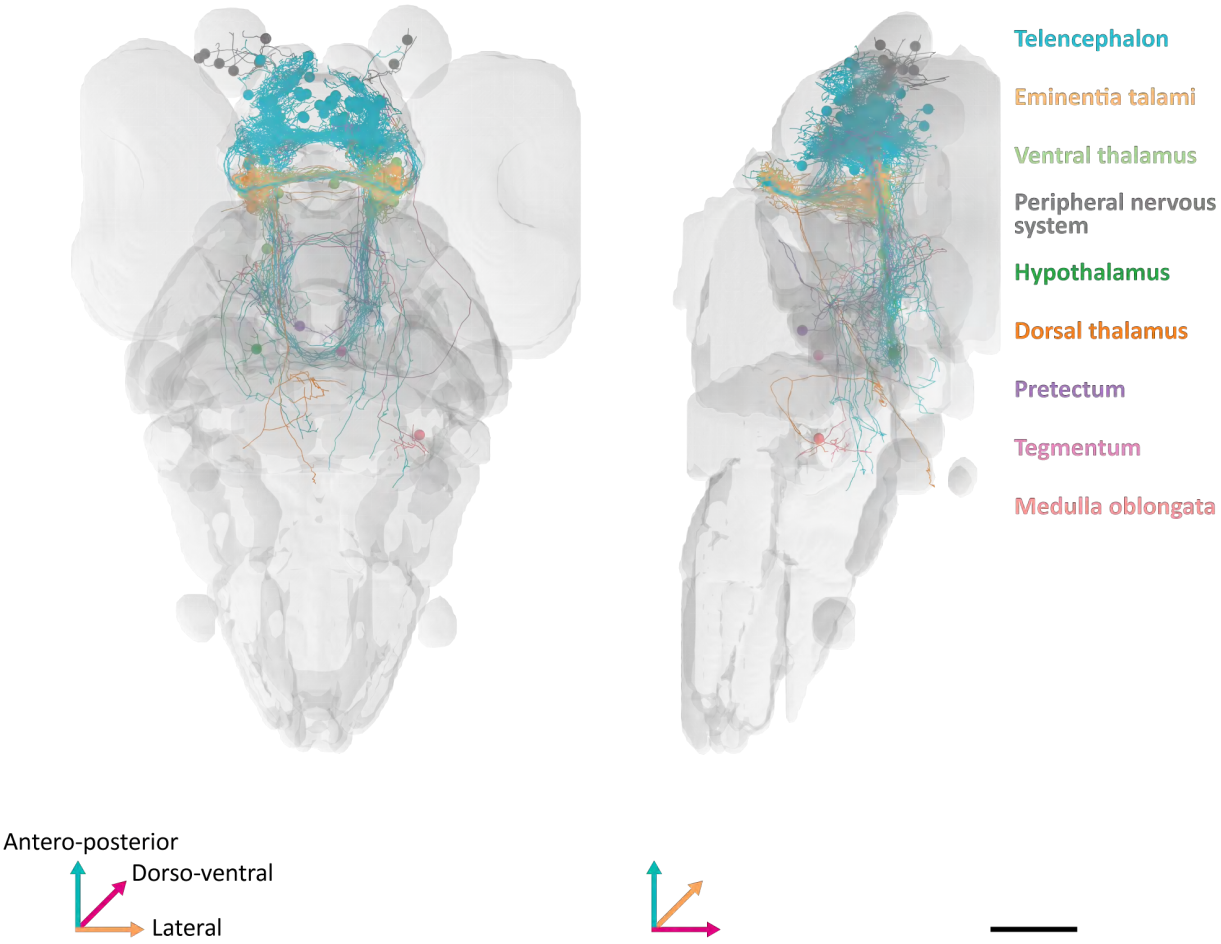

Figure 7.35: Community 7 subcommunity 1.
Projections of the neurons found in the subcommunity. Colors are assigned based on soma location. Scale bar = 100 μm

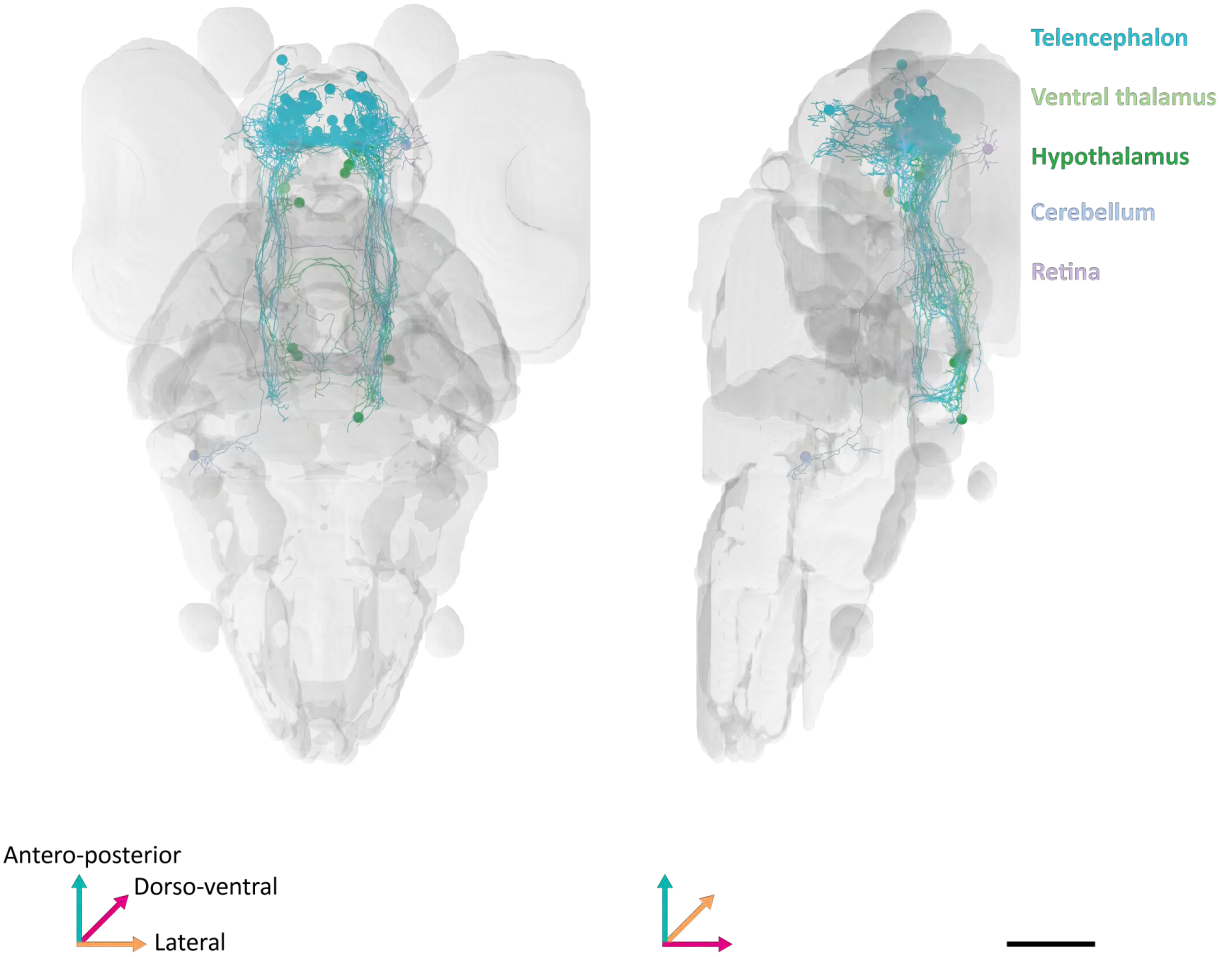

Figure 7.36: Community 7 subcommunity 2.
Projections of the neurons found in the subcommunity. Colors are assigned based on soma location. Scale bar = 100 μm

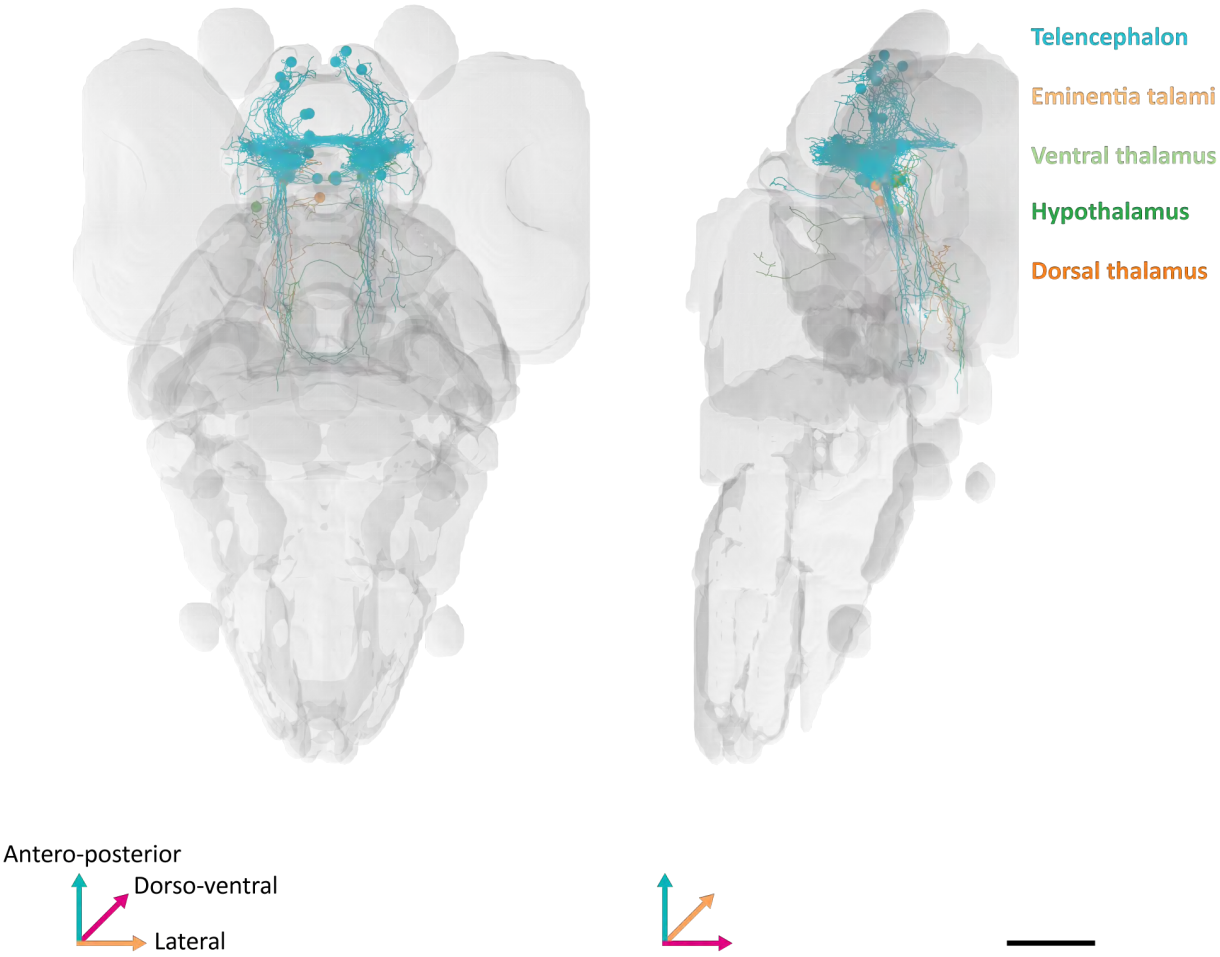

Figure 7.37: Community 7 subcommunity 3.
Projections of the neurons found in the subcommunity. Colors are assigned based on soma location. Scale bar = 100 μm

Figure 7.38: Community 7 subcommunity 4.
Projections of the neurons found in the subcommunity. Colors are assigned based on soma location. Scale bar = 100 μm

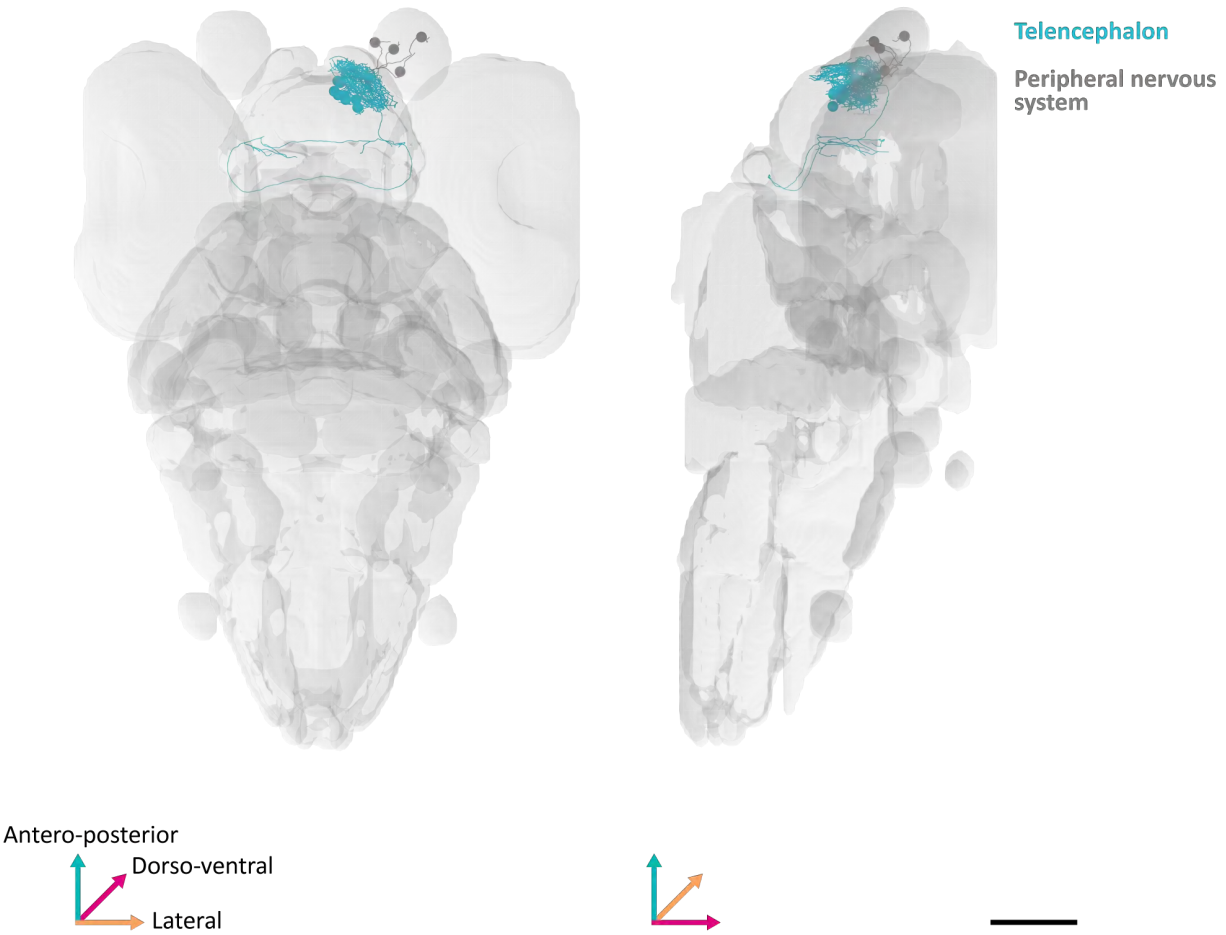

Figure 7.39: Community 7 subcommunity 5.
Projections of the neurons found in the subcommunity. Colors are assigned based on soma location. Scale bar = 100 μm

8 Publications

Publications produced during the PhD program.

10 - Research article - in preparation

A graph-based method for extracting the organization of brain-wide networks from connectome datasets

Understanding brain mechanisms is currently one of the open challenges. Despite a number of methods available, it is still limited the information one can retrieve about on how the organization of the wiring between the cells across the brain supporting the network ands the circuit activity. This appears as a general problem, even in the cases where the cell anatomy is well described and potentially accessible at scales down to synaptic level. To extend the tools currently available, here we present the application of a network analysis algorithm working on brain connectome data for uncovering the cell communities underlying brain-wide networks and reveal their intra- and inter-network organization. We first applied this approach on a Electron Microscopy (EM) dataset with connectome reconstructions from the hemibrain of an invertebrate model organism, Drosophila Melanogaster, identifying a number of characteristic networks and their organization. We then extended this approach on a "synthetic" connectome generated from a dataset of more than 3 thousand cell skeletonizations from the zebrafish larvae brain applying a simple cell-to-cell synaptic contact rule. Although lacking the actual synaptic information, this approach was capable to capture already described connectivity patterns and functional connection diagrams. In conclusion, we show the application of an analysis pipeline that is scalable and amenable for different type of dataset, independently from the particular anatomical reconstruction method adopted, to reveal the neuronal architectures supporting the brain mechanisms.

9 - Book chapter - in press expected March 2023

Vaczi, T., László, H., **Bruzzone, M.**, Miklós V., & Dal Maschio M., *Spectrally-Focused Stimulated Raman Scattering (sf-SRS) Microscopy for Label-free Investigations of Molecular Mechanisms in Living Organisms* - Neuromethods

Stimulated Raman Scattering (SRS) microscopy is a light-based non-linear imaging method for visualizing a molecule based on its chemical properties, i.e. the energy vibrational states reflecting the molecule structure and its environment. This technique, relying on the specificity of the molecule spectral fingerprint, enables label-free, high sensitivity and high-resolution 3D reconstruction of the distribution and the properties of a molecule within a tissue. Despite its tremendous potentials, the application of SRS is still not frequent in the field of life science, where it could be applied over an extremely broad investigation range, from the study of the molecule interactions at subcellular level to the characterization of tissue alterations in clinical studies. Trying to fill this gap, here, after describing the general principles of SRS, we present the materials and the methods to integrate spectrally-focused Stimulated Raman Spectroscopy

(sf-SRS) on commercial multiphoton microscopes and highlight the critical aspects to consider.

8 - Book chapter - in press expected March 2023

Bruzzone, M., Chiarello E., Maset A., Megighian A., Lodovichi C., Dal Maschio M., *Light-based neuronal circuit probing in living brains at high-resolution: constraints and layouts for integrating neuronal activity recording and modulation in three dimensions* - Neuromethods

Understanding how the brain orchestrates neuronal activity to finely produce and regulate behavior is an intriguing yet challenging task. In the last years, the progressive refinement of optical techniques and light-based molecular tools allowed to start addressing open questions in cellular and systems neuroscience with unprecedented resolution and specificity. Currently, all- optical experimental protocols for simultaneous recording of the activity of large cell populations with the concurrent modulation of the firing rate at cellular resolution represent an invaluable tool. In this scenario, it is becoming everyday more evident the importance of sampling and probing the circuit mechanisms not just in a single plane, but extending the exploration to the entire volume containing the involved circuit components. Here, we focus on the design principles and the hardware architectures of all-optical approaches allowing for studying the neuronal dynamics at cellular resolution across a volume of the brain.

7 - Research article

Anna Archetti, Matteo Bruzzone, Giulia Tagliabue & Dal Maschio M., *Generation of Bessel beam lattices by a single metasurface for recording neuronal activity in zebrafish larva* Bessel Beams (BBs) and BB lattices are structured-light excitation profiles that are frequently used in many optical methods, in particular in Light Sheet Microscopy (LSM) approaches. In LSM, BB-lattices offer higher acquisition rate, enhanced resolution and signal-to-noise ratio, while reducing the overall phototoxicity. However, this performance improvement typically comes at the cost of the layout complexity and constraints, originating from the optical elements required, like beam multiplexing devices for forming the lattice, and the phase or amplitude light modulation components for introducing Bessel features. Here, we present a novel method for integrating in a single flat element all the optical operations required to generate a BB lattice, including those of the excitation objective. Finally, replacing the original components along a LSM excitation path with the fabricated element, we demonstrated its actual performance and recorded the neuronal activity from the zebrafish larvae brain over a 200 x 700 x 7 µm3 region with cellular resolution. In perspective, this approach can revolutionize the LSM technique and, more in general, the BBs versatility and application scenarios.
DOI: 10.1101/2023.02.12.528189

6 - Review

Brondi, M., **Bruzzone, M.**, Lodovichi, C., Dal Maschio, M. (2022). *Optogenetic Methods to Investigate Brain Alterations in Preclinical Models*. Cells, 11(11), 1848.
DOI: 10.3390/cells11111848

Investigating the neuronal dynamics supporting brain functions and understanding how the alterations in these mechanisms result in pathological conditions represents a fundamental challenge. Preclinical research on model organisms allows for a multiscale and multiparametric analysis in vivo of the neuronal mechanisms and holds the potential for better linking the symptoms of a neurological disorder to the underlying cellular and circuit alterations, eventually leading to the identification of therapeutic/rescue strategies. In recent years, brain research in model organisms has taken advantage, along with other techniques, of the development and continuous refinement of methods that use light and optical approaches to reconstruct the activity of brain circuits at the cellular and system levels, and to probe the impact of the different neuronal components in the observed dynamics. These tools, combining low-invasiveness of optical approaches with the power of genetic engineering, are currently revolutionizing the way, the scale and the perspective of investigating brain diseases. The aim of this review is to describe how brain functions can be investigated with optical approaches currently available and to illustrate how these techniques have been adopted to study pathological alterations of brain physiology.

5 - Research article

Corradi, L., **Bruzzone, M.**, Dal Maschio, M., Sawamiphak, S., & Filosa, A. (2022). *Hypothalamic Galanin-producing neurons regulate stress in zebrafish through a peptidergic, self-inhibitory loop*. Current Biology, 32(7), 1497-1510.
DOI: 10.1016/j.cub.2022.02.011

Animals possess neuronal circuits inducing stress to avoid or cope with threats present in their surroundings, for instance, by promoting behaviors, such as avoidance and escape. However, mechanisms must exist to tightly control responses to stressors, since overactivation of stress circuits is deleterious for the wellbeing of an organism. The underlying neuronal dynamics responsible for controlling behavioral responses to stress have remained unclear. Here, we describe a neuronal circuit in the hypothalamus of zebrafish larvae that inhibits stress-related behaviors and prevents excessive activation of the neuroendocrine pathway hypothalamic-pituitary-interrenal axis. Central components of this circuit are neurons secreting the neuropeptide Galanin, as ablation of these neurons led to abnormally high levels of stress. Surprisingly, we found that Galanin has a self-inhibitory action on Galanin-producing neurons. Our results suggest that hypothalamic Galanin-producing neurons play an important role in fine-tuning stress responses by preventing potentially harmful overactivation of stress-regulating circuits.

4 - Research article

Gatto, E., Dadda, M., **Bruzzone, M.**, Chiarello, E., De Russi, G., Maschio, M. D., ... & Lucon-Xiccato, T. (2022). *Environmental enrichment decreases anxiety-like behavior in zebrafish larvae*. Developmental Psychobiology, 64(3), e22255.

DOI: 10.1002/dev.22255

The development of anxiety disorders is often linked to individuals' negative experience. In many animals, development of anxiety-like behavior is modeled by manipulating individuals' exposure to environmental enrichment. We investigated whether environmental enrichment during early ontogenesis affects anxiety-like behavior in larval zebrafish. Larvae were exposed from hatching to either an environment enriched with 3D-objects of different color and shape or to a barren environment. Behavioral testing was conducted at different intervals during development (7, 14, and 21 days post-fertilization, dpf). In a novel object exploration test, 7 dpf larvae of the two treatments displayed similar avoidance of the visual stimulus. However, at 14 and 21 dpf, larvae of the enriched environment showed less avoidance, indicating lower anxiety response. Likewise, larvae of the two treatments demonstrated comparable avoidance of a novel odor stimulus at 7 dpf, with a progressive reduction of anxiety behavior in the enriched treatment with development. In a control experiment, larvae treated before 7 dpf but tested at 14 dpf showed the effect of enrichment on anxiety, suggesting an early determination of the anxiety phenotype. This study confirms a general alteration of zebrafish anxiety-like behavior due to a short enrichment period in first days of life.

3 - Research article

Gatto, E., **Bruzzone, M.**, Dal Maschio, M., & Dadda, M. (2022). *Effects of environmental enrichment on recognition memory in zebrafish larvae*. Applied Animal Behaviour Science, 247, 105552.
DOI: 10.1016/j.applanim.2022.105552

Zebrafish (Danio rerio) constitute a useful model for studying memory function and impairment in vertebrates and are now widely used in translational research. On the one hand, the adoption of simple, fast and reliable tests such as novel object recognition (NOR) has increased our knowledge considerable about memory mechanisms in animals. On the other hand, in many model organisms, exposure to environmental enrichment, especially during the early stages of development, affects various cognitive functions. Evidence for the effects of environmental enrichment on zebrafish has been accumulating rapidly, but most of this evidence has been collected in adult subjects. We compared larvae raised in either an enriched or barren environments and measured their memory performance at 14-days post-fertilization. Initially, subjects were allowed to familiarize with two identical novel objects (i.e., pattern of 2D-geometrical figures). After a time interval, larvae faced a two-choice task presenting the same objects paired with a new one. As a measure of recognition memory, we exploit the tendency of individuals to explore a novel object over a familiar one. Our results indicate that larvae from the barren environment spent more time exploring familiar stimuli than novel ones, showing the innate presence of recognition memory capacity in zebrafish larvae. Conversely, subjects bred in a visually enriched environment explore both familiar and novel stimuli almost equally. The increase of exploratory behavior and, consequently, the reduction of avoidance to the novel object may explain the performance shown by larvae exposed to an enrichment

environment compared to the larvae bred in a barren environment. Taken together, these results confirm that early-stage zebrafish possess complex visual discrimination capacities and that rearing subjects in a structurally complex environment might hinder memory performance by reducing their neophobic response.

2 - Research article

Gatto, E., **Bruzzone, M.**, & Lucon-Xiccato, T. (2021). Innate visual discrimination abilities of zebrafish larvae. Behavioural Processes, 193, 104534.
DOI: 10.1016/j.beproc.2021.104534

The ability to discriminate between objects visually plays a key role in animals' interactions with their environment because it enables them to recognise companions, prey, and predators. In the zebrafish, Danio rerio, hatching occurs early on during development (48–72 h post fertilisation), and the larvae must forage and evade predators despite their immature sensory and cognitive systems. Using a preference paradigm, we investigated whether larval zebrafish are nonetheless capable of discriminating between visual stimuli. We found that larvae discriminated not only between figures with different colours or different shapes, but also between two identical figures with different orientations and between sets of figures with different numerosities. By manipulating larvae's exposure to objects before the test, we demonstrated that their discrimination abilities are innate and do not depend upon experience. This study highlighted that zebrafish possess relatively sophisticated visual discrimination abilities even at the larval stage. These abilities likely improve larval survival via the recognition of biologically relevant stimuli.

1 - Research article

Bruzzone, M., Chiarello, E., Albanesi, M., Miletto Petrazzini, M. E., Megighian, A., Lodovichi, C., & Dal Maschio, M. (2021). Whole brain functional recordings at cellular resolution in zebrafish larvae with 3D scanning multiphoton microscopy. Scientific reports, 11(1), 1-11.
DOI: 10.1038/s41598-021-90335-y

Optical recordings of neuronal activity at cellular resolution represent an invaluable tool to investigate brain mechanisms. Zebrafish larvae is one of the few model organisms where, using fluorescence-based reporters of the cell activity, it is possible to optically reconstruct the neuronal dynamics across the whole brain. Typically, leveraging the reduced light scattering, methods like lightsheet, structured illumination, and light-field microscopy use spatially extended excitation profiles to detect in parallel activity signals from multiple cells. Here, we present an alternative design for whole brain imaging based on sequential 3D point-scanning excitation. Our approach relies on a multiphoton microscope integrating an electrically tunable lens. We first apply our approach, adopting the GCaMP6s activity reporter, to detect functional responses from retinal ganglion cells (RGC) arborization fields at different depths within the zebrafish larva midbrain. Then, in larvae expressing a nuclear localized GCaMP6s, we recorded

whole brain activity with cellular resolution. Adopting a semi-automatic cell segmentation, this allowed reconstructing the activity from up to 52,000 individual neurons across the brain. In conclusion, this design can easily retrofit existing imaging systems and represents a compact, versatile and reliable tool to investigate neuronal activity across the larva brain at high resolution.

Bibliography

[1] De No Lorente. 'Vestibulo-ocular reflex arc'. In: *Arch Neurol Psychiat* 30 (1933), pp. 245–291 (cited on page 1).

[2] Rafael Yuste. 'From the neuron doctrine to neural networks'. In: *Nature Reviews Neuroscience* 16.8 (Aug. 2015). Number: 8 Publisher: Nature Publishing Group, pp. 487–497. DOI: 10.1038/nrn3962 (cited on page 1).

[3] Miguel A.L Nicolelis, Erika E Fanselow, and Asif A Ghazanfar. 'Hebb's Dream: The Resurgence of Cell Assemblies'. In: *Neuron* 19.2 (Aug. 1997), pp. 219–221. DOI: 10.1016/S0896-6273(00)80932-0 (cited on page 1).

[4] D. O. Hebb. *The organization of behavior: A neuropsychological theory*. Vol. 34. 1949 (cited on page 1).

[5] Jason W. Bohland et al. 'A Proposal for a Coordinated Effort for the Determination of Brainwide Neuroanatomical Connectivity in Model Organisms at a Mesoscopic Scale'. In: *PLOS Computational Biology* 5.3 (Mar. 27, 2009). Publisher: Public Library of Science, e1000334. DOI: 10.1371/journal.pcbi.1000334 (cited on page 2).

[6] Hongkui Zeng. 'Mesoscale connectomics'. In: *Current Opinion in Neurobiology*. Neurotechnologies 50 (June 1, 2018), pp. 154–162. DOI: 10.1016/j.conb.2018.03.003 (cited on pages 2, 3).

[7] Michael N. Economo et al. 'Distinct descending motor cortex pathways and their roles in movement'. In: *Nature* 563.7729 (Nov. 2018). Number: 7729 Publisher: Nature Publishing Group, pp. 79–84. DOI: 10.1038/s41586-018-0642-9 (cited on page 2).

[8] Osung Kwon et al. 'Schaffer Collateral Inputs to CA1 Excitatory and Inhibitory Neurons Follow Different Connectivity Rules'. In: *The Journal of Neuroscience* 38.22 (May 30, 2018), pp. 5140–5152. DOI: 10.1523/JNEUROSCI.0155-18.2018 (cited on page 2).

[9] Yunyun Han et al. 'The logic of single-cell projections from visual cortex'. In: *Nature* 556.7699 (Apr. 2018). Number: 7699 Publisher: Nature Publishing Group, pp. 51–56. DOI: 10.1038/nature26159 (cited on page 2).

[10] Bryan M. Hooks et al. 'Topographic precision in sensory and motor corticostriatal projections varies across cell type and cortical area'. In: *Nature Communications* 9.1 (Sept. 3, 2018). Number: 1 Publisher: Nature Publishing Group, p. 3549. DOI: 10.1038/s41467-018-05780-7 (cited on page 2).

[11] Johan Winnubst et al. 'Reconstruction of 1,000 Projection Neurons Reveals New Cell Types and Organization of Long-Range Connectivity in the Mouse Brain'. In: *Cell* 179.1 (Sept. 19, 2019), 268–281.e13. DOI: 10.1016/j.cell.2019.07.042 (cited on page 2).

[12] Marcia G. Honig and Richard I. Hume. 'Dil and DiO: versatile fluorescent dyes for neuronal labelling and pathway tracing'. In: *Trends in Neurosciences* 12.9 (Jan. 1, 1989), pp. 333–341. DOI: 10.1016/0166-2236(89)90040-4 (cited on page 2).

[13] Elke Rink and Mario F. Wullimann. 'The teleostean (zebrafish) dopaminergic system ascending to the subpallium (striatum) is located in the basal diencephalon (posterior tuberculum)'. In: *Brain Research* 889.1 (Jan. 19, 2001), pp. 316–330. DOI: 10.1016/S0006-8993(00)03174-7 (cited on page 2).

[14] Elke Rink and Mario F Wullimann. 'Development of the catecholaminergic system in the early zebrafish brain: an immunohistochemical study'. In: *Developmental Brain Research* 137.1 (July 30, 2002), pp. 89–100. DOI: 10.1016/S0165-3806(02)00354-1 (cited on page 2).

[15] Elke Rink and Mario F Wullimann. 'Connections of the ventral telencephalon and tyrosine hydroxylase distribution in the zebrafish brain (Danio rerio) lead to identification of an ascending dopaminergic system in a teleost'. In: *Brain Research Bulletin* 57.3 (Feb. 1, 2002), pp. 385–387. DOI: 10.1016/S0361-9230(01)00696-7 (cited on page 2).

[16] Elke Rink and Mario F Wullimann. 'Connections of the ventral telencephalon (subpallium) in the zebrafish (Danio rerio)'. In: *Brain Research* 1011.2 (June 18, 2004), pp. 206–220. DOI: 10.1016/j.brainres.2004.03.027 (cited on page 2).

[17] Michiyo Kinoshita and Finlay J. Stewart. 'Cortical-like colour-encoding neurons in the mushroom body of a butterfly'. In: *Current Biology* 32.3 (Feb. 7, 2022), R114–R115. DOI: 10.1016/j.cub.2021.12.032 (cited on page 2).

[18] Jonathan J. Nassi et al. 'Neuroanatomy goes viral!' In: *Frontiers in Neuroanatomy* 9 (2015). DOI: 10.3389/fnana.2015.00080 (cited on page 3).

[19] Kristin M Scaplen et al. 'Transsynaptic mapping of Drosophila mushroom body output neurons'. In: *eLife* 10 (Feb. 11, 2021). Ed. by K VijayRaghavan and Nicholas Strausfeld. Publisher: eLife Sciences Publications, Ltd, e63379. DOI: 10.7554/eLife.63379 (cited on page 3).

[20] Harold K. Shearin et al. 't-GRASP, a targeted GRASP for assessing neuronal connectivity'. In: *Journal of neuroscience methods* 306 (Aug. 1, 2018), pp. 94–102. DOI: 10.1016/j.jneumeth.2018.05.014 (cited on page 3).

[21] Lindsay A. Schwarz et al. 'Viral-genetic tracing of the input–output organization of a central noradrenaline circuit'. In: *Nature* 524.7563 (Aug. 2015). Number: 7563 Publisher: Nature Publishing Group, pp. 88–92. DOI: 10.1038/nature14600 (cited on page 3).

[22] Barbara J. Hunnicutt et al. 'A comprehensive thalamocortical projection map at the mesoscopic level'. In: *Nature Neuroscience* 17.9 (Sept. 2014). Number: 9 Publisher: Nature Publishing Group, pp. 1276–1285. DOI: 10.1038/nn.3780 (cited on page 3).

[23] Seung Wook Oh et al. 'A mesoscale connectome of the mouse brain'. In: *Nature* 508.7495 (Apr. 2014). Number: 7495 Publisher: Nature Publishing Group, pp. 207–214. DOI: 10.1038/nature13186 (cited on pages 3, 12).

[24] Shenqin Yao et al. 'A whole-brain monosynaptic input connectome to neuron classes in mouse visual cortex'. In: *Nature Neuroscience* (Dec. 22, 2022). Publisher: Nature Publishing Group, pp. 1–15. DOI: 10.1038/s41593-022-01219-x (cited on page 3).

[25] Ethan K. Scott et al. 'Targeting neural circuitry in zebrafish using GAL4 enhancer trapping'. In: *Nature Methods* 4.4 (Apr. 2007). Number: 4 Publisher: Nature Publishing Group, pp. 323–326. DOI: 10.1038/nmeth1033 (cited on page 3).

[26] Ann-Shyn Chiang et al. 'Three-Dimensional Reconstruction of Brain-wide Wiring Networks in Drosophila at Single-Cell Resolution'. In: *Current Biology* 21.1 (Jan. 11, 2011), pp. 1–11. DOI: 10.1016/j.cub.2010.11.056 (cited on page 3).

[27] Michael Kunst et al. 'A Cellular-Resolution Atlas of the Larval Zebrafish Brain'. In: *Neuron* 103.1 (July 3, 2019). Publisher: Elsevier, 21–38.e5. DOI: 10.1016/j.neuron.2019.04.034 (cited on pages 3, 12, 13, 15, 24, 25, 39, 46, 47, 52, 53, 68, 69).

[28] Partha P. Mitra. 'The Circuit Architecture of Whole Brains at the Mesoscopic Scale'. In: *Neuron* 83.6 (Sept. 17, 2014), pp. 1273–1283. DOI: 10.1016/j.neuron.2014.08.055 (cited on page 3).

[29] Fabian Svara et al. 'Automated synapse-level reconstruction of neural circuits in the larval zebrafish brain'. In: *Nature Methods* 19.11 (Nov. 2022). Number: 11 Publisher: Nature Publishing Group, pp. 1357–1366. DOI: 10.1038/s41592-022-01621-0 (cited on pages 3–5, 39, 78).

[30] Donna G. Albertson, J. N. Thompson, and Sydney Brenner. 'The pharynx of Caenorhabditis elegans'. In: *Philosophical Transactions of the Royal Society of London. B, Biological Sciences* 275.938 (Aug. 10, 1976). Publisher: Royal Society, pp. 299–325. DOI: 10.1098/rstb.1976.0085 (cited on page 3).

[31] J. G. White et al. 'The structure of the nervous system of the nematode Caenorhabditis elegans'. In: *Philosophical Transactions of the Royal Society of London. Series B, Biological Sciences* 314.1165 (Nov. 12, 1986), pp. 1–340. DOI: 10.1098/rstb.1986.0056 (cited on pages 3, 5).

[32] Winfried Denk and Heinz Horstmann. 'Serial block-face scanning electron microscopy to reconstruct three-dimensional tissue nanostructure'. In: *PLoS biology* 2.11 (Nov. 2004), e329. DOI: 10.1371/journal.pbio.0020329 (cited on page 3).

[33] Jurgen A. W. Heymann et al. 'Site-specific 3D imaging of cells and tissues with a dual beam microscope'. In: *Journal of Structural Biology* 155.1 (July 2006), pp. 63–73. DOI: 10.1016/j.jsb.2006.03.006 (cited on page 3).

[34] Albert Cardona et al. 'An integrated micro- and macroarchitectural analysis of the Drosophila brain by computer-assisted serial section electron microscopy'. In: *PLoS biology* 8.10 (Oct. 5, 2010), e1000502. DOI: 10.1371/journal.pbio.1000502 (cited on page 3).

[35] Albert Cardona et al. 'TrakEM2 software for neural circuit reconstruction'. In: *PloS One* 7.6 (2012), e38011. DOI: 10.1371/journal.pone.0038011 (cited on page 3).

[36] Jörgen Kornfeld and Winfried Denk. 'Progress and remaining challenges in high-throughput volume electron microscopy'. In: *Current Opinion in Neurobiology*. Neurotechnologies 50 (June 1, 2018), pp. 261–267. DOI: 10.1016/j.conb.2018.04.030 (cited on page 3).

[37] Kerrianne Ryan, Zhiyuan Lu, and Ian A Meinertzhagen. 'The CNS connectome of a tadpole larva of Ciona intestinalis (L.) highlights sidedness in the brain of a chordate sibling'. In: *eLife* 5 (Dec. 6, 2016). Ed. by Eve Marder. Publisher: eLife Sciences Publications, Ltd, e16962. DOI: 10.7554/eLife.16962 (cited on page 3).

[38] Nadine Randel et al. 'Neuronal connectome of a sensory-motor circuit for visual navigation'. In: *eLife* 3 (May 27, 2014). Ed. by Eve Marder. Publisher: eLife Sciences Publications, Ltd, e02730. DOI: 10.7554/eLife.02730 (cited on page 3).

[39] Tomoko Ohyama et al. 'A multilevel multimodal circuit enhances action selection in Drosophila'. In: *Nature* 520.7549 (Apr. 30, 2015), pp. 633–639. DOI: 10.1038/nature14297 (cited on pages 3–5).

[40] Fushiki A et al. 'A circuit mechanism for the propagation of waves of muscle contraction in Drosophila'. In: *eLife* 5 (Feb. 15, 2016). Publisher: Elife. DOI: 10.7554/eLife.13253 (cited on page 3).

[41] Larderet I et al. 'Organization of the Drosophila larval visual circuit'. In: *eLife* 6 (Aug. 8, 2017). Publisher: Elife. DOI: 10.7554/eLife.28387 (cited on page 3).

[42] Katharina Eichler et al. 'The complete connectome of a learning and memory centre in an insect brain'. In: *Nature* 548.7666 (Aug. 9, 2017), pp. 175–182. DOI: 10.1038/nature23455 (cited on pages 3, 4).

[43] Shin-ya Takemura et al. 'The comprehensive connectome of a neural substrate for 'ON' motion detection in Drosophila'. In: *eLife* 6 (Apr. 22, 2017). Ed. by Alexander Borst. Publisher: eLife Sciences Publications, Ltd, e24394. DOI: 10.7554/eLife.24394 (cited on page 3).

[44] Mai M Morimoto et al. 'Spatial readout of visual looming in the central brain of Drosophila'. In: *eLife* 9 (Nov. 18, 2020). Ed. by Claude Desplan, Ronald L Calabrese, and Markus Meister. Publisher: eLife Sciences Publications, Ltd, e57685. DOI: 10.7554/eLife.57685 (cited on page 3).

[45] Adrian A. Wanner et al. 'Dense EM-based reconstruction of the interglomerular projectome in the zebrafish olfactory bulb'. In: *Nature Neuroscience* 19.6 (June 2016). Number: 6 Publisher: Nature Publishing Group, pp. 816–825. DOI: 10.1038/nn.4290 (cited on pages 3, 5).

[46] Sven Dorkenwald et al. 'Automated synaptic connectivity inference for volume electron microscopy'. In: *Nature Methods* 14.4 (Apr. 2017). Number: 4 Publisher: Nature Publishing Group, pp. 435–442. DOI: 10.1038/nmeth.4206 (cited on pages 3–5).

[47] Davi D. Bock et al. 'Network anatomy and in vivo physiology of visual cortical neurons'. In: *Nature* 471.7337 (Mar. 2011), pp. 177–182. DOI: 10.1038/nature09802 (cited on pages 3, 5).

[48] Narayanan Kasthuri et al. 'Saturated Reconstruction of a Volume of Neocortex'. In: *Cell* 162.3 (July 30, 2015), pp. 648–661. DOI: 10.1016/j.cell.2015.06.054 (cited on page 3).

[49] Wei-Chung Allen Lee et al. 'Anatomy and function of an excitatory network in the visual cortex'. In: *Nature* 532.7599 (Apr. 21, 2016), pp. 370–374. DOI: 10.1038/nature17192 (cited on page 3).

[50] MICrONS Consortium et al. *Functional connectomics spanning multiple areas of mouse visual cortex*. Section: New Results Type: article. bioRxiv, Aug. 9, 2021, p. 2021.07.28.454025. DOI: 10.1101/2021.07.28.454025 (cited on pages 3, 5).

[51] Daniel J. Bumbarger et al. 'System-wide Rewiring Underlies Behavioral Differences in Predatory and Bacterial-Feeding Nematodes'. In: *Cell* 152.1 (Jan. 17, 2013), pp. 109–119. DOI: 10.1016/j.cell.2012.12.013 (cited on pages 4, 14).

[52] Zhihao Zheng et al. 'A Complete Electron Microscopy Volume of the Brain of Adult Drosophila melanogaster'. In: *Cell* 174.3 (July 26, 2018), 730–743.e22. DOI: 10.1016/j.cell.2018.06.019 (cited on pages 4, 5).

[53] Louis K Scheffer et al. 'A connectome and analysis of the adult Drosophila central brain'. In: *eLife* 9 (Sept. 3, 2020). Ed. by Eve Marder et al. Publisher: eLife Sciences Publications, Ltd, e57443. DOI: 10.7554/eLife.57443 (cited on pages 4, 5, 23).

[54] Philipp J. Schubert et al. 'Learning cellular morphology with neural networks'. In: *Nature Communications* 10.1 (June 21, 2019), p. 2736. DOI: 10.1038/s41467-019-10836-3 (cited on page 4).

[55] Sven Dorkenwald et al. 'FlyWire: online community for whole-brain connectomics'. In: *Nature Methods* 19.1 (Jan. 2022). Number: 1 Publisher: Nature Publishing Group, pp. 119–128. DOI: 10.1038/s41592-021-01330-0. (Visited on 01/03/2023) (cited on page 4).

[56] Philipp J. Schubert et al. 'SyConn2: dense synaptic connectivity inference for volume electron microscopy'. In: *Nature Methods* 19.11 (Nov. 2022). Number: 11 Publisher: Nature Publishing Group, pp. 1367–1370. DOI: 10.1038/s41592-022-01624-x (cited on pages 4, 5, 77).

[57] Steven J. Cook et al. 'Whole-animal connectomes of both Caenorhabditis elegans sexes'. In: *Nature* 571.7763 (July 2019). Number: 7763 Publisher: Nature Publishing Group, pp. 63–71. DOI: 10.1038/s41586-019-1352-7 (cited on pages 4, 5).

[58] Michael Winding et al. *The connectome of an insect brain*. Pages: 2022.11.28.516756 Section: New Results. Nov. 28, 2022. DOI: 10.1101/2022.11.28.516756. URL: https://www.biorxiv.org/content/10.1101/2022.11.28.516756v1 (cited on pages 4, 5, 26, 76).

[59] Paul Brooks, Andrew Champion, and Marta Costa. 'Mapping of the zebrafish brain takes shape'. In: *Nature Methods* 19.11 (Nov. 2022). Number: 11 Publisher: Nature Publishing Group, pp. 1345–1346. DOI: 10.1038/s41592-022-01637-6 (cited on page 5).

[60] Karl J. Friston. 'Functional and Effective Connectivity: A Review'. In: *Brain Connectivity* 1.1 (Jan. 2011), pp. 13–36. DOI: 10.1089/brain.2011.0008 (cited on page 5).

[61] Michael N. Shadlen and William T. Newsome. 'The Variable Discharge of Cortical Neurons: Implications for Connectivity, Computation, and Information Coding'. In: *Journal of Neuroscience* 18.10 (May 15, 1998). Publisher: Society for Neuroscience Section: ARTICLE, pp. 3870–3896. DOI: 10.1523/JNEUROSCI.18-10-03870.1998 (cited on page 5).

[62] Ian H. Stevenson et al. 'Inferring functional connections between neurons'. In: *Current opinion in neurobiology* 18.6 (Dec. 2008), pp. 582–588. DOI: 10.1016/j.conb.2008.11.005 (cited on page 5).

[63] Erica Warp et al. 'Emergence of Patterned Activity in the Developing Zebrafish Spinal Cord'. In: *Current Biology* 22.2 (Jan. 24, 2012), pp. 93–102. DOI: 10.1016/j.cub.2011.12.002 (cited on page 5).

[64] Olaf Sporns. 'Structure and function of complex brain networks'. In: *Dialogues in Clinical Neuroscience* 15.3 (Sept. 30, 2013), pp. 247–262. DOI: 10.31887/DCNS.2013.15.3/osporns (cited on page 5).

[65] Tyler Davis and Russell A. Poldrack. 'Quantifying the Internal Structure of Categories Using a Neural Typicality Measure'. In: *Cerebral Cortex* 24.7 (July 1, 2014), pp. 1720–1737. DOI: 10.1093/cercor/bht014 (cited on page 5).

[66] Parinaz Babaeeghazvini et al. 'Brain Structural and Functional Connectivity: A Review of Combined Works of Diffusion Magnetic Resonance Imaging and Electro-Encephalography'. In: *Frontiers in Human Neuroscience* 15 (2021) (cited on pages 5, 6).

[67] A. M. Aertsen et al. 'Dynamics of neuronal firing correlation: modulation of "effective connectivity"'. In: *Journal of Neurophysiology* 61.5 (May 1989). Publisher: American Physiological Society, pp. 900–917. DOI: 10.1152/jn.1989.61.5.900 (cited on page 5).

[68] Barry Horwitz. 'The elusive concept of brain connectivity'. In: *NeuroImage* 19.2 (June 1, 2003), pp. 466–470. DOI: 10.1016/S1053-8119(03)00112-5 (cited on page 5).

[69] Volker Pernice et al. 'How Structure Determines Correlations in Neuronal Networks'. In: *PLOS Computational Biology* 7.5 (May 19, 2011). Publisher: Public Library of Science, e1002059. DOI: 10.1371/journal.pcbi.1002059 (cited on page 5).

[70] Lief Fenno, Ofer Yizhar, and Karl Deisseroth. 'The Development and Application of Optogenetics'. In: *Annual Review of Neuroscience* 34.1 (2011). _eprint: https://doi.org/10.1146/annurev-neuro-061010-113817, pp. 389–412. DOI: 10.1146/annurev-neuro-061010-113817 (cited on page 6).

[71] Karl Deisseroth. 'Optogenetics: 10 years of microbial opsins in neuroscience'. In: *Nature Neuroscience* 18.9 (Sept. 2015). Number: 9 Publisher: Nature Publishing Group, pp. 1213–1225. DOI: 10.1038/nn.4091 (cited on page 6).

[72] Valentina Emiliani et al. 'Optogenetics for light control of biological systems'. In: *Nature Reviews Methods Primers* 2.1 (July 21, 2022). Number: 1 Publisher: Nature Publishing Group, pp. 1–25. DOI: 10.1038/s43586-022-00136-4 (cited on page 6).

[73] Kay M. Tye and Karl Deisseroth. 'Optogenetic investigation of neural circuits underlying brain disease in animal models'. In: *Nature Reviews Neuroscience* 13.4 (Apr. 2012). Number: 4 Publisher: Nature Publishing Group, pp. 251–266. DOI: 10.1038/nrn3171 (cited on page 6).

[74] Talia N. Lerner, Li Ye, and Karl Deisseroth. 'Communication in Neural Circuits: Tools, Opportunities, and Challenges'. In: *Cell* 164.6 (Mar. 10, 2016), pp. 1136–1150. DOI: 10.1016/j.cell.2016.02.027 (cited on page 6).

[75] Carsten K. Pfeffer et al. 'Inhibition of inhibition in visual cortex: the logic of connections between molecularly distinct interneurons'. In: *Nature Neuroscience* 16.8 (Aug. 2013). Number: 8 Publisher: Nature Publishing Group, pp. 1068–1076. DOI: 10.1038/nn.3446 (cited on page 6).

[76] Stephanie C Seeman et al. 'Sparse recurrent excitatory connectivity in the microcircuit of the adult mouse and human cortex'. In: *eLife* 7 (Sept. 26, 2018). Ed. by Inna Slutsky, Eve Marder, and Per Jesper Sjöström. Publisher: eLife Sciences Publications, Ltd, e37349. DOI: 10.7554/eLife.37349 (cited on page 6).

[77] Verena Senn et al. 'Long-Range Connectivity Defines Behavioral Specificity of Amygdala Neurons'. In: *Neuron* 81.2 (Jan. 22, 2014), pp. 428–437. DOI: 10.1016/j.neuron.2013.11.006 (cited on page 6).

[78] Leopoldo Petreanu et al. 'The subcellular organization of neocortical excitatory connections'. In: *Nature* 457.7233 (Feb. 2009). Number: 7233 Publisher: Nature Publishing Group, pp. 1142–1145. DOI: 10.1038/nature07709 (cited on page 6).

[79] Benjamin R. Rost et al. 'Optogenetics at the presynapse'. In: *Nature Neuroscience* 25.8 (Aug. 2022). Number: 8 Publisher: Nature Publishing Group, pp. 984–998. DOI: 10.1038/s41593-022-01113-6 (cited on page 6).

[80] M. Desai et al. 'Mapping brain networks in awake mice using combined optical neural control and fMRI'. In: *Journal of Neurophysiology* 105.3 (Mar. 2011). Publisher: American Physiological Society, pp. 1393–1405. DOI: 10.1152/jn.00828.2010 (cited on page 6).

[81] Adam Q Bauer et al. 'Effective Connectivity Measured Using Optogenetically Evoked Hemodynamic Signals Exhibits Topography Distinct from Resting State Functional Connectivity in the Mouse'. In: *Cerebral Cortex* 28.1 (Jan. 1, 2018), pp. 370–386. DOI: 10.1093/cercor/bhx298 (cited on page 6).

[82] Ed Bullmore and Olaf Sporns. 'Complex brain networks: graph theoretical analysis of structural and functional systems'. In: *Nature Reviews Neuroscience* 10.3 (Mar. 2009). Number: 3 Publisher: Nature Publishing Group, pp. 186–198. DOI: 10.1038/nrn2575 (cited on pages 6, 12).

[83] C. J. Honey et al. 'Predicting human resting-state functional connectivity from structural connectivity'. In: *Proceedings of the National Academy of Sciences of the United States of America* 106.6 (Feb. 10, 2009), pp. 2035–2040. DOI: 10.1073/pnas.0811168106 (cited on page 6).

[84] Laura E. Suárez et al. 'Linking Structure and Function in Macroscale Brain Networks'. In: *Trends in Cognitive Sciences* 24.4 (Apr. 1, 2020). Publisher: Elsevier, pp. 302–315. DOI: 10.1016/j.tics.2020.01.008 (cited on page 6).

[85] Dominique Förster et al. 'An optogenetic toolbox for unbiased discovery of functionally connected cells in neural circuits'. In: *Nature Communications* 8.1 (July 24, 2017). Number: 1 Publisher: Nature Publishing Group, p. 116. DOI: 10.1038/s41467-017-00160-z (cited on pages 6, 78).

[86] Tina Schrödel et al. 'Brain-wide 3D imaging of neuronal activity in Caenorhabditis elegans with sculpted light'. In: *Nature Methods* 10.10 (Oct. 2013). Number: 10 Publisher: Nature Publishing Group, pp. 1013–1020. DOI: 10.1038/nmeth.2637 (cited on page 7).

[87] Ruben Portugues et al. 'Whole-Brain Activity Maps Reveal Stereotyped, Distributed Networks for Visuomotor Behavior'. In: *Neuron* 81.6 (Mar. 19, 2014), pp. 1328–1343. DOI: 10.1016/j.neuron.2014.01.019. (Visited on 12/27/2022) (cited on page 7).

[88] Misha B Ahrens and Florian Engert. 'Large-scale imaging in small brains'. In: *Current Opinion in Neurobiology*. Large-Scale Recording Technology (32) 32 (June 1, 2015), pp. 78–86. DOI: 10.1016/j.conb.2015.01.007. (Visited on 12/27/2022) (cited on page 7).

[89] W. Müller and J. A. Connor. 'Dendritic spines as individual neuronal compartments for synaptic Ca2+ responses'. In: *Nature* 354.6348 (Nov. 7, 1991), pp. 73–76. DOI: 10.1038/354073a0 (cited on page 7).

[90] David B. Jaffe et al. 'The spread of Na+ spikes determines the pattern of dendritic Ca2+ entry into hippocampal neurons'. In: *Nature* 357.6375 (May 1992). Number: 6375 Publisher: Nature Publishing Group, pp. 244–246. DOI: 10.1038/357244a0 (cited on page 7).

[91] Christine Grienberger and Arthur Konnerth. 'Imaging calcium in neurons'. In: *Neuron* 73.5 (Mar. 8, 2012), pp. 862–885. DOI: 10.1016/j.neuron.2012.02.011 (cited on page 7).

[92] Hailong Li et al. 'Imaging of mitochondrial Ca2+ dynamics in astrocytes using cell-specific mitochondria-targeted GCaMP5G/6s: mitochondrial Ca2+ uptake and cytosolic Ca2+ availability via the endoplasmic reticulum store'. In: *Cell Calcium* 56.6 (Dec. 2014), pp. 457–466. DOI: 10.1016/j.ceca.2014.09.008 (cited on page 8).

[93] Yiming Chen et al. 'Soma-Targeted Imaging of Neural Circuits by Ribosome Tethering'. In: *Neuron* 107.3 (Aug. 5, 2020), 454–469.e6. DOI: 10.1016/j.neuron.2020.05.005 (cited on page 8).

[94] Misha B. Ahrens et al. 'Whole-brain functional imaging at cellular resolution using light-sheet microscopy'. In: *Nature Methods* 10.5 (May 2013), pp. 413–420. DOI: 10.1038/nmeth.2434 (cited on page 8).

[95] Christina K. Kim et al. 'Prolonged, brain-wide expression of nuclear-localized GCaMP3 for functional circuit mapping'. In: *Frontiers in Neural Circuits* 8 (2014) (cited on page 8).

[96] Marco dal Maschio et al. 'Linking Neurons to Network Function and Behavior by Two-Photon Holographic Optogenetics and Volumetric Imaging'. In: *Neuron* 94.4 (May 17, 2017), 774–789.e5. DOI: 10.1016/j.neuron.2017.04.034 (cited on page 8).

[97] Marco Brondi et al. 'Optogenetic Methods to Investigate Brain Alterations in Preclinical Models'. In: *Cells* 11.11 (Jan. 2022). Number: 11 Publisher: Multidisciplinary Digital Publishing Institute, p. 1848. DOI: 10.3390/cells11111848 (cited on page 8).

[98] J. Nakai, M. Ohkura, and K. Imoto. 'A high signal-to-noise Ca(2+) probe composed of a single green fluorescent protein'. In: *Nature Biotechnology* 19.2 (Feb. 2001), pp. 137–141. DOI: 10.1038/84397 (cited on page 8).

[99] Tsai-Wen Chen et al. 'Ultrasensitive fluorescent proteins for imaging neuronal activity'. In: *Nature* 499.7458 (July 2013). Number: 7458 Publisher: Nature Publishing Group, pp. 295–300. DOI: 10.1038/nature12354 (cited on page 8).

[100] Hod Dana et al. 'High-performance calcium sensors for imaging activity in neuronal populations and microcompartments'. In: *Nature Methods* 16.7 (July 2019). Number: 7 Publisher: Nature Publishing Group, pp. 649–657. DOI: 10.1038/s41592-019-0435-6 (cited on page 8).

[101] Jasper Akerboom et al. 'Crystal Structures of the GCaMP Calcium Sensor Reveal the Mechanism of Fluorescence Signal Change and Aid Rational Design'. In: *The Journal of Biological Chemistry* 284.10 (Mar. 6, 2009), pp. 6455–6464. DOI: 10.1074/jbc.M807657200. (Visited on 12/27/2022) (cited on page 8).

[102] Siegfried Weisenburger and Alipasha Vaziri. 'A Guide to Emerging Technologies for Large-Scale and Whole-Brain Optical Imaging of Neuronal Activity'. In: *Annual Review of Neuroscience* 41 (July 8, 2018), pp. 431–452. DOI: 10.1146/annurev-neuro-072116-031458 (cited on page 9).

[103] Gaddum Duemani Reddy et al. 'Three-dimensional random access multiphoton microscopy for functional imaging of neuronal activity'. In: *Nature Neuroscience* 11.6 (June 2008), pp. 713–720. DOI: 10.1038/nn.2116 (cited on page 9).

[104] Na Ji, Jeremy Freeman, and Spencer L. Smith. 'Technologies for imaging neural activity in large volumes'. In: *Nature Neuroscience* 19.9 (Aug. 26, 2016), pp. 1154–1164. DOI: 10.1038/nn.4358 (cited on page 9).

[105] Marco Dal Maschio et al. 'Three-dimensional in vivo scanning microscopy with inertia-free focus control'. In: *Optics Letters* 36.17 (Sept. 1, 2011), pp. 3503–3505. DOI: 10.1364/OL.36.003503 (cited on page 11).

[106] Francesco Difato et al. 'Spatial Light Modulators for Complex Spatiotemporal Illumination of Neuronal Networks'. In: *Neuronal Network Analysis: Concepts and Experimental Approaches*. Ed. by Tommaso Fellin and Michael Halassa. Neuromethods. Totowa, NJ: Humana Press, 2012, pp. 61–81. DOI: 10.1007/7657_2011_3 (cited on page 11).

[107] Marco Dal Maschio. 'Computer-Generated Holographic Beams for the Investigation of the Molecular and Circuit Function'. In: June 26, 2014. DOI: 10.1007/978-3-662-43367-6 (cited on page 11).

[108] Weijian Yang et al. 'Simultaneous Multi-plane Imaging of Neural Circuits'. In: *Neuron* 89.2 (Jan. 20, 2016), pp. 269–284. DOI: 10.1016/j.neuron.2015.12.012 (cited on page 11).

[109] Rui Liu et al. 'Aberration-free multi-plane imaging of neural activity from the mammalian brain using a fast-switching liquid crystal spatial light modulator'. In: *Biomedical Optics Express* 10.10 (Oct. 1, 2019), pp. 5059–5080. DOI: 10.1364/BOE.10.005059 (cited on page 11).

[110] Katona G et al. 'Fast two-photon in vivo imaging with three-dimensional random-access scanning in large tissue volumes'. In: *Nature methods* 9.2 (Jan. 8, 2012). Publisher: Nat Methods. DOI: 10.1038/nmeth.1851 (cited on page 11).

[111] K. M. Naga Srinivas Nadella et al. 'Random-access scanning microscopy for 3D imaging in awake behaving animals'. In: *Nature Methods* 13.12 (Dec. 2016), pp. 1001–1004. DOI: 10.1038/nmeth.4033 (cited on page 11).

[112] Benjamin F. Grewe et al. 'Fast two-layer two-photon imaging of neuronal cell populations using an electrically tunable lens'. In: *Biomedical Optics Express* 2.7 (July 1, 2011). Publisher: Optica Publishing Group, pp. 2035–2046. DOI: 10.1364/BOE.2.002035 (cited on page 11).

[113] Wulfram Gerstner, Henning Sprekeler, and Gustavo Deco. 'Theory and Simulation in Neuroscience'. In: *Science* 338.6103 (Oct. 5, 2012). Publisher: American Association for the Advancement of Science, pp. 60–65. DOI: 10.1126/science.1227356 (cited on page 11).

[114] Kerstin Lenk et al. 'A Computational Model of Interactions Between Neuronal and Astrocytic Networks: The Role of Astrocytes in the Stability of the Neuronal Firing Rate'. In: *Frontiers in Computational Neuroscience* 13 (2020) (cited on page 11).

[115] Amit Naskar et al. 'Multiscale dynamic mean field (MDMF) model relates resting-state brain dynamics with local cortical excitatory–inhibitory neurotransmitter homeostasis'. In: *Network Neuroscience* 5.3 (Sept. 2, 2021), pp. 757–782. DOI: 10.1162/netn_a_00197 (cited on page 11).

[116] Olaf Sporns. 'Graph theory methods: applications in brain networks'. In: *Dialogues in Clinical Neuroscience* 20.2 (June 30, 2018), pp. 111–121. DOI: 10.31887/DCNS.2018.20.2/osporns (cited on page 12).

[117] Jaap C. Reijneveld et al. 'The application of graph theoretical analysis to complex networks in the brain'. In: *Clinical Neurophysiology* 118.11 (Nov. 1, 2007), pp. 2317–2331. DOI: 10.1016/j.clinph.2007.08.010 (cited on page 12).

[118] Stanley Milgram. 'The Small World Problem'. In: Psychology Today.2 (1967), pp. 60–67 (cited on page 12).

[119] Duncan J. Watts and Steven H. Strogatz. 'Collective dynamics of 'small-world' networks'. In: *Nature* 393.6684 (June 1998). Number: 6684 Publisher: Nature Publishing Group, pp. 440–442. DOI: 10.1038/30918 (cited on page 12).

[120] Lav R. Varshney et al. 'Structural Properties of the Caenorhabditis elegans Neuronal Network'. In: *PLOS Computational Biology* 7.2 (Feb. 3, 2011). Publisher: Public Library of Science, e1001066. DOI: 10.1371/journal.pcbi.1001066 (cited on page 12).

[121] Maxwell H. Turner, Kevin Mann, and Thomas R. Clandinin. 'The connectome predicts resting state functional connectivity across the Drosophila brain'. In: *Current biology : CB* 31.11 (June 7, 2021), 2386–2394.e3. DOI: 10.1016/j.cub.2021.03.004 (cited on pages 12, 13, 24).

[122] Michael Stobb et al. 'Graph theoretical model of a sensorimotor connectome in zebrafish'. In: *PloS One* 7.5 (2012), e37292. DOI: 10.1371/journal.pone.0037292 (cited on page 12).

[123] Richard F. Betzel. 'Organizing principles of whole-brain functional connectivity in zebrafish larvae'. In: *Network Neuroscience* 4.1 (Mar. 1, 2020), pp. 234–256. DOI: 10.1162/netn_a_00121 (cited on pages 12, 13, 76).

[124] Murray Shanahan et al. 'Large-scale network organization in the avian forebrain: a connectivity matrix and theoretical analysis'. In: *Frontiers in Computational Neuroscience* 7 (2013) (cited on page 12).

[125] Yong He, Zhang J. Chen, and Alan C. Evans. 'Small-World Anatomical Networks in the Human Brain Revealed by Cortical Thickness from MRI'. In: *Cerebral Cortex* 17.10 (Oct. 1, 2007), pp. 2407–2419. DOI: 10.1093/cercor/bhl149 (cited on page 12).

[126] Jinhui Wang et al. 'Parcellation-dependent small-world brain functional networks: A resting-state fMRI study'. In: *Human Brain Mapping* 30.5 (2009), pp. 1511–1523. DOI: 10.1002/hbm.20623 (cited on page 12).

[127] Ann S. Blevins et al. 'From calcium imaging to graph topology'. In: *Network Neuroscience* 6.4 (Oct. 1, 2022), pp. 1125–1147. DOI: 10.1162/netn_a_00262 (cited on page 13).

[128] Yoshinori Aso et al. 'The neuronal architecture of the mushroom body provides a logic for associative learning'. In: *eLife* 3 (Dec. 23, 2014). Ed. by Leslie C Griffith. Publisher: eLife Sciences Publications, Ltd, e04577. DOI: 10.7554/eLife.04577 (cited on pages 13, 14).

[129] Feng Li et al. 'The connectome of the adult Drosophila mushroom body provides insights into function'. In: *eLife* 9 (Dec. 14, 2020). Ed. by Leslie C Griffith et al. Publisher: eLife Sciences Publications, Ltd, e62576. DOI: 10.7554/eLife.62576 (cited on page 13).

[130] Claire Eschbach et al. *Multilevel feedback architecture for adaptive regulation of learning in the insect brain*. Pages: 649731 Section: New Results. May 27, 2019. DOI: 10.1101/649731. URL: https://www.biorxiv.org/content/10.1101/649731v1 (cited on pages 13, 14).

[131] Raya Khanin and Ernst Wit. *How Scale-Free Are Biological Networks*. https://home.liebertpub.com/cmb. Archive Location: 2 Madison Avenue Larchmont, NY 10538 USA Publisher: Mary Ann Liebert, Inc. 2 Madison Avenue Larchmont, NY 10538 USA. May 17, 2006. DOI: 10.1089/cmb.2006.13.810. URL: https://www.liebertpub.com/doi/10.1089/cmb.2006.13.810 (cited on page 13).

[132] Ad Broido and A Clauset. 'Scale-free networks are rare'. In: *Nature communications* 10.1 (Mar. 4, 2019). Publisher: Nat Commun. DOI: 10.1038/s41467-019-08746-5 (cited on page 13).

[133] Thijs L. van der Plas et al. *Neural assemblies uncovered by generative modeling explain whole-brain activity statistics and reflect structural connectivity*. Pages: 2021.11.09.467900 Section: New Results. June 10, 2022. DOI: 10.1101/2021.11.09.467900. URL: https://www.biorxiv.org/content/10.1101/2021.11.09.467900v2 (cited on pages 13, 15).

[134] Ashwin Vishwanathan et al. *Predicting modular functions and neural coding of behavior from a synaptic wiring diagram*. Apr. 17, 2022. DOI: 10.1101/2020.10.28.359620. URL: https://www.biorxiv.org/content/10.1101/2020.10.28.359620v3 (cited on pages 13, 26, 39, 75, 77).

[135] Matteo Bruzzone et al. 'Whole brain functional recordings at cellular resolution in zebrafish larvae with 3D scanning multiphoton microscopy'. In: *Scientific Reports* 11.1 (May 26, 2021). Number: 1 Publisher: Nature Publishing Group, p. 11048. DOI: 10.1038/s41598-021-90335-y (cited on pages 17, 29, 55, 56, 58, 61–64).

[136] J.-P. Onnela et al. 'Intensity and coherence of motifs in weighted complex networks'. In: *Physical Review E* 71.6 (June 13, 2005), p. 065103. DOI: 10.1103/PhysRevE.71.065103 (cited on page 19).

[137] M. E. J. Newman. 'Mixing patterns in networks'. In: *Physical Review E* 67.2 (Feb. 27, 2003), p. 026126. DOI: 10.1103/PhysRevE.67.026126 (cited on page 19).

[138] Mark Newman. 'The configuration model'. In: *Networks*. Ed. by Mark Newman. Oxford University Press, July 26, 2018, p. 0. DOI: 10.1093/oso/9780198805090.003.0012 (cited on page 20).

[139] V. A. Traag, L. Waltman, and N. J. van Eck. 'From Louvain to Leiden: guaranteeing well-connected communities'. In: *Scientific Reports* 9.1 (Mar. 26, 2019). Number: 1 Publisher: Nature Publishing Group, p. 5233. DOI: 10.1038/s41598-019-41695-z (cited on pages 20, 21, 39).

[140] Brian B. Avants et al. 'A reproducible evaluation of ANTs similarity metric performance in brain image registration'. In: *NeuroImage* 54.3 (Feb. 1, 2011), pp. 2033–2044. DOI: 10.1016/j.neuroimage.2010.09.025 (cited on page 24).

[141] Yunmin Wu et al. 'An Optical Illusion Pinpoints an Essential Circuit Node for Global Motion Processing'. In: *Neuron* 108.4 (Nov. 25, 2020), 722–734.e5. DOI: 10.1016/j.neuron.2020.08.027 (cited on pages 24, 44, 49).

[142] Armen Stepanyants, Patrick R. Hof, and Dmitri B. Chklovskii. 'Geometry and Structural Plasticity of Synaptic Connectivity'. In: *Neuron* 34.2 (Apr. 11, 2002), pp. 275–288. DOI: 10.1016/S0896-6273(02)00652-9 (cited on page 25).

[143] Armen Stepanyants and Dmitri B. Chklovskii. 'Neurogeometry and potential synaptic connectivity'. In: *Trends in Neurosciences* 28.7 (July 1, 2005), pp. 387–394. DOI: 10.1016/j.tins.2005.05.006 (cited on page 25).

[144] Christopher L. Rees, Keivan Moradi, and Giorgio A. Ascoli. 'Weighing the Evidence in Peters' Rule: Does Neuronal Morphology Predict Connectivity?' In: *Trends in neurosciences* 40.2 (Feb. 2017), pp. 63–71. DOI: 10.1016/j.tins.2016.11.007 (cited on page 25).

[145] Johan Galtung. *Theory and methods of social research*. In collab. with Internet Archive. Oslo, Universitetsforlaget; New York, Columbia University Press [etc.], 1967. 550 pp. (cited on page 26).

[146] Aric A Hagberg, Daniel A Schult, and Pieter J Swart. 'Exploring Network Structure, Dynamics, and Function using NetworkX'. In: (2008) (cited on page 26).

[147] Charles R. Harris et al. 'Array programming with NumPy'. In: *Nature* 585.7825 (Sept. 2020). Number: 7825 Publisher: Nature Publishing Group, pp. 357–362. DOI: 10.1038/s41586-020-2649-2 (cited on page 26).

[148] Pauli Virtanen et al. 'SciPy 1.0: fundamental algorithms for scientific computing in Python'. In: *Nature Methods* 17.3 (Mar. 2020). Number: 3 Publisher: Nature Publishing Group, pp. 261–272. DOI: 10.1038/s41592-019-0686-2 (cited on page 26).

[149] Didier Ruedin. 'An Introduction to the R Package Agrmt'. In: (Nov. 12, 2021) (cited on page 26).

[150] Marco Morsch et al. 'Triggering Cell Stress and Death Using Conventional UV Laser Confocal Microscopy'. In: *Journal of Visualized Experiments: JoVE* 120 (Feb. 3, 2017), p. 54983. DOI: 10.3791/54983 (cited on page 27).

[151] Vilim Štih et al. 'Stytra: An open-source, integrated system for stimulation, tracking and closed-loop behavioral experiments'. In: *PLOS Computational Biology* 15.4 (Apr. 8, 2019). Publisher: Public Library of Science, e1006699. DOI: 10.1371/journal.pcbi.1006699 (cited on page 31).

[152] Marius Pachitariu et al. *Suite2p: beyond 10,000 neurons with standard two-photon microscopy*. June 30, 2016. DOI: 10.1101/061507 (cited on page 31).

[153] Andrew Miri et al. 'Regression-Based Identification of Behavior-Encoding Neurons During Large-Scale Optical Imaging of Neural Activity at Cellular Resolution'. In: *Journal of Neurophysiology* 105.2 (Feb. 2011), pp. 964–980. DOI: 10.1152/jn.00702.2010 (cited on page 32).

[154] Fabian Pedregosa et al. 'Scikit-learn: Machine Learning in Python'. In: *Journal of Machine Learning Research* 12.85 (2011), pp. 2825–2830 (cited on page 34).

[155] Laura Corradi et al. 'Hypothalamic Galanin-producing neurons regulate stress in zebrafish through a peptidergic, self-inhibitory loop'. In: *Current Biology* 32.7 (Apr. 11, 2022), 1497–1510.e5. DOI: 10.1016/j.cub.2022.02.011. (Visited on 12/14/2022) (cited on pages 36, 67, 73).

[156] Olaf Sporns and Richard F. Betzel. 'Modular Brain Networks'. In: *Annual review of psychology* 67 (Jan. 4, 2016), pp. 613–640. DOI: 10.1146/annurev-psych-122414-033634 (cited on page 41).

[157] Jeroen Crucke, Annelore Van de Kelft, and Ann Huysseune. 'The innervation of the zebrafish pharyngeal jaws and teeth'. In: *Journal of Anatomy* 227.1 (July 2015), pp. 62–71. DOI: 10.1111/joa.12321 (cited on page 44).

[158] Pedro M. Henriques et al. 'Nucleus Isthmi Is Required to Sustain Target Pursuit during Visually Guided Prey-Catching'. In: *Current biology: CB* 29.11 (June 3, 2019), 1771–1786.e5. DOI: 10.1016/j.cub.2019.04.064 (cited on page 44).

[159] Catherine A. McCormick. 'Central Lateral Line Mechanosensory Pathways in Bony Fish'. In: *The Mechanosensory Lateral Line*. Ed. by Sheryl Coombs, Peter Görner, and Heinrich Münz. New York, NY: Springer, 1989, pp. 341–364. DOI: 10.1007/978-1-4612-3560-6_17 (cited on page 45).

[160] David W. Raible and Gregory J. Kruse. 'Organization of the lateral line system in embryonic zebrafish'. In: *Journal of Comparative Neurology* 421.2 (2000), pp. 189–198. DOI: 10.1002/(SICI)1096-9861(20000529)421:2<189::AID-CNE5>3.0.CO;2-K (cited on page 45).

[161] James C. Liao and Melanie Haehnel. 'Physiology of afferent neurons in larval zebrafish provides a functional framework for lateral line somatotopy'. In: *Journal of Neurophysiology* 107.10 (May 15, 2012). Publisher: American Physiological Society, pp. 2615–2623. DOI: 10.1152/jn.01108.2011 (cited on pages 45, 46).

[162] Ryann M. Fame, Carole Brajon, and Alain Ghysen. 'Second-order projection from the posterior lateral line in the early zebrafish brain'. In: *Neural Development* 1.1 (Nov. 29, 2006), p. 4. DOI: 10.1186/1749-8104-1-4 (cited on page 46).

[163] Andrew W. Thompson et al. 'Functional Profiles of Visual-, Auditory-, and Water Flow-Responsive Neurons in the Zebrafish Tectum'. In: *Current Biology* 26.6 (Mar. 21, 2016), pp. 743–754. DOI: 10.1016/j.cub.2016.01.041 (cited on page 46).

[164] Isaac H. Bianco et al. 'The Tangential Nucleus Controls a Gravito-inertial Vestibulo-ocular Reflex'. In: *Current Biology* 22.14 (July 24, 2012), pp. 1285–1295. DOI: 10.1016/j.cub.2012.05.026 (cited on page 47).

[165] Itia A. Favre-Bulle et al. 'Cellular-Resolution Imaging of Vestibular Processing across the Larval Zebrafish Brain'. In: *Current Biology* 28.23 (Dec. 3, 2018), 3711–3722.e3. DOI: 10.1016/j.cub.2018.09.060 (cited on page 47).

[166] Hideaki Matsui et al. 'Functional regionalization of the teleost cerebellum analyzed in vivo'. In: *Proceedings of the National Academy of Sciences* 111.32 (Aug. 12, 2014). Publisher: Proceedings of the National Academy of Sciences, pp. 11846–11851. DOI: 10.1073/pnas.1403105111 (cited on page 47).

[167] Young-Ki Bae et al. 'Anatomy of zebrafish cerebellum and screen for mutations affecting its development'. In: *Developmental Biology* 330.2 (June 15, 2009), pp. 406–426. DOI: 10.1016/j.ydbio.2009.04.013 (cited on page 47).

[168] Herwig Baier and Mario F. Wullimann. 'Anatomy and function of retinorecipient arborization fields in zebrafish'. In: *Journal of Comparative Neurology* 529.15 (2021), pp. 3454–3476. DOI: 10.1002/cne.25204 (cited on page 48).

[169] Estuardo Robles, Eva Laurell, and Herwig Baier. 'The Retinal Projectome Reveals Brain-Area-Specific Visual Representations Generated by Ganglion Cell Diversity'. In: *Current Biology* 24.18 (Sept. 22, 2014), pp. 2085–2096. DOI: 10.1016/j.cub.2014.07.080 (cited on page 48).

[170] Lucy A. L. Heap et al. 'Luminance Changes Drive Directional Startle through a Thalamic Pathway'. In: *Neuron* 99.2 (July 25, 2018), 293–301.e4. DOI: 10.1016/j.neuron.2018.06.013 (cited on page 49).

[171] Kun Wang et al. 'Selective processing of all rotational and translational optic flow directions in the zebrafish pretectum and tectum'. In: *BMC Biology* 17.1 (Mar. 29, 2019), p. 29. DOI: 10.1186/s12915-019-0648-2 (cited on page 49).

[172] Anna Kramer et al. 'Neuronal Architecture of a Visual Center that Processes Optic Flow'. In: *Neuron* 103.1 (July 3, 2019), 118–132.e7. DOI: 10.1016/j.neuron.2019.04.018 (cited on page 49).

[173] Incinur Temizer et al. 'A Visual Pathway for Looming-Evoked Escape in Larval Zebrafish'. In: *Current biology: CB* 25.14 (July 20, 2015), pp. 1823–1834. DOI: 10.1016/j.cub.2015.06.002 (cited on page 49).

[174] Thomas O. Helmbrecht et al. 'Topography of a Visuomotor Transformation'. In: *Neuron* 100.6 (2018), 1429–1445.e4. DOI: 10.1016/j.neuron.2018.10.021 (cited on pages 49, 76, 78).

[175] Robert J. Sutherland. 'The dorsal diencephalic conduction system: A review of the anatomy and functions of the habenular complex'. In: *Neuroscience & Biobehavioral Reviews* 6.1 (Mar. 1982), pp. 1–13. DOI: 10.1016/0149-7634(82)90003-3 (cited on page 50).

[176] Hidenori Aizawa et al. 'Laterotopic Representation of Left-Right Information onto the Dorso-Ventral Axis of a Zebrafish Midbrain Target Nucleus'. In: *Current Biology* 15.3 (Feb. 8, 2005), pp. 238–243. DOI: 10.1016/j.cub.2005.01.014 (cited on page 50).

[177] Ryunosuke Amo et al. 'Identification of the Zebrafish Ventral Habenula As a Homolog of the Mammalian Lateral Habenula'. In: *The Journal of Neuroscience* 30.4 (Jan. 27, 2010), pp. 1566–1574. DOI: 10.1523/JNEUROSCI.3690-09.2010 (cited on page 50).

[178] Bor-Wei Cherng et al. 'The Dorsal Lateral Habenula-Interpeduncular Nucleus Pathway Is Essential for Left-Right-Dependent Decision Making in Zebrafish'. In: *Cell Reports* 32.11 (Sept. 15, 2020), p. 108143. DOI: 10.1016/j.celrep.2020.108143 (cited on page 50).

[179] Shannon L. Wolfman et al. 'Nicotine aversion is mediated by GABAergic interpeduncular nucleus inputs to laterodorsal tegmentum'. In: *Nature Communications* 9.1 (July 13, 2018). Number: 1 Publisher: Nature Publishing Group, p. 2710. DOI: 10.1038/s41467-018-04654-2 (cited on page 50).

[180] Ian McLaughlin, John A. Dani, and Mariella De Biasi. 'The medial habenula and interpeduncular nucleus circuitry is critical in addiction, anxiety, and mood regulation'. In: *Journal of Neurochemistry* 142 (S2 2017). _eprint: https://onlinelibrary.wiley.com/doi/pdf/10.1111/jnc.14008, pp. 130–143. DOI: 10.1111/jnc.14008 (cited on page 50).

[181] Nobuhiko Miyasaka et al. 'Olfactory projectome in the zebrafish forebrain revealed by genetic single-neuron labelling'. In: *Nature Communications* 5.1 (Apr. 9, 2014). Number: 1 Publisher: Nature Publishing Group, p. 3639. DOI: 10.1038/ncomms4639 (cited on pages 52, 76).

[182] Matthew Lovett-Barron et al. 'Ancestral Circuits for the Coordinated Modulation of Brain State'. In: *Cell* 171.6 (Nov. 30, 2017), 1411–1423.e17. DOI: 10.1016/j.cell.2017.10.021 (cited on page 68).

[183] Colette M. vom Berg-Maurer et al. 'The Severity of Acute Stress Is Represented by Increased Synchronous Activity and Recruitment of Hypothalamic CRH Neurons'. In: *Journal of Neuroscience* 36.11 (Mar. 16, 2016). Publisher: Society for Neuroscience Section: Articles, pp. 3350–3362. DOI: 10.1523/JNEUROSCI.3390-15.2016 (cited on page 72).

[184] Mario F. Wullimann and Thomas Mueller. 'Teleostean and mammalian forebrains contrasted: Evidence from genes to behavior'. In: *Journal of Comparative Neurology* 475.2 (2004), pp. 143–162. DOI: 10.1002/cne.20183 (cited on page 76).

[185] Rainer W. Friedrich, Christopher J. Habermann, and Gilles Laurent. 'Multiplexing using synchrony in the zebrafish olfactory bulb'. In: *Nature Neuroscience* 7.8 (Aug. 2004). Number: 8 Publisher: Nature Publishing Group, pp. 862–871. DOI: 10.1038/nn1292 (cited on page 76).

[186] Emre Yaksi et al. 'Transformation of odor representations in target areas of the olfactory bulb'. In: *Nature Neuroscience* 12.4 (Apr. 2009). Number: 4 Publisher: Nature Publishing Group, pp. 474–482. DOI: 10.1038/nn.2288 (cited on page 76).

[187] Xiuye Chen et al. 'Brain-wide Organization of Neuronal Activity and Convergent Sensorimotor Transformations in Larval Zebrafish'. In: *Neuron* 100.4 (Nov. 21, 2018), 876–890.e5. DOI: 10.1016/j.neuron.2018.09.042 (cited on pages 76, 78).

[188] Daniella Dumitriu et al. 'Correlation Between Axonal Morphologies and Synaptic Input Kinetics of Interneurons from Mouse Visual Cortex'. In: *Cerebral Cortex* 17.1 (Jan. 1, 2007), pp. 81–91. DOI: 10.1093/cercor/bhj126 (cited on page 78).